PhD Dissertation

On Proteins and Phantasms in Photoactivated Localization Microscopy

Point Process Methods for Correction of Imaging Artifacts

Louis Gammelgaard Jensen

Department of Mathematics
Aarhus University
2021

On Proteins and Phantasms in Photoactivated Localization Microscopy
Point Process Methods for Correction of Imaging Artifacts

PhD dissertation by
Louis Gammelgaard Jensen

Department of Mathematics, Aarhus University
Ny Munkegade 118, 8000 Aarhus C, Denmark

Supervised by
Associate Professor Ute Hahn, Aarhus University

Submitted to Graduate School of Natural Sciences, Aarhus, July 30, 2021

Dissertation was typesat in kpfonts with
pdfLaTeX and the memoir class

AARHUS
UNIVERSITY
DEPARTMENT OF MATHEMATICS

Contents

Preface

This dissertation concludes my PhD studies at the Department of Mathematics, Aarhus University, which began in February of 2018. It consists of three self-contained papers, an introductory chapter which cover background material and new results in papers A and B, and a chapter providing mathematical details for paper C. The papers were made possible with the help of several coauthors both from abroad and Aarhus University, and my supervisor Ute Hahn, also of the Department of Mathematics.

The papers are:

Paper A Semiparametric point process modeling of blinking artifacts in PALM. Revised manuscript submitted to *The Annals of Applied Statistics*.

Paper B Correction of multiple-blinking artefacts in photoactivated localisation microscopy. Under revision for *Nature Methods*.

Paper C Regulated exocytosis: renal aquaporin-2 3D vesicular network organization and association with F-actin. Under revision for *American Journal of Physiology: Cell Physiology*.

My contributions to papers B and C are clearly stated in the manuscripts, and they will not be repeated here. For paper A, I have been extensively involved in the methodological development, and have written the paper. In addition, I wrote the code underlying newly developed methods, and performed the analyses on real and simulated data.

Acknowledgments

My PhD studies were funded in large part by the now closed Centre for Stochastic Geometry and Bioimaging (CSGB), which was funded by the Villum Foundation. My work was greatly enhanced through the many social gatherings offered by CSGB, and I was able to meet people I would since collaborate with.

I would also like to thank the many coauthors on all three papers for being exceedingly pleasant partners in crime. Your passionate involvement throughout has been inspirational.

Last but certainly not least, I would like to thank my supervisor, Ute Hahn, for the many discussions on everything from microscopy and point processes to plants and music, for offering cake and coffee at every hour of the day, and for believing in the path I walked. Thank you, Ute, for helping me in my pursuit of a PhD, and for introducing me to a very exciting area of research!

Louis Gammelgaard Jensen
Aarhus, July 2021

Summary

In this dissertation, we deal with modeling of data from Photoactivated Localization Microscopy (PALM), and in particular the various imaging artifacts that affect it. Of these, the multiple blinking problem is of principal interest, and is the focal point of papers A and B. Paper C is an applied study of protein clustering and interactions, and modeling of imaging artifacts here takes a back seat to more biologically motivated analyses.

More specifically, Paper A is concerned with modeling and estimation of image artifacts in PALM, taking an approach based on point process theory. The methodological development here has been guided by a strong desire to obtain methods that can be used without a need for calibration data, which is typically required by competing methods. As a way to realize this, we develop the Independent Blinking Cluster point process (IBCpp) family of models intended for Single-Molecule Localization Microscopy (SMLM) modalities, and importantly the PALM-IBCpp for PALM data. We present a useful result on the mark correlation function for IBCpp models, and use it as a basis for an estimation scheme that can be used without assumptions on the distribution of proteins. We validate our methods on nuclear pore complex reference data, and we can show a close correspondence between expectations and model predictions. We also develop a test for complete spatial randomness (CSR) that is corrected for blinking biases, and illustrate its use on a real PALM recording of the protein Linker for Activation of T cells (LAT).

As a natural extension of this work, Paper B goes a step further, and attempts to clean PALM images of the artifacts. We achieve this by combining the estimated artifact parameters, obtained via Paper A, with a Bayesian model for the full spatio temporal data. On the basis of this model and the parameters, we generate various proposals for cleaned images, and pick the proposal with the largest posterior probability. We demonstrate this method on simulated data, and compare it with a state of the art, threshold-based method, where we show superior results, as measured on counting error, Wasserstein distance, and Ripley's L-function. We show that PALM images can be sufficiently cleaned up to allow for CSR testing at the correct level.

Finally, in Paper C, we imaged renal epithelial cells expressing the water channel protein Aquaporin-2 (AQP2), and the cytoskeletal protein F-Actin (ACT). Using 3D PALM, we could uncovered the organization of AQP2 into vesicular structures, and ACT into a fibrous layer. We extracted and modeled the vesicles, and tested for significant interactions with ACT for wildtype AQP2. Similar analyzes were carried out for cells expressing phosphorylation mutants of AQP2, and we could demonstrate differences in vesicle sizes and strength of ACT association.

Resumé

Denne afhandling omhandler modellering af data fra *Photoactivated Localization Microscopy* (PALM), og nærmere bestemt de billedartefakter, som påvirker denne form for mikroskopi. Af disse har *multiple blinking* problemet den største interesse, og er i fokus i artiklerne A og B. Artikel C er et anvendt studie af sammenklumpning af, og interaktioner mellem, proteiner. Modellering af billedartefakter spiller således en birolle her ift. mere biologisk motiverede analyser.

Mere specifikt undersøges der i artikel A, hvordan billedartefakter kan modelleres og estimeres, med teoretisk udgangspunkt i punktprocesser. Den metodologiske udvikling er her påvirket af et ønske om metoder, som kan benyttes uden kalibreringsdata, som typisk forlanges af konkurrerende metoder. For at opnå dette udvikler vi en familie af punktprocesser, *Independent Blinking Cluster point processes* (IBCpp), tiltænkt modellering af data fra *Single-Molecule Localization Microscopy* (SMLM), og særligt udvikles PALM-IBCpp modellen til PALM data. Vi præsenterer et nyttigt resultat om den markerede korrelationsfunktion, som danner baggrund for en estimationsmetode, hvor igen antagelser om den rumlige fordeling af proteiner er nødvendig. Vi validerer vores metoder på referencedata af nukleare porekomplekser, og vi kan herigennem demonstrere en tæt samhørighed mellem forventninger og modellens forskrivelser. Vi udvikler et test for *complete spatial randomness* (CSR), der er korrigeret for bias fra artefakter, og illustrerer brugen på en PALM optagelse af proteinet *Linker for Activation of T cells* (LAT).

Som en naturlig videreførelse af dette projekt går vi i artikel B skridtet videre, og forsøger helt at fjerne billedartefakterne. Vi kombinerer estimerede artefaktparametre, opnået gennem artikel A, med en Bayesiansk model for det observerede rumtidsdata. Med det udgangspunkt betragter vi adskillelige forslag til rengjorte billeder, og vi vælger imellem dem på baggrund af deres *posterior* sandsynlighed. Vi demonstrerer denne fremgangsmåde på simulerede data, hvor vi også sammenligner resultater med en etableret, tærskelbaseret metode. Vi kan derved vise, at vores metode har bedre ydeevne målt på tællefejl, Wasserstein-afstand og Ripleys L-funktion. Vi viser også, at PALM-billeder kan rengøres i en sådan grad, at et test for CSR kan foretages på det korrekte niveau.

Afslutningsvist tager vi i artikel C udgangspunkt i epithelceller i nyrevæv. Disse celler udtrykker proteinet *Aquaporin-2*(AQP2), der fungerer som vandkanal i cellemembranen, og proteinet *F-Actin* (ACT), som giver struktur til cytoskelettet. Ved brug af 3D PALM kan vi afdække, at AQP2 og ACT organiserer sig i hhv. vesikulære strukture og et lag bestående af fibre. Vi segmenterer og modellerer vesiklerne, og tester for signifikante interaktioner med ACT-laget. Analyserne gentages for muterede celler med forandret fosforyleringstilstand, og vi kunne herved demonstrere, at der er forskelle i vesikelstørrelse og interaktionsgraden med ACT.

Introduction to papers A and B

This chapter serves as an introduction to the background and main results of papers A and B, which are closely related. In particular, we go over conventional fluorescence microscopy and PALM, the imaging artifacts inherent to PALM, and commonly employed correction methodologies. In this light, the main results and new correction ideas of papers A and B are then presented.

We assume the reader is familiar with point process theory, including moment measures and the mark- and pair correlation functions. A quick rundown of these concepts can be found in Section A.2.1 of paper A, which also provides references to a more formal treatment.

1 Fluorescence microscopy

As a starting point towards an understanding of imaging artifacts in Photoactivated Localization Microscopy (PALM) [5], it is necessary to first understand the basics of fluorescence microscopy (FM), a generic term that covers a large number of techniques. What all FM modalities have in common is the use of fluorescent emissions from target structures, which can then be captured and observed by a camera. These fluorescent targets are referred to as fluorophores, and FM methods differ primarily in their choice of fluorophore, and the implementation modifications necessary to accommodate this choice. For this work we are interested in FM for its ability to image proteins, and in this context we can separate FM modalities into two broad categories. Single-Molecule Localization Microscopy (SMLM) [17] methods are capable of uncovering the positions of individual proteins, whereas Conventional Fluorescence Microscopy (CFM) methods can at best hope to recover a density map of protein positions [32].

Although PALM, which is an SMLM modality, is the main interest of our work, it is instructive to first consider CFM, which has all the same building blocks as SMLM. Fundamentally, CFM is a selectively magnifying device that zooms in on fluorescent emissions of a desired wavelength. In particular, for the imaging of proteins, it is necessary that the target protein is able to fluoresce, which can be accomplished in several ways. Notably, the protein can be genetically engineered into a fluorescent protein (FP), a mutant of the original protein carrying a fluorescent label [6]. Alternatively, antigen proteins can be tagged with fluorophore-carrying antibodies, a technique referred to as immunofluorescence [38]. Whichever method is used, the sample of proteins is made fluorescent, and imaging can proceed. Very briefly, the fluorophores are illuminated with an excitation laser, and begin to fluoresce. Owing to the Stokes shift, the emitted light will differ in wavelength from that of the excitation light, and the excitation light can thus be filtered out using a spectral filter, leaving only the signal of interest, which is ultimately digitized by a camera.

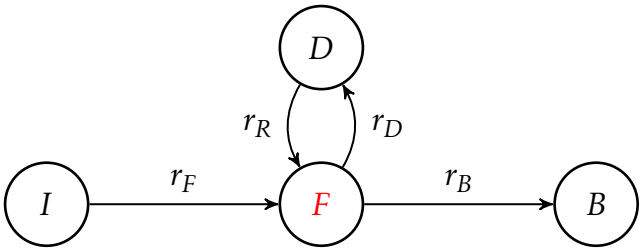

Figure 1: PA-FP switch states according to a Markov process. The inactivated I state corresponds to a PA-FP that has not yet switched to its activated form. After this initial switch, the PA-FP will emit fluorescence while in the F state. The D state is a temporary nonfluorescent state, and B is the absorbing, permanently nonfluorescent state, corresponding to a photobleaching event.

As mentioned, the shortcoming of CFM is its inability to uncover individual proteins. Owing to the diffraction of light, photons emitted from an FP will appear as a blurry spot on the camera, with a shape described by the point spread function (PSF). Mathematically, the observed signal can then be thought of as the convolution

$$I = P * \mathrm{PSF}, \tag{1.1}$$

where I is the observed image, and P is the sample of proteins. Because of this, fluorophores become increasingly difficult to tell apart as their spatial separation is decreased. In fact, for distances smaller than the full width at half maximum (FWHM) of the PSF, the fluorophores become entirely indistinguishable [31, p. 1090]. The FWHM is given as approximately

$$d \approx \frac{\lambda}{2\mathrm{NA}}, \tag{1.2}$$

where λ is the wavelength, and NA is the numerical aperture of the microscope lens. This smallest resolvable distance is sometimes called the Abbe diffraction limit, in honor of German physicist Ernst Abbe who discovered it in 1873. Achievable values of d are bounded in practice by microscope construction limits and the cytotoxicity associated with low wavelengths - a realistic best case value is around $d \approx 180$nm [21]. Unfortunately, in the study of protein interactions, relevant distances may be measured in just a few nanometers, and the resolution of CFM is then clearly insufficient.

1.1 Photoactivated Localization Microscopy

The principal observation allowing PALM to circumvent the diffraction limit, is that isolated fluorescent proteins can be localized with high precision. Problems only occur when several fluorophores are observed simultaneously in close proximity; in fact, the uncertainty (standard deviation) about the location of a single FP can be approximated by the expression

$$\sigma \approx \frac{\sigma_{PSF}}{\sqrt{N}} \tag{1.3}$$

where σ_{PSF} is the ”size” of the PSF, and N is the number of photons emitted during the experiment [14]. For instance, in a standard case where the PSF is modeled with an isotropic Gaussian function, σ_{PSF} is the standard deviation of this Gaussian [9]. In

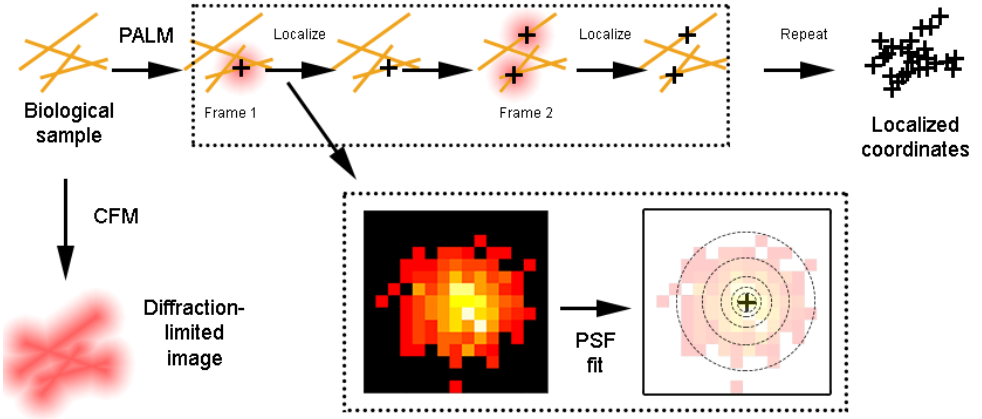

Figure 2: Imaging a biological sample with conventional fluorescence microscopy produces a diffraction-limited image, whereas PALM results in a list of coordinates by a series of localization steps. This is made possible by the sequential activation and bleaching of PA-FPs, the fluorophore type used in PALM.

principle there is therefore nothing stopping us from obtaining arbitrarily accurate measurements of isolated FPs, assuming they are sufficiently bright.

To exploit this fact, PALM uses a particular class of FPs, namely the photoactivateable fluorescent proteins (PA-FP) [6]. These fluorophores operate slightly differently from regular FPs, in that they can exist in an activated and an inactivated form. When illuminated with a light of the correct wavelength (the *activation laser*) they will enter the activated form after a stochastic waiting time, and only from the activated form can they then fluoresce upon illumination with an excitation laser. The important part is that the excitation and activation lasers use different frequencies, and can consequently be operated at different intensities. To understand why this is useful, we need a slightly more detailed understanding of the PA-FPs used in PALM. Each PA-FP in a given sample is believed to operate independently and identically according to a Markov process [12, 29, 7, 18, 10, 35], see Figure 1. The inactivated form corresponds to the state I, and I is always the initial state. After activation, the PA-FP will fluoresce in the F state, from which it will cycle to and from the nonfluorescent D state a number of times (commonly referred to as *blinking*), before permanently photobleaching in the nonfluorescent B state. This 4 state model is the most commonly used, as it is a parsimonious choice that has been found to work well in practice [10], but more complex descriptions have also been investigated [25, 35, 15].

The rate out of I, r_F, depends on the intensity of the activation laser, whereas the remaining rates depend on the excitation laser. For intensities used in practice, the mean activation time can be several minutes, whereas the lifetime (time from activation to absorption in B) is measured in seconds. This means that the fluorescent signal coming from different PA-FP will tend to occur in disjoint windows of time. In particular, even if two PA-FP are closer than the diffraction limit, they can still be distinguished so long as their fluorescent signals are observed separately. To make use of this, PALM records both the spatial and temporal coordinates of fluorescent signals. The entire experiment is recorded by a camera, resulting in a stack of sequential camera frames, each containing the fluorescent signals of a specific time interval.

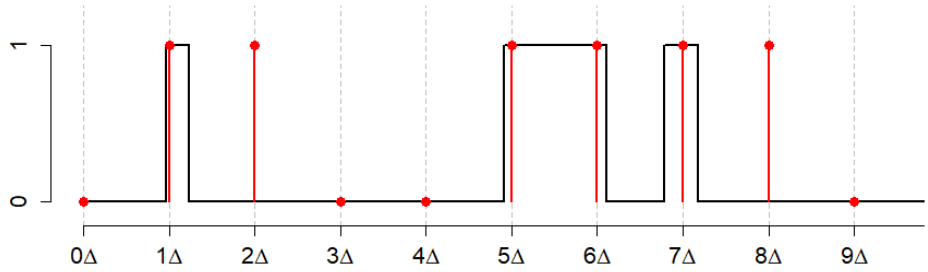

Figure 3: Under an idealized camera, we see each camera frame that overlaps with a visit to the F state. The continuous signal $S(t)$ is shown in black, and the discretized timepoints in $\tilde{S}(k\Delta)$ are in red. In this example, the total fluorescent signal would give rise to 6 appearances of the protein, observed at timepoints $(1\Delta, 2\Delta, 5\Delta, 6\Delta, 7\Delta, 8\Delta)$.

Each frame can then be searched for spots of activity, corresponding to the locations of PA-FPs active at that time, and the spot center coordinates are estimated [34], see Figure 2. In this way, PALM ultimately results in a list of coordinates, resolved with a mean uncertainty in the 10-30nm range [36].

2 Imaging artifacts in PALM

Although PALM is capable of localizing proteins individually, interpretation of the final image is hindered by imaging artifacts. This is in part due to the discretization of the fluorescent signal on camera frames, in part due to the temporary dark state D, and in part due to background noise coming from non-protein sources.

The most problematic imaging artifact is the multiple blinking (or multiple appearances) problem [10, 2], which is multiple inclusions of the same protein. The reason this occurs is easy to realize in light of the switching model of Figure 1, combined with a discretization of the temporal dimension. Consider the fluorescent signal coming from a single PA-FP, and make the indicator process

$$S(t) = \begin{cases} 1 & \text{if the PA-FP is in state } F \text{ at time } t \\ 0 & \text{otherwise.} \end{cases} \tag{2.1}$$

Now, assume the camera operates at a framerate of Δ^{-1}hz, so that the length of a single frame is Δ seconds, and the observable timepoints are then on the form $k\Delta$ for some integer k. The camera in PALM sums the photons on each camera frame when forming an image. Thus, if the camera had perfect sensitivity, such that any non-zero amount of fluorescence could be observed, we would model the activity at timepoint $k\Delta$ with the expression

$$\tilde{S}(k\Delta) = \mathbb{1}_{(0,\Delta]}\left(\int_{\Delta(k-1)}^{\Delta k} S(t)dt\right), \tag{2.2}$$

such that $\tilde{S}(k\Delta) = 1$ corresponds to an observable signal [25]. Depending on the framerate, number of visits to the F state, and the length of each stay in F, there could be several k for which $\tilde{S}(k\Delta) = 1$, see Figure 3. The trouble with these multiple

appearances is that they they can be both spatially and temporally separated by a significant distance, and it then becomes highly nontrivial to attribute them all to the same PA-FP, as there can be nearby signal from several other PA-FP.

In addition to the multiple appearances, it can happen that random bursts of light will find their way into the recording. There are a large number of possible sources of such background noise, and it is not possible to discriminate PA-FPs from background with complete certainty. The amalgamation of all background sources can often be approximated with a Poisson process of random points in the image [27].

3 Correction methods

Localizations that were generated from the same PA-FP will form clusters in space and time, so it is no surprise that most correction methods for multiple blinking artifacts are based on clustering techniques. Most commonly, points are grouped by thresholding of pairwise distances [4], a technique that is built in to most localization software [23]. The general idea is to group points that can be connected by a series of steps no larger than the thresholds. Each group is then merged down to its estimated center, and the uncertainty of the center is computed on the basis of the uncertainty of each localization in the group.

The problem with all such correction methods is that they rely on hyperparameters. For the dense samples encountered in practice, the correct choice of hyperparameters is far from obvious, while the wrong choice will bias subsequent analysis [3]. Optimal hyperparameters would have to account for the blinking rates of the PA-FP being imaged, which are apriori unknown. Although blinking artifacts have the potential to seriously bias studies on proteins, correction details are often absent or poorly justified in SMLM studies [11, 26, 20].

One way to make a well-founded choice of correction method is through calibration data. Calibration data consists of specially procured samples of PA-FP, sparsely and randomly positioned on a large surface. In this way, clustered spots can be assumed to be the multiple appearances of a single protein. The blinking dynamics can then be extracted from the segmented clusters - this can be done simply by exponential curve fitting [19, 10], but more complex description of photoblinking have also been modeled using Hidden Markov Models [25]. Once the blinking rates are known, hyperparameters for correction algorithms can be rigorously chosen; an optimal thresholding method was determined this way in [18].

Although calibration data simplifies statistical analysis greatly, it has two serious drawbacks. First, the preparation and analysis of calibration data is a time and resource drain, especially for experiments involving several conditions. More critically, blinking dynamics are known to depend on both the chosen PA-FP and the experimental conditions [24, 35]. As such, it is unclear whether parameters obtained from a calibration sample are truly transferable to the dataset of interest.

3.1 Corrections tied to specific analyses

Rather than attempt to clean the entire image of artifacts, it may be easier to correct only those analyses that are of interest. For instance, protein clustering is often investigated by means of Ripley's K-function [28], so a blinking-corrected K-function

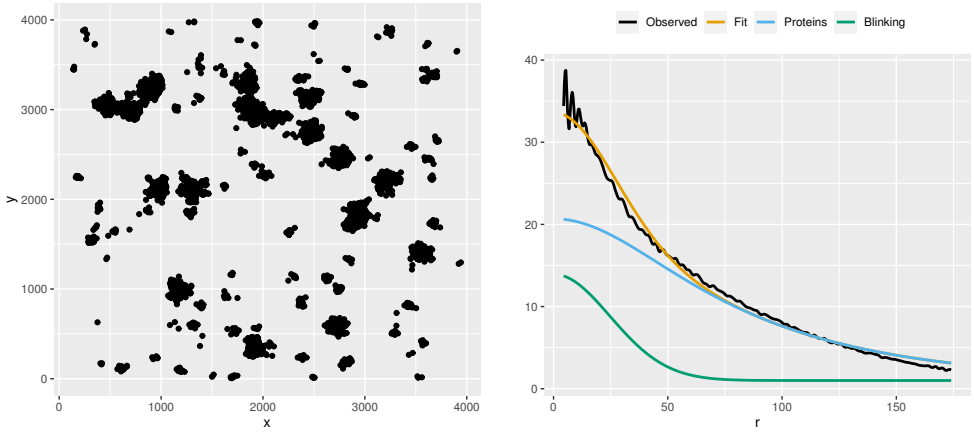

Figure 4: The PC-PALM method takes the observed localizations (left) and splits the observed pair correlation function into contributions from proteins and blinking clusters (right).

is sufficient if no other analyses are desired. Similarly, if counting of proteins is of interest, it is sufficient to know the mean number of appearances per PA-FP [15].

Correcting for blinking in a particular analysis is done by explicitly modeling both proteins and their multiple appearances. Perhaps the most well-known such approach is "PC-PALM", which models the pair correlation function [33, 37]. Under a simple model for the blinking clusters and a Gaussian PSF, and assuming no background noise, the pair correlation function in PALM is shown to split into a blinking and a protein term

$$g_{obs}(x,y) = \frac{1}{4\pi\sigma^2\rho} e^{-\frac{\|x-y\|^2}{4\sigma^2}} + (g_{protein} * \mathrm{PSF})(x,y), \tag{3.1}$$

where g_{obs} is the observed pair correlation function, $g_{protein}$ is the pair correlation function of the true protein coordinates, $*$ indicates convolution, σ is the (assumed known and constant) localization uncertainty, and ρ is a parameter. To use this method, $g_{protein}$ is parameterized by an assumed model for the proteins, and a minimum contrast procedure [22] is used for fitting parameters, see Figure 4. The authors of [33] suggest an exponential term for the proteins, so that

$$g_{proteins}(x,y) = Ae^{-\frac{\|x-y\|}{B}} + 1, \tag{3.2}$$

where A and B are parameters that need to be fit. This choice is of course most natural for modeling of clustered conditions, but it also allows for Poisson proteins as an edge case ($A = 0$). In addition to parameters governing the organization of proteins, the estimated ρ can be used to estimate the number of appearances per protein (under additional modeling assumptions). The PC-PALM method is placed into a larger framework in [1], where a general class of doubly-clustered point process models are constructed, motivated by the hierarchy of real and artificial clusters inherent to PALM, and fit via the pair correlation function.

Other than correlation functions, some work has gone into the correction of protein counts [15, 16, 18]. For instance, in [15], a general parametric form for the probability of observing m localizations from n proteins is derived. Based on counts from several spots, the number of proteins is then obtained via maximum likelihood.

4 A new correction methodology

In paper A we model and estimate PALM artifacts directly from any given dataset. Importantly, the estimation procedures can be carried out without a need to specify the distribution of proteins, making the method universally applicable. On this background, we develop a new correction methodology for PALM in paper B, which can be used without calibration data.

4.1 Paper A and IBCpp models

We introduce the Independent Blinking Cluster point process (IBCpp) family of models for SMLM microscopy. The family consists of spatio-temporal point process models with a cluster structure that is motivated by blinking clusters in SMLM. More specifically, we model the observed data with a process on the form

$$O = \left(\bigcup_{x \in X} Y_x \right) \bigcup E, \tag{4.1}$$

where X is the unobserved process of proteins, Y_x is a blinking cluster associated with the protein $x \in X$, and E is a space-time background noise process. The noise process has intensity function

$$\lambda_E(e, t_e) = \lambda_{\downarrow E} \frac{\mathbb{1}(t_e \leq b)}{b}, \tag{4.2}$$

where b is the length of the SMLM experiment in seconds, and $0 \leq \lambda_{\downarrow E} < \infty$ is the spatial noise intensity. The blinking clusters are assumed independent and on the form

$$Y_x = \bigcup_{i=1}^{G} (x + \epsilon_i, t_{y_i}), \tag{4.3}$$

where the ϵ_i are centered i.i.d. localization errors, G is the total number of appearances of the protein, and t_{y_i} is the time at which localization i was observed. The timepoints and G are allowed to depend on eachother, but we require both G and the timepoints to be independent of the localization errors.

This construction is natural for SMLM; note first that the collection $\{Y_x\}_{x \in X}$ is assumed independent, just as fluorophores in SMLM are assumed to be independent [15, 29, 35]. Each location is on the form $x + \epsilon_i$, corresponding to a noisy observation of the true protein location, with the noise being the result of PSF fitting to the pixellated fluorescent signal. The distribution of G and $\{t_{y_i}\}_{i=1}^{G}$ are left unspecified in general, as their distribution can differ between SMLM modalities. By putting specific distributional assumptions on G, ϵ_i, and the timepoints, we create the PALM-IBCpp which is tailored to PALM data, the main focus of paper A. Specifically, the timepoints and G are determined from the discretized 4-state model of PA-FP photophysics, as in Figure 3.

For a general IBCpp process, we show a useful result for the mark correlation function. Denote by k_O^f the mark correlation function of O under a symmetrical non-negative function f, and by $g_{\downarrow O}$ the (spatial) pair correlation function of O. Given

a stationary and rotation invariant X, we then find

$$\gamma_2^O(f)k_O^f(r)g_{\downarrow O}(r) = (\gamma_1(f)-\gamma_2(f))\left[\frac{\eta}{\lambda_{\downarrow O}}n_c(h_\epsilon * h_\epsilon)(r)\right]+\gamma_2(f)\left[g_{\downarrow O}(r)-1\right]+\gamma_2^O(f). \quad (4.4)$$

The involved quantities are explained in full in paper A, and will not be explained again here in the interest of brevity. The first takeaway is that the γ's and n_c are functions only of the distribution of timepoints and G, and in particular independent of the locations in O. The second takeaway is that the distribution of X enters only through $g_{\downarrow O}$, which can be nonparametrically estimated. Finally, the term $(h_\epsilon * h_\epsilon)$ is just the autoconvolution of the PSF, and this can be estimated from the localization uncertainties, which are always included in SMLM data.

We devise a way to estimate the background noise intensity, and combining this with Equation (4.4), we show that the quantities

$$\zeta(f) = (\gamma_1(f)-\gamma_2(f))\,n_c, \quad (4.5)$$

can be estimated for any f, without parametric assumptions on X. For each choice of f, $\zeta(f)$ contains information about the process that generated the timepoints, and hence the blinking artifacts. We pick a collection of functions $\{f_u\}_{u\in T}$ indexed by a set T, and solve a weighted minimum contrast [22] problem between $\hat{\zeta}(f_u)$ and $\zeta(f_u)$. We derive expressions for $\zeta(f_u)$ in the PALM-IBCpp, on the basis of which three of the four blinking rates can be estimated. The last blinking rate is estimated separately afterwards, using an estimating equation.

Although we motivate the estimation procedures on stationary and rotation invariant X, we show that the same techniques can be expected to work for arbitrary X. Thus, we are in a position to estimate the parameters that control imaging artifacts in a general setting.

4.2 Paper B and the MBC algorithm for artifact removal

With the artifact parameters now estimable from arbitrary data, it is natural to want to use them for correction. To that end, we develop the Model-Based Correction (MBC) algorithm for PALM artifacts, which is built on a Bayesian model for the spatio-temporal data. We imagine the data as a set of coordinates $(X_i, Y_i)_{i=1}^n$ in $\mathbb{R}^2$, with associated timepoints $\{T_i\}_{i=1}^n$. Additionally, we have access to localization uncertainties $\{\sigma_i\}_{i=1}^n$ associated with each localization. We observe the data in the spatial window $R = [x_0, x_1] \times [y_0, y_1]$, which we refer to as the region of interest (ROI).

We let a data partitioning with N categories be given, such that the partition postulates which points belong to the same blinking cluster (or is noise). We are interested in the posterior probability of this partition given the data, which provides a basis for choosing between different partitions. By using this posterior as a scoring scheme, we combine it with a clustering algorithm to find a likely candidate for the artifact-free image, an idea that was inspired by [30]. We put a uniform prior on the partitions, and it then turns out that we need only compute the converse posterior of the data given the partition. This is because maximization of the two posteriors with respect to the partition is then equivalent by Bayes' theorem.

Using a similar model for blinking clusters and background noise as in paper A, points belonging to different partition groups are independent. Starting with non-

noise points, a particular cluster $(X_i, Y_i, T_i)_{i=1}^m$ of size $m \leq n$ with true protein location $\mu = (\mu_x, \mu_y)$, has conditional probability given the partition and μ that is factorizable as

$$P((X_i, Y_i, T_i)_{i=1}^m|\mu) = P((X_i)_{i=1}^m|\mu)P((Y_i)_{i=1}^m|\mu)P((T_i)_{i=1}^m), \tag{4.6}$$

where we show that $P((X_i)_{i=1}^m|\mu)$ is given as

$$P((X_i)_{i=1}^m \mid \mu) = (2\pi)^{-\frac{m}{2}} \left(\prod_{i=1}^m \sigma_i\right)^{-1} exp\left\{-\frac{1}{2}\sum_{i=1}^m \eta_i \left(X_i - \tilde{X}\right)^2\right\} exp\left\{-\frac{\sum_{i=1}^m \eta_i}{2}\left(\mu_x - \tilde{X}\right)^2\right\}, \tag{4.7}$$

with

$$\eta_i = \frac{1}{\sigma_i^2} \tag{4.8}$$

$$\tilde{X} = \frac{\sum_{i=1}^m \eta_i X_i}{\sum_{i=1}^m \eta_i}. \tag{4.9}$$

We place a uniform prior on μ over the ROI, and show that the marginal posterior is

$$P((X_i)_{i=1}^m) = (2\pi)^{-\frac{m}{2}} \left(\prod_{i=1}^m \sigma_i\right)^{-1} exp\left\{-\frac{1}{2}\sum_{i=1}^m \eta_i \left(X_i - \tilde{X}\right)^2\right\} \tag{4.10}$$

$$\times (x_1 - x_0)^{-1}(2\pi)^{\frac{1}{2}} \left(\sum_{i=1}^m \eta_i\right)^{-\frac{1}{2}} \left\{\Phi\left(\frac{x_1 - \tilde{X}}{\left(\sum_{i=1}^m \eta_i\right)^{-\frac{1}{2}}}\right) - \Phi\left(\frac{x_0 - \tilde{X}}{\left(\sum_{i=1}^m \eta_i\right)^{-\frac{1}{2}}}\right)\right\}, \tag{4.11}$$

where Φ is the CDF of the standard normal distribution. The expression for $P((Y_i)_{i=1}^m)$ is computed identically. For the timepoints, we show that

$$P((T_i)_{i=1}^m) = P(u)P(T_{min})(1-p)^{n_f} \prod_{k=1}^{n_F} P(f_k) \prod_{k=1}^{n_F - 1} P(d_k), \tag{4.12}$$

where

$$p = \frac{r_B}{r_D + r_B}, \tag{4.13}$$

is the probability of bleaching (an $F \to B$ transition), and n_F is the number of F state visits. f_k and d_k are respectively the length of stay in the k'th visit to the F and D state. All these quantities are computed on the basis of the sorted timepoints; to accomplish this, we ignore discretization errors, and set f_k to be the length of the k'th unbroken streak of contiguous frames of activity in the sorted timepoints. The dark times d_k are computed similarly, but for the lengths of the gaps in the fluorescent activity. Finally, T_{min} is the smallest observed timepoint, and u is the time between the last observed fluorescent activity and the end of the experiment. Given the 4-state PA-FP model, we then find that

$$P(T_{min}) = r_F e^{-r_F \min_i T_i} \tag{4.14}$$

$$P(f_k) = (r_D + r_B)e^{-(r_D + r_B)f_k} \tag{4.15}$$

$$P(d_k) = r_R e^{-r_R d_k} \tag{4.16}$$

$$P(u) = (1-p)e^{-r_R u} + p, \tag{4.17}$$

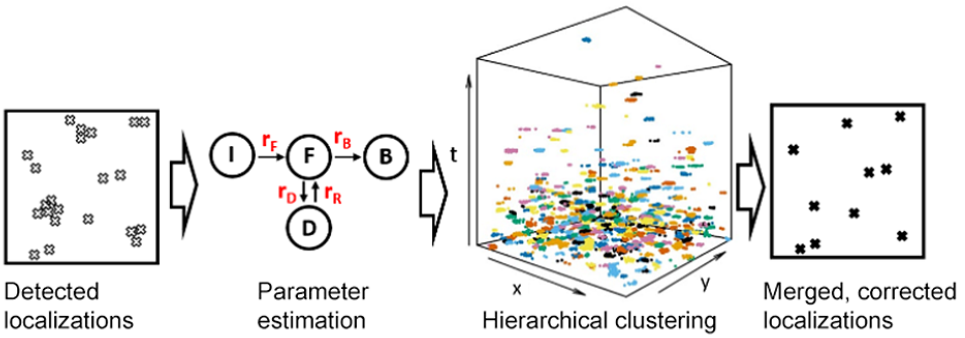

Figure 5: The MBC workflow. The localizations, timepoints, and localization uncertainties are given as input to the algorithm. On this basis, the artifact parameters are estimated, and several clustering proposals are then considered and scored via their posterior probability. The best proposal is used to construct a corrected dataset.

where $P(u)$ comes from the possibility that the blinking cluster could have continued after the end of the experiment, given a sufficiently long dark state visit. Finally, by allowing for uniform noise points with probability α, the final probability of the group is shown to be

$$\pi((X_i)_{i=1}^m,(Y_i)_{i=1}^m,(T_i)_{i=1}^m) = \begin{cases} (1-\alpha)P((X_i)_{i=1}^m,(Y_i)_{i=1}^m,(T_i)_{i=1}^m) & m>1 \\ \alpha V^{-1} + (1-\alpha)P(P((X_i)_{i=1}^m,(Y_i)_{i=1}^m,(T_i)_{i=1}^m)) & m=1, \end{cases} \tag{4.18}$$

where $V = T(x_1 - x_0)(y_1 - y_0)$ and T is the length of the PALM recording. Since the clusters are independent, the posterior probability of all data is then given simply as the product over the groups.

In order to find a likely partition of the data, corresponding to the blinking clusters and noise points, we then use the following two step procedure (see Figure 5). First, we estimate the blinking rates and α via paper A, and using these we can then immediately compute the posterior probability of a given partition. The parameters also provide us with an estimate of N, the total number of groups to look for in the partition. Next, as direct maximization over partitions is a notoriously hard undertaking, we must be satisfied with approximations. One way to get good solutions is to use a clustering algorithm that respects the nature of the clusters we expect to find. Particularly, as blinking clusters are Gaussian in space and i.i.d., we should expect reasonably compact and homogeneous clusters. To do this in a way that is fast and easy to implement, we use a custom hierarhical clustering (HC) [8] algorithm. HC computes all pairwise distances between points using any desired metric (or dissimilarity measure). The distances are generalized to clusters by means of a linkage criterion, and the algorithm merges the closest clusters in a greedy fashion until a partition with a desired number of clusters is achieved. The choice of metric and linkage criterion determine the sort of clusters found. We chose Ward's linkage criterion [8] which is well-suited for compact clusters. For the metric, let spacetime locations (X_1, Y_1, T_1) and (X_2, Y_2, T_2) with associated uncertainties σ_1 and σ_2 be given. Then, we define the distance between them as

$$d_S((X_1,Y,T_1),(X_2,Y,T_2)) = \frac{\|(X_1,Y_1)-(X_2,Y_2)\|}{\sigma_1+\sigma_2} + S\cdot|T_1-T_2|, \tag{4.19}$$

where $S \geq 0$ is a tuneable parameter. This distance weighs spatial distance by uncertainty, and the temporal distance by S. By varying S, and fixing the number of clusters to find at N, we get a large number of likely partitions to choose from, which we accomplish by comparing their posterior probabilities. Finally, we take each found blinking cluster and estimate its center by maximum likelihood, which corresponds to taking the inverse variance weighted average, and compute an updated localization uncertainty, reflecting the increased certainty about the protein position.

It should be noted that many other clustering algorithms could be considered. For the revised version of paper B, we will also look at the Bayesian hierarchical clustering [13] algorithm, which attempts to directly maximize the posterior in a greedy fashion.

References

[1] Andersen, I.T., U. Hahn, E.C. Arnspang, L.N. Nejsum and E.B.V. Jensen (2018). Double Cox cluster processes — with applications to photoactivated localization microscopy. *Spatial Statistics* 27, 58–73. DOI: 10.1016/j.spasta.2018.04.009.

[2] Annibale, P., M. Scarselli, A. Kodiyan and A. Radenovic (Apr. 2010). Photoactivatable Fluorescent Protein mEos2 Displays Repeated Photoactivation after a Long-Lived Dark State in the Red Photoconverted Form. *The Journal of Physical Chemistry Letters* 1(9), 1506–1510. DOI: 10.1021/jz1003523.

[3] Annibale, P., S. Vanni, M. Scarselli, U. Rothlisberger and A. Radenovic (2011a). Identification of clustering artifacts in photoactivated localization microscopy. *Nature methods* 8(7), 527.

[4] Annibale, P., S. Vanni, M. Scarselli, U. Rothlisberger and A. Radenovic (2011b). Quantitative photo activated localization microscopy: unraveling the effects of photoblinking. *PloS one* 6(7), e22678.

[5] Betzig, E., G.H. Patterson, R. Sougrat, O.W. Lindwasser, S. Olenych, J.S. Bonifacino, M.W. Davidson, J. Lippincott-Schwartz and H.F. Hess (2006). Imaging intracellular fluorescent proteins at nanometer resolution. *Science* 313(5793), 1642–1645.

[6] Chudakov, D.M, M.V. Matz, S. Lukyanov and K.A. Lukyanov (July 2010). Fluorescent Proteins and Their Applications in Imaging Living Cells and Tissues. *Physiological Reviews* 90(3), 1103–1163. DOI: 10.1152/physrev.00038.2009.

[7] Coltharp, C., R.P Kessler and J. Xiao (2012). Accurate construction of photoactivated localization microscopy (PALM) images for quantitative measurements. *PLoS One* 7(12), e51725.

[8] Cormack, R.M (1971). A Review of Classification. *Journal of the Royal Statistical Society. Series A (General)* 134(3), 321. DOI: 10.2307/2344237.

[9] Deschout, H., F.C. Zanacchi, M. Mlodzianoski, A. Diaspro, J. Bewersdorf, S. T. Hess and K. Braeckmans (2014). Precisely and accurately localizing single emitters in fluorescence microscopy. *Nature methods* 11(3), 253.

[10] Fricke, F., J. Beaudouin, R. Eils and M. Heilemann (2015). One, two or three? Probing the stoichiometry of membrane proteins by single-molecule localization microscopy. *Scientific reports* 5, 14072.

[11] Greenfield, D., A.L. McEvoy, H. Shroff, G.E. Crooks, N.S. Wingreen, E. Betzig and J. Liphardt (June 2009). Self-Organization of the Escherichia coli Chemotaxis Network Imaged with Super-Resolution Light Microscopy. *PLoS Biology* 7(6). Ed. by H.C. Berg, e1000137. DOI: 10.1371/journal.pbio.1000137.

[12] Griffié, J., T. Pham, C. Sieben, R. Lang, V. Cevher, S. Holden, M. Unser, S. Manley and D. Sage (Mar. 2020). Virtual-SMLM, a virtual environment for real-time interactive SMLM acquisition. DOI: 10.1101/2020.03.05.967893.

[13] Heller, K.A. and Z. Ghahramani (2005). "Bayesian hierarchical clustering". *Proceedings of the 22nd international conference on Machine learning - ICML '05*. ACM Press. DOI: 10.1145/1102351.1102389.

[14] Huang, B., M. Bates and X. Zhuang (June 2009). Super-Resolution Fluorescence Microscopy. *Annual Review of Biochemistry* 78(1), 993–1016. DOI: 10.1146/annurev.biochem.77.061906.092014.

[15] Hummer, G., F. Fricke and M. Heilemann (2016). Model-independent counting of molecules in single-molecule localization microscopy. *Molecular biology of the cell* 27(22), 3637–3644.

[16] Karathanasis, C., F. Fricke, G. Hummer and M. Heilemann (2017). Molecule counts in localization microscopy with organic fluorophores. *ChemPhysChem* 18(8), 942–948.

[17] Klein, T., S. Proppert and M. Sauer (Feb. 2014). Eight years of single-molecule localization microscopy. *Histochemistry and Cell Biology* 141(6), 561–575. DOI: 10.1007/s00418-014-1184-3.

[18] Lee, S.-H., J.Y. Shin, A. Lee and C. Bustamante (Oct. 2012). Counting single photoactivatable fluorescent molecules by photoactivated localization microscopy (PALM). *Proceedings of the National Academy of Sciences* 109(43), 17436–17441. DOI: 10.1073/pnas.1215175109.

[19] Lin, Y., J.J. Long, F. Huang, W.C. Duim, S. Kirschbaum, Y. Zhang, L.K. Schroeder, A.A. Rebane, M.G.M Velasco, A. Virrueta, et al. (2015). Quantifying and optimizing single-molecule switching nanoscopy at high speeds. *PloS one* 10(5), e0128135.

[20] Malkusch, S., W. Muranyi, B. Müller, H.-G. Kräusslich and M. Heilemann (Aug. 2012). Single-molecule coordinate-based analysis of the morphology of HIV-1 assembly sites with near-molecular spatial resolution. *Histochemistry and Cell Biology* 139(1), 173–179. DOI: 10.1007/s00418-012-1014-4.

[21] Moerner, W.E. (July 2007). New directions in single-molecule imaging and analysis. *Proceedings of the National Academy of Sciences* 104(31), 12596–12602. DOI: 10.1073/pnas.0610081104.

[22] Møller, J. and R. Waagepetersen (2004). *Statistical inference and simulation for spatial point processes*. Boca Raton: Chapman & Hall/CRC.

[23] Ovesny, M., P. Křižek, J. Borkovec, Z. Švindrych and G.M Hagen (2014). ThunderSTORM: a comprehensive ImageJ plug-in for PALM and STORM data analysis and super-resolution imaging. *Bioinformatics* 30(16), 2389–2390.

[24] Pageon, S.V., P.R. Nicovich, M. Mollazade, T. Tabarin and K. Gaus (Nov. 2016). Clus-DoC: a combined cluster detection and colocalization analysis for single-molecule localization microscopy data. *Molecular Biology of the Cell* 27(22). Ed. by D. Lidke, 3627–3636. DOI: 10.1091/mbc.e16-07-0478.

[25] Patel, L., N. Gustafsson, Y. Lin, R. Ober, R. Henriques, E. Cohen, et al. (2019). A hidden Markov model approach to characterizing the photo-switching behavior of fluorophores. *The Annals of Applied Statistics* 13(3), 1397–1429.

[26] Pereira, C.F., J. Rossy, D.M Owen, J. Mak and K. Gaus (2012). HIV taken by STORM: Super-resolution fluorescence microscopy of a viral infection. *Virology Journal* 9(1), 84. DOI: 10.1186/1743-422x-9-84.

[27] Peterson, E.M and J.M Harris (Dec. 2009). Quantitative Detection of Single Molecules in Fluorescence Microscopy Images. *Analytical Chemistry* 82(1), 189–196. DOI: 10.1021/ac901710t.

[28] Ripley, B.D. (June 1976). The second-order analysis of stationary point processes. *Journal of Applied Probability* 13(2), 255–266. DOI: 10.2307/3212829.

[29] Rollins, G.C., J.Y. Shin, C. Bustamante and S. Presse (2015). Stochastic approach to the molecular counting problem in superresolution microscopy. *Proceedings of the National Academy of Sciences* 112(2), E110–E118.

[30] Rubin-Delanchy, P., G.L. Burn, J. Griffié, D.J. Williamson, N.A. Heard, A.P Cope and D.M Owen (Oct. 2015). Bayesian cluster identification in single-molecule localization microscopy data. *Nature Methods* 12(11), 1072–1076. DOI: 10.1038/nmeth.3612.

[31] Sahl, S.J., A. Schönle and S.W. Hell (2019). "Fluorescence Microscopy with Nanometer Resolution". *Springer Handbook of Microscopy*. Ed. by P.W. Hawkes and J.C.H. Spence. Cham: Springer International Publishing, 1089–1143. DOI: 10.1007/978-3-030-00069-1_22.

[32] Schermelleh, L., R. Heintzmann and H. Leonhardt (July 2010). A guide to super-resolution fluorescence microscopy. *Journal of Cell Biology* 190(2), 165–175. DOI: 10.1083/jcb.201002018.

[33] Sengupta, P., T. Jovanovic-Talisman, D. Skoko, M. Renz, S.L. Veatch and J. Lippincott-Schwartz (2011). Probing protein heterogeneity in the plasma membrane using PALM and pair correlation analysis. *Nature methods* 8(11), 969.

[34] Small, A. and S. Stahlheber (2014). Fluorophore localization algorithms for super-resolution microscopy. *Nature methods* 11(3), 267.

[35] Staudt, T., T. Aspelmeier, O. Laitenberger, C. Geisler, A. Egner, A. Munk, et al. (2020). Statistical Molecule Counting in Super-Resolution Fluorescence Microscopy: Towards Quantitative Nanoscopy. *Statistical Science* 35(1), 92–111.

[36] Temprine, K., A.G. York and H. Shroff (Oct. 2014). "Three-Dimensional Photoactivated Localization Microscopy with Genetically Expressed Probes". *Methods in Molecular Biology*. Springer New York, 231–261. DOI: 10.1007/978-1-4939-2080-8_13.

[37] Veatch, S.L., B.B. Machta, S.A. Shelby, E.N. Chiang, D.A. Holowka and B.A. Baird (Feb. 2012). Correlation Functions Quantify Super-Resolution Images and Estimate Apparent Clustering Due to Over-Counting. *PLoS ONE* 7(2). Ed. by J. Rao, e31457. DOI: 10.1371/journal.pone.0031457.

[38] Wardyn, J.D. and A.D. Jeyasekharan (2018). "Immunofluorescence". *eLS*. American Cancer Society, 1–9. DOI: https://doi.org/10.1002/9780470015902.a0001174.pub2. eprint: https://onlinelibrary.wiley.com/doi/pdf/10.1002/9780470015902.a0001174.pub2.

PAPER A

Semiparametric point process modeling of blinking artifacts in PALM.

Louis G. Jensen, David J. Williamson, Ute Hahn

In review (revision round 1) at *The Annals of Applied Statistics*.

Abstract

Photoactivated localization microscopy (PALM) is a powerful imaging technique for characterization of protein organization in biological cells. Due to the stochastic blinking of fluorescent probes, and camera discretization effects, each protein gives rise to a cluster of artificial observations. These blinking artifacts are an obstacle for quantitative analysis of PALM data, and tools for their correction are in high demand. We develop the Independent Blinking Cluster point process (IBCpp) family of models, which is suited for modeling of data from single-molecule localization microscopy modalities, and we present results on the mark correlation function. We then construct the PALM-IBCpp - a semiparametric IBCpp tailored for PALM data, and we describe a procedure for estimation of parameters, which can be used without parametric assumptions on the spatial organization of proteins. Our model is validated on nuclear pore complex reference data, where the ground truth was accurately recovered, and we demonstrate how the estimated blinking parameters can be used to perform a blinking corrected test for protein clustering in a cell expressing the adaptor protein LAT. Finally, we consider simulations with varying degrees of blinking and protein clustering to shed light on the expected performance in a range of realistic settings.

Keywords: Photoactivated localization microscopy; Multiple blinking; Spatiotemporal point patterns; Mark correlation function; Moment-based estimation; Second-order characteristics

A.1 Introduction

Breaking the resolution limit imposed on classical fluorescence microscopy has been made possible by the advent of super resolution methods [12]. Among these, PALM [5] has become a popular tool for the acquisition of point maps of individual molecules, achieved by the use of photoactivatable fluorescent proteins (PA-FPs). PA-FPs can be activated, read, and permanently photobleached in stochastic fashion. The resulting separation of fluorescent signal in time-space will, with high probability, be sufficient to individually localize the PA-FPs present in a given sample [39].

Unfortunately, it is the nature of PA-FPs to enter and reemerge from dark states a number of times before permanently bleaching, leading to multiple appearances of the same protein [3, 9]. For analysis of the spatial organization of molecules, these reappearances lead to erroneous conclusions, unless explicitly dealt with [30]. In particular, analysis of the clustering properties of proteins, a common goal in PALM studies, is an increasingly contentious topic [26]. Making matters worse, direct modeling of the blinking artifacts is complicated due to camera discretization of the continuous fluorescent signals [11, 22], and an understanding of both PA-FP photophysics and discretization effects is required to properly remedy the situation.

Although such artifacts are best understood by considering the spatio-temporal behavior of PA-FPs, established methods for analysis of blinking artifacts have so far focused on one dimension or the other. In methods such as [1, 29], the spatial data alone is used, and require a model for protein behavior. Other methods use the temporal fluorescence traces to estimate the number of proteins in local regions [13, 15, 18], which require either manual segmentation or external calibration samples. More recently, complex descriptions of PA-FP photophysics have been modeled by means of Hidden Markov Models (HMM) [33, 22]. In [22], estimation is carried out by means of a calibration sample of well-separated fluorophores. More recently, [33] model the conglomerate fluorescent intensity trace over a sequence of time points, as originating from some unknown number of PA-FP. This means that additional parameters have to be estimated, and the information in the spatial dimension is not exploited.

In this paper, we define the family of Independent Blinking Cluster point processes (IBCpp) for single-molecule localization microscopy (SMLM) data, and present a result on the mark correlation function that is useful for estimation. We propose a particular model from the family, the PALM-IBCpp, for modeling of PALM data, and motivate the construction in terms of a discretized, 4-state PA-FP blinking model. We present an algorithm for estimating the parameters that control data artifacts, which can be run quickly even on large datasets. Our approach leads to estimates of the kinetic rates that govern photoblinking, which can be used to quantify the effect of blinking artifacts on a given sample, and correct downstream analyses for blinking induced biases. The modeling efforts are validate on established reference data of nuclear pore complexes (NUP) [36].

To help facilitate the debate on whether real protein clustering is present in a given sample, we devise a blinking corrected test for complete spatial randomness (CSR) on the basis of estimated blinking dynamics, and demonstrate it on a real biological sample of a cell expressing the protein Linker for Activation of T cells (LAT), observed at the plasma membrane. In this way, we can show that there are both

areas of significant and non-significant protein clustering at different sites in the cell. This analysis serves as an example on the use of this universal test, and additionally provides yet more evidence for protein clustering in LAT, a research area of interest in its own right [38].

The paper is organized as follows. In Section A.2, we briefly go over the needed point process theory that will be used for modeling or estimation, and we give a quick rundown of the principles of PALM imaging, and how camera artifacts come into play. In Section A.3, we define the IBCpp class of models, and present a useful result on the mark correlation function. We then construct and motivate the PALM-IBCpp for modeling of PALM data.. In Section A.4, we describe an algorithm for estimation of the kinetic rates in the PA-FP blinking model. We validate our methods on nuclear pore complex reference data in Section A.5 by demonstrating a close alignment with expected blinking targets. Section A.6 considers a dataset expressing LAT-mEos3.2 PA-FP, and we demonstrate how a blinking corrected CSR test can be performed on the basis of estimated blinking dynamics. Finally, in Section A.7, we simulate PA-FP with a range of different spatial organizations and blinking behaviors, and illustrate the ability of our estimation methods to precisely recover the kinetic rates. We also consider what happens when the blinking model is misspecified, and we find that important PA-FP descriptors, such as the total number of reappearances and time to activation and bleaching, can still be recovered.

A.2 Prerequisites

In this section we present the notation and point process concepts that we will be needing below, including moment measures, mark distributions, and the mark correlation function. We also describe some of the modeling difficulties that arise in SMLM experiments, namely those associated with discretization of the temporal information and background noise. For the general exposition, we work with processes on $\mathbb{R}^d \times \mathbb{R}_+$, but it is instructive to imagine $d = 2$, corresponding to 2D microscopy, which is the most common modality. For a more rigorous introduction to point process theory, we refer to [7]. For more on mark distributions, see [34]. Finally, more on the acquisition and preparation of SMLM data can be found in [8].

A.2.1 Point processes and moment measures

For the purpose of this paper, a spatio-temporal point process, $V = \{(v_i, t_{v_i})\}_{i=1}^{\infty}$, is a random, locally finite point configuration with distinct points in $\mathbb{R}^d \times \mathbb{R}_+$. We call V stationary if

$$V \overset{d}{=} V + s = \{v_i + s, t_{v_i}\}_{i=1}^{\infty}, \tag{A.2.1}$$

for all $s \in \mathbb{R}^d$, where $\overset{d}{=}$ denotes equality in distribution. Similarly, we call V rotation-invariant if

$$V \overset{d}{=} RV = \{Rv_i, t_{v_i}\}_{i=1}^{\infty}, \tag{A.2.2}$$

for any rotation R. If V is both stationary and rotation-invariant, it is motion-invariant.

Write $\downarrow V = \{v_i\}_{i=1}^{\infty}$ (*ground* V) for the random object obtained by stripping V of its times. Assume $\downarrow V$ is well-defined as a spatial point process on $\mathbb{R}^d$, having finite

intensity function $\lambda_{\downarrow V}$ and second-order product density $\lambda^{(2)}_{\downarrow V}$. Then we compute the (ground) intensity measure, $\Lambda_{\downarrow V}$, and (ground) second-order factorial moment measure, $\alpha^{(2)}_{\downarrow V}$, as

$$\Lambda_{\downarrow V}(A) = \mathbb{E}\left[\sum_{v\in\downarrow V} \mathbb{1}_A(v)\right] = \int_A \lambda_{\downarrow V}(v)dv, \tag{A.2.3}$$

$$\alpha^{(2)}_{\downarrow V}(A_1 \times A_2) = \mathbb{E}\left[\sum^{\neq}_{(v_1,v_2)\in\downarrow V^2} \mathbb{1}_{A_1\times A_2}(v_1, v_2)\right] = \int_{A_1\times A_2} \lambda^{(2)}_{\downarrow V}(v_1, v_2)d(v_1, v_2), \tag{A.2.4}$$

working everywhere on Borel sets, and $\sum^{\neq}$ means summation over distinct pairs of points. The pair correlation function $g_{\downarrow V}$ is then defined in the usual way

$$g_{\downarrow V}(v_1, v_2) = \frac{\lambda^{(2)}_{\downarrow V}(v_1, v_2)}{\lambda_{\downarrow V}(v_1)\lambda_{\downarrow V}(v_2)}. \tag{A.2.5}$$

Next, the 1-point mark distribution, $M^{(1)}_{V|v}$, is defined via the space-time intensity measure. When it exists, it is the conditional probability measure on $\mathbb{R}_+$ satisfying

$$\Lambda_V(A \times B) = \mathbb{E}\left[\sum_{(v,t_v)\in V} \mathbb{1}_A(v)\mathbb{1}_B(t_v)\right] = \int_A M^{(1)}_{V|v}(B)d\Lambda_{\downarrow V}(v). \tag{A.2.6}$$

Similarly, the *2-point mark distribution*, $M^{(2)}_{V|(v_1,v_2)}$, satisfies the conditional measure representation of the space-time second-order factorial moment measure

$$\alpha^{(2)}_V(\times^2_{k=1}[A_k \times B_k]) = \mathbb{E}\left[\sum^{\neq}_{(v_1,t_{v_1}),(v_2,t_{v_2})\in V^2} \mathbb{1}_{A_1\times A_2}(v_1, v_2)\mathbb{1}_{B_1\times B_2}(t_{v_1}, t_{v_2})\right] \tag{A.2.7}$$

$$= \int_{A_1\times A_2} M^{(2)}_{V|(v_1,v_2)}(B_1 \times B_2)d\alpha^{(2)}_{\downarrow V}(v_1, v_2). \tag{A.2.8}$$

From these conditional measures, the mark correlation function, k^f_V, is defined as

$$k^f_V(v_1, v_2) = \frac{\int f(t_{v_1}, t_{v_2})dM^{(2)}_{V|(v_1,v_2)}(t_{v_1}, t_{v_2})}{\int\int f(t_{v_1}, t_{v_2})dM^{(1)}_{V|v_1}(t_{v_1})dM^{(1)}_{V|v_2}(t_{v_2})}, \tag{A.2.9}$$

for $f : \mathbb{R}^2_+ \mapsto \mathbb{R}_+$ a non-negative Borel function of two times. We will refer to f as a *query function*.

A.2.2 PALM, discretization, and noise

To understand how PALM works, we imagine a single PA-FP located at the position x. Whenever fluorescence is emitted, it is captured by the camera, and the signal is integrated over the acquisition time lasting 1 frame. Based on the intensity profile observed on pixels, the position x is estimated, by assuming a shape for the point spread function (PSF) [32, 20], which models the blurry shape observed on a camera

when imaging a point-source of light. The localization uncertainty associated with the estimate of x can then be computed, and is included in the dataset for each localization. This localization procedure is possible because we assumed only a single, isolated fluorescent emitter. In a real biological sample, there can be several emitters at nearly the same position, and the assumption of an isolated signal is thus often violated. However, if we only receive a signal of finite length from each emitter, in non-overlapping windows of time, the spatial proximity becomes irrelevant, and we can again determine the position of each emitter. In PALM, this temporal separation is made possible using PA-FPs, which activate at different times, and turn off permanently after finite emission of fluorescence. In this way, only a single emitter should be active at a given space-time location, and it can then be precisely localized.

Note that, using the procedure outlined above, each emitter will give rise to several localizations. To see why this is true, assume that the PA-FP at position x sends out a (sufficiently bright) signal lasting in total T seconds, and the frame acquisition time is Δ seconds. We can then expect the signal to result in roughly $T\Delta^{-1}$ estimates of x, all of which will be included in the sample as separate localizations. Depending on the total fluorescence observed from the PA-FPs, and the camera framerate, this can lead to a large number of reappearances per protein. It is natural to think that this problem can be solved by grouping localization that are close in space-time, and although such procedures are often used in practice [2, 17], they are typically heuristic in nature due to the lack of precise knowledge about the temporal behavior of the PA-FPs in the sample. Without such knowledge, we have no principled guide for determining the merging thresholds, which must allow both for varying spatial uncertainty, and extended temporal separation occurring due to PA-FPs visiting dark states. As a result, localizations arising from the same emitter can be easily confused with those arising from a nearby, or nonexistent, emitter.

In addition to reappearances, background noise will invariably affect the dataset. Each time fluorescence is observed on the camera, it must be attributed as spurious background or coming from a PA-FP emission event, by means of a separating threshold. Since we cannot set the threshold too high without losing the signal of real PA-FP, some background noise points will always be present in PALM recordings.

A.3 Independent Blinking Cluster point processes

In this section we introduce and motivate the IBCpp family of models, which is a subset of clustered spatio-temporal point processes with a particular spatio-temporal clustering structure that is natural for modeling of SMLM data. We then consider a moment result with particular importance for parameter estimation. Finally, we construct the PALM-IBCpp, which is a semiparametric IBCpp model tailored for PALM data.

A.3.1 Definition

A point process following the IBCpp model, denoted by O throughout, has 3 components: the process of protein locations, ${}_{\downarrow}X$, the blinking cluster of all localizations and timepoints associated with a protein x, Y_x, and an independent Poisson process of noise points, E. The IBCpp O is then constructed hierarchically as the union of all

blinking clusters, Z, with the noise process, E, as

$$O = Z \bigcup E, \tag{A.3.1}$$

$$Z = \bigcup_{x \in X} Y_x, \tag{A.3.2}$$

where we assume the blinking clusters are independent of eachother, and of the form

$$Y_x = \bigcup_{i=1}^{G} (x + \epsilon_i, t_{y_i}), \tag{A.3.3}$$

where the ϵ_i are i.i.d. with distribution P_ϵ, and further independent of $\{t_{y_i}\}_{i=1}^G$ and G. Finally, the spatio-temporal intensity of the noise process is assumed to be on the form

$$\lambda_E(e, t_e) = \lambda_{\downarrow E} \frac{\mathbb{1}(t_e \leq b)}{b}, \tag{A.3.4}$$

where b is the length (in seconds) of the data recording and $0 \leq \lambda_{\downarrow E} < \infty$.

To explain why this construction is natural for SMLM data, we now consider each component and assumption above in more detail. Starting with the overall structure of O, essentially all SMLM modalities should be modeled naturally with this general idea of (possibly repeated) noisy observations of the proteins in the sample, corrupted by spurious background noise. This is certainly the case for commonly used modalities such as PALM, STORM [27], DNA-PAINT [28], and many others.

The real meat of the definition is in the parametrization of a blinking cluster, Y_x, and the dependence assumptions within and between different blinking clusters. Starting from the assumption of independently blinking fluorophores (and thus blinking clusters), this is a standard convenience assumption in the literature [25, 33], albeit likely an approximation in samples with extreme local density. For the timepoints and the number of points in Y_x, $|Y_x| = G$, we allow general distribution and dependence structure. We need this level of generality as both are typically derived from the same, underlying source of stochasticity. Taking PALM as an example, the PA-FP in the sample switch between fluorescent and non-fluorescent states according to a continuous time absorbing Markov process, $S(t)$, and the observed times then correspond to the camera frames that overlap a fluorescent state visit. More broadly we can imagine the observed timepoints in Y_x arising as

$$D(S) = \{t_{y_1}, t_{y_2}, ..., t_{y_G}\}, \tag{A.3.5}$$

where D is a "discretization operator" (the camera, localization software, filtering,...), transforming S into the observed signal. In particular, the distribution and dependence structures of G and $\{t_{y_i}\}_{i=1}^G$ are both derived in some complex way from the same stochastic process, see Figure A.1 and Figure A.2.

Finally, for the locations in Y_x, $\{y_i\}_{i=1}^G$, recall that positions are estimated on the basis of fitting to a blurry point spread function (PSF) centered on x. This motivates why the locations in Y_x are modeled on the form

$$y_k = x + \epsilon_k, \tag{A.3.6}$$

where ϵ_k is a random variable on $\mathbb{R}^d$ reflecting our uncertainty about the true position x. The distributional shape and scale of ϵ_k depends on the PSF and on the number

of photons detected by the camera during the associated camera frame. As a practically necessary assumption, we modeled the collection $\{\epsilon_k\}_{k=1}^{G}$ as i.i.d., and further independent of the timepoints and G. These assumptions can all be motivated by the time-homogeneous Markov processes underlying photon statistics [33], which imply that the number of photons hitting different frames are approximately independent, and further independent of which frame number is currently being imaged.

A.3.2 A result on the mark correlation function

Let O be an IBCpp with motion-invariant X. We present here a key result on the mark correlation function, which we use to motivate the estimation procedures of Section A.4. The derivations of the results in this section and more can be found in Supplement A.

Let $f : \mathbb{R}_+^2 \mapsto \mathbb{R}_+$ be a symmetric query function of 2 arrival times, and assume P_ϵ has radially symmetric density function h_ϵ. Then, the pair- and mark correlation functions are functions only of the distance between two points, r, and for the product between them we have the result

$$\gamma_2^O(f)k_O^f(r)g_{\downarrow O}(r) = (\gamma_1(f) - \gamma_2(f))\left[\frac{\eta}{\lambda_{\downarrow O}} n_c(h_\epsilon * h_\epsilon)(r)\right] + \gamma_2(f)\left[g_{\downarrow O}(r) - 1\right] + \gamma_2^O(f) \tag{A.3.7}$$

where

$$n_c = \frac{\mathbb{E}\left[G^2\right]}{\mathbb{E}[G]} - 1, \tag{A.3.8}$$

$$\eta = \frac{\lambda_{\downarrow Z}}{\lambda_{\downarrow O}}, \tag{A.3.9}$$

$$\gamma_1(f) = \frac{\mathbb{E}\left[\sum_{(i,j)=1}^{G} \mathbb{1}(i \neq j) f(t_{y_i}, t_{y_j})\right]}{\mathbb{E}[G(G-1)]}, \tag{A.3.10}$$

$$\gamma_2(f) = \frac{\mathbb{E}\left[\sum_{i=1}^{G} \sum_{i=1}^{G'} f(t_{y_i}, t'_{y_j})\right]}{\mathbb{E}[G]^2}, \tag{A.3.11}$$

$$\gamma_2^O(f) = \int\int f(t_1, t_2) dM_O^{(1)}(t_1) dM_O^{(1)}(t_2), \tag{A.3.12}$$

and

$$(h_\epsilon * h_\epsilon)(r) = \int h_\epsilon(y_1 - x) h_\epsilon(y_2 - x) dx, \tag{A.3.13}$$

for $\|y_1 - y_2\| = r$. In the above, $(G, \{t_{y_i}\}_{i=1}^{G})$ should be thought of as the timepoints in a typical blinking cluster Y_x at arbitrary location x, and $(G', \{t'_{y_j}\}_{j=1}^{G'})$ is an independent copy of $(G, \{t_{y_i}\}_{i=1}^{G})$. Finally, $M_O^{(1)}$ is the 1-point mark distribution of O, which does not depend on the conditioning point, which is therefore omitted in the notation.

We unpack this result now in some detail, providing first some intuition on the involved quantities. We also cover some related moment expression that will be needed in the following. Starting with η, it is the expected fraction of points in O that arose from blinking clusters (as opposed to background noise), and in particular we

have the alternative expression

$$\eta = 1 - \frac{\lambda_{\downarrow E}}{\lambda_{\downarrow O}}, \tag{A.3.14}$$

as 1 minus the expected fraction of noise points. This is a simple consequence of the fact that the points in O are either from Z or E, so that

$$\lambda_{\downarrow O} = \lambda_{\downarrow Z} + \lambda_{\downarrow E}. \tag{A.3.15}$$

A useful related expression is

$$\lambda_{\downarrow Z} = \mathbb{E}[G]\,\lambda_{\downarrow X}, \tag{A.3.16}$$

which states the natural result that the number of points (per area) from blinking clusters can be written as the number of proteins (per area) times the number of repeats per protein.

Moving on to the second-order quantities, $\gamma_1(f)$ is essentially the mean value of $f(t_{y_1}, t_{y_2})$ when (t_{y_1}, t_{y_2}) are sampled randomly from the distinct pairs of timepoints in a typical blinking cluster. It should be clear that, depending on the choice of f, $\gamma_1(f)$ will contain information about the blinking dynamics of the fluorophores in the sample, a fact we will exploit for estimation. Similarly, $\gamma_2(f)$ is the mean value of $f(t_{y_1}, t'_{y_2})$ when the timepoints are sampled randomly from 2 different (and thus independent) blinking clusters. Lastly, $\gamma_2^O(f)$ is as before, but where each timepoint is an independently sampled timepoint among all timepoints in O, including those from noise points - it is also known as the normalization constant of the mark correlation function. Lastly, the spatial term $(h_\epsilon * h_\epsilon)(r)$ is simply the autoconvolution of the localization uncertainty density.

The expression in Equation (A.3.7) is important from the standpoint of semiparametric estimation due to the split of terms into products of spatial and temporal components. The temporal components (the γ's) and the spatial components ($g_{\downarrow O}$ and $(h_\epsilon * h_\epsilon)$) are in this sense separable, which hints at the possibility of extracting information about the temporal behavior of fluorophores, independently of their spatial coordinates. To make more explicit how this should be done, note the simple algebraic manipulation

$$(\gamma_1(f) - \gamma_2(f))n_c = \frac{\left(\gamma_2^O(f)k_O^f(r)g_{\downarrow O}(r) - \gamma_2(f)\left[g_{\downarrow O}(r) - 1\right] - \gamma_2^O(f)\right)\lambda_{\downarrow O}}{(h_\epsilon * h_\epsilon)(r)\eta}. \tag{A.3.17}$$

The significance of this identity is that the left hand side depends *only* on the process that generated blinking, whereas the right hand side can be estimated from O, without a need to model $_{\downarrow}X$. The idea is then to set these estimated quantities, for various f, in relation to their theoretical value under the parameters of a specified blinking model. We show how to do this in more detail in Section A.4.

A.3.3 An IBCpp model for PALM data

In order to use the IBCpp family in practice, we get more specific about the construction of the blinking clusters. The choices we make here are based on realistic models for PALM fluorophore photophysics, camera discretization effects, and localization errors, and lead to the PALM-IBCpp model. The PALM-IBCpp is most appropriate

for modeling of 2D data, as 3D PALM generally has unequal uncertainty in the xy versus z plane [31], and a radial noise profile is then no longer a valid assumption. As a workaround for 3D data, the z-coordinates can simply be discarded.

As in the general IBCpp formulation, we write the typical blinking cluster on the form

$$Y_x = \bigcup_{k=1}^{G} (x + \epsilon_k, t_{y_k}), \tag{A.3.18}$$

and we need to specify the distributions of ϵ_k, G, and t_{y_k}. Starting with ϵ_k, recall that a point source of light appears as a blurry spot on the camera, with shape described by the PSF. For PALM data we model this PSF using a symmetric Gaussian with random variance σ^2. We model σ as random since its magnitude depends on the number of photons detected and various other nuisance factors that will vary for each observation. Denoting by P_σ the distribution of σ, we thus write

$$(\epsilon_k|\sigma) \sim N(0, \sigma^2), \tag{A.3.19}$$

$$\sigma \sim P_\sigma, \tag{A.3.20}$$

where $(\cdot|\sigma)$ denotes the σ-conditional distribution, and $N(0, \sigma^2)$ is the centered Gaussian distribution with variance σ^2. Since localization software outputs an estimate $\hat{\sigma}$ for each observation, we do not need to parametrize P_σ. The use of Gaussian PSFs is standard practice, and generally provides a highly accurate approximation [40], but another model for the PSF can be used without serious complications, so long as it is radially symmetric on average (across the typical observation).

Moving on to G and the timepoints, we take as basis a well-established 4-state model for continuous time fluorophore behavior [11, 25, 6]. We imagine the PA-FP are independently following a Markov processes, with a single fluorescent state F, and 3 non-fluorescent states, see Figure A.1. A PA-FP always begins in the inactive state I, and eventually moves to the F state. From here, it can either go dark in D temporarily, or permanently photobleach in B.

We cannot observe the process in continuous time. In fact, if we write Δ for the length of 1 camera frame, the temporal resolution allows observations to occur only on the fixed grid $\Delta\mathbb{N}$. To describe the fluorescent signal that is ultimately observed on this grid, from a single PA-FP during the experiment, we consider a discretization operation under an idealized camera. Consider the indicator process

$$S(t) = \begin{cases} 1 & \text{if the PA-FP is in state } F \text{ at time } t \\ 0 & \text{otherwise.} \end{cases} \tag{A.3.21}$$

We imagine that any (measurable) amount of fluorescent signal hitting a given camera frame gives rise to an observation. Defining

$$\tilde{S}(k\Delta) = \mathbb{1}_{(0,\Delta]}\left(\int_{\Delta(k-1)}^{\Delta k} S(t)dt \right), \tag{A.3.22}$$

the observed timepoints are then $k\Delta$ whenever $\tilde{S}(k\Delta) = 1$. This corresponds to a camera with perfect sensitivity, which is of course an approximation to the truth. In reality there is a non-zero threshold on the amount of signal that must be observed

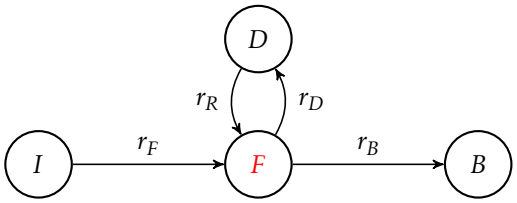

Figure A.1: The transition diagram for the continuous time, photophysical model of fluorophores. Transitions are Markovian, with rates indicated next to the transition arrows.

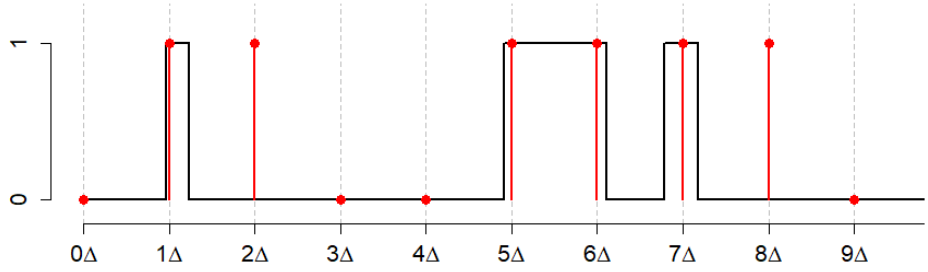

Figure A.2: Camera discretization transforms the continuous process $S(t)$ (in black) into the discrete process $\tilde{S}(k\Delta)$ (in red). The observed timepoints are the $k\Delta$ with $\tilde{S}(k\Delta) = 1$; in this example there are 6 such timepoints, observed on frames $\{1, 2, 5, 6, 7, 8\}$, and we thus have $G = 6$ and $\{y_{t_k}\}_{k=1}^{6} = (1\Delta, 2\Delta, 5\Delta, 6\Delta, 7\Delta, 8\Delta)$.

during a given integration period, but this threshold is generally very low in SMLM recordings [22], so we have ignored it here to avoid the complications that arise from modeling it.

From the above, we can write G and $\{t_{y_k}\}_{k=1}^{G}$ more formally as

$$G = \sum_{k=1}^{\infty} \tilde{S}(k\Delta), \tag{A.3.23}$$

$$t_{y_k} = \min\{s\Delta : s \in \mathbb{N} \text{ and } \sum_{i=1}^{s} \tilde{S}(i\Delta) = k\}, \ 1 \leq k \leq G. \tag{A.3.24}$$

In this way, the timepoints of a typical cluster correspond precisely to the discretized signal obtained from $S(t)$, see Figure A.2.

A.4 Estimation

We suggest now a stepwise estimation procedure, leading eventually to estimates of η and (r_F, r_D, r_R, r_B). As the implementation details are somewhat long-winded, we describe the methods here at the intuitive level, and refer to Supplement B and Algorithm 1 for more details. For clarity of exposition, we motivate our approach on the assumption that $_{\downarrow}X$ be motion-invariant, but we stress that this is not a necessary assumption in practice, as Algorithm 1 will produce meaningful estimates also for general $_{\downarrow}X$, cf. Supplement D. Further, since the PALM-IBCpp is most appropriate for 2D data, as previously noted, we assume the spatial dimension is $d = 2$ in the following. An efficient implementation of Algorithm 1, and various other helpful tools, are available, see Code availability.

A.4.1 Data format and requirements

In the following, we assume that we have data $\{(o_k, t_{o_k})\}_{i=1}^N$ from a PALM-IBCpp observed with N points in the space-time window $W \times [0, b]$, where $W \subset \mathbb{R}^2$ and b is the length of the PALM recording in seconds. Additionally, we require access to localization uncertainties associated with each position, and we denote these by $\{\hat{\sigma}_k\}_{k=1}^N$. Note that it is assumed the timepoints t_{o_k} are recorded in seconds. Often it is the case that PALM data is recorded in terms of frame numbers, and it is then necessary to first transform the times by multiplying the frame numbers by the camera integration length, Δ, which can be obtained from the framerate by

$$\Delta = \frac{1}{\text{framerate}}, \tag{A.4.1}$$

and is also a required component in its own right.

If the fitting procedures should account for background noise, it is also necessary to have access to an observation of pure noise, which will allow us to quantify the fraction of points arising as noise. Thus, we assume that we have N_e observations $\{e_k, t_{e_k}\}_{k=1}^{N_E}$ of E in a separate space-time window $W_E \times [0, b]$. Access to E in this way is typically possible without a need to perform additional experiments, as standard PALM recordings generally extend to regions outside the cell being imaged, see Figure A.3 and Figure A.4.

A.4.2 Choice of query functions

The foundation for estimation of kinetic rates is the identity in Equation (A.3.17), which allow us to extract a purely temporal information from the observed space-time data, principally via $\gamma_1(f)$ and n_c. The type and quality of this information depends crucially on our choice for the query function f. In the following, we pick the set of functions

$$f_u(t_1, t_2) = \mathbb{1}(|t_1 - t_2| \leq u), \quad u \in T, \tag{A.4.2}$$

$$T = \{i\Delta\}_{i=1}^{\lfloor \frac{b}{\Delta} \rfloor}. \tag{A.4.3}$$

This choice exhausts the information present in functions acting on times only through their difference, while eliminating absolute time information. To see why this can be desirable, imagine a typical blinking cluster Y_x. The timepoints in Y_x can be written approximately (up to rounding-induced errors) on the form

$$t_{o_k} \approx W_F + w_k, \tag{A.4.4}$$

Algorithm 1: PALM-IBCpp model fit, part 1

Input : Space-time observations $\{o_k, t_{o_k}\}_{k=1}^N$ observed in window $W \times [0, b]$, where b is the length of the PALM recording in seconds.

Input : Localization uncertainties $\{\hat{\sigma}_k\}_{k=1}^N$.

Input : Camera integration length, $\Delta = \frac{1}{\text{framerate}}$.

Input : Quality parameters n_r and n_s (default values of 500 and 10000 are used everywhere in this work, respectively).

Input : (optional) The noise process $E = \{e_k, t_{e_k}\}_{k=1}^{N_E}$ observed separately in window $W_E \times [0, b]$.

Output: Estimated fraction of non-noise points $\hat{\eta}$ and kinetic rates $(\hat{r}_F, \hat{r}_D, \hat{r}_R, \hat{r}_B)$.

Initialization

(1) If $\{t_{o_k}\}_{k=1}^N$ are stored as frame numbers, update each timepoint as

$$t_{o_k} \leftarrow t_{o_k} \Delta.$$

(2) Define the spatial range r_{max} and grid R, by

$$r_{max} = \frac{1}{N} \sum_{k=1}^{N} \hat{\sigma}_k, \qquad R = \{\frac{r_{max}}{n_r} i\}_{i=1}^{n_r}.$$

(3) Define the temporal grid T and query functions f_u for $u \in T$ by

$$T = \{\Delta i\}_{i=1}^{\lfloor \frac{b}{\Delta} \rfloor}, \qquad f_u(t_1, t_2) = \mathbb{1}(|t_1 - t_2| \leq u).$$

end

Estimation of η

Set $\hat{\lambda}_{\downarrow O} = \frac{N}{|W|}$. If E was observed in a separate window, set $\hat{\lambda}_{\downarrow E} = \frac{N_E}{|W_E|}$, and otherwise set $\hat{\lambda}_{\downarrow E} = 0$. Return the estimator

$$\hat{\eta} = 1 - \frac{\hat{\lambda}_{\downarrow E}}{\hat{\lambda}_{\downarrow O}}.$$

end

where $W_F \sim Exp(r_F)$ is the time spent in the inactive I state before first activation, and w_k is the waiting time separating the k'th appearance from the temporal origin, which depends only on the remaining rates (r_D, r_R, r_B). When extracting information from a query function through $\gamma_1(f)$, we then obtain

$$\gamma_1(f) \approx \frac{\mathbb{E}\left[\sum_{(i,j)=1}^{G} \mathbb{1}(i \neq j) f(W_F + w_i, W_F + w_j)\right]}{\mathbb{E}[G(G-1)]}. \tag{A.4.5}$$

Since r_F is typically orders of magnitudes smaller than the remaining rates, W_F will tend to dominate and obscure the information on the remaining parameters. On the other hand, for f_u we have

$$\gamma_1(f_u) \approx \frac{\mathbb{E}\left[\sum_{(i,j)=1}^{G} \mathbb{1}(i \neq j) \mathbb{1}(|w_i - w_j| \leq u)\right]}{\mathbb{E}[G(G-1)]}, \tag{A.4.6}$$

Algorithm 1: PALM-IBCpp model fit, part 2

Estimation of kinetic rates

(1) Let $\{\hat{\sigma}_{1,k}\}_{k=1}^{n_s}$ and $\{\hat{\sigma}_{2,k}\}_{k=1}^{n_s}$ be independent samples of size n_s with replacement from $\{\hat{\sigma}_k\}_{k=1}^{N}$. Estimate the blinking cluster autoconvolution via

$$\widehat{(h_\epsilon * h_\epsilon)}(r) = \frac{1}{n_s}\sum_{k=1}^{n_s} \frac{e^{-\frac{r^2}{2(\hat{\sigma}_{1,k}^2+\hat{\sigma}_{2,k}^2)}}}{2\pi(\hat{\sigma}_{1,k}^2+\hat{\sigma}_{2,k}^2)}, \quad r \in R.$$

(2) Let $\{t_{o_{1,k}}\}_{k=1}^{n_s}$ and $\{t_{o_{2,k}}\}_{k=1}^{n_s}$ be independent samples of size n_s with replacement from $\{t_{o_k}\}_{k=1}^{N}$. Estimate $\gamma_2^O(f_u)$ via

$$\hat{\gamma}_2^O(f_u) = \frac{1}{n_s}\sum_{k=1}^{n_s} \mathbb{1}(|t_{1,k} - t_{2,k}| \le u), \quad u \in T.$$

(3) Define the distribution function

$$\hat{M}_Z^{(1)}(u) = \frac{N^{-1}\sum_{k=1}^{N} \mathbb{1}(t_{o_k} \le u) - (1-\hat{\eta})\frac{u}{b}}{\hat{\eta}}.$$

Sample i.i.d. collections of variates $\{\tilde{t}_{1,k}\}_{k=1}^{n_s}$ and $\{\tilde{t}_{2,k}\}_{k=1}^{n_s}$ with distribution $\hat{M}_Z^{(1)}$, and use the estimator

$$\hat{\gamma}_2(f_u) = \frac{1}{n_s}\sum_{k=1}^{n_s} \mathbb{1}(|\tilde{t}_{1,k} - \tilde{t}_{2,k}| \le u), \quad u \in T.$$

(4) Using (any) standard estimators for the mark- and pair correlation functions, $\hat{k}_O^f$ and $\hat{g}_{\downarrow O}$, set

$$\hat{\zeta}_u = \frac{\hat{\lambda}_{\downarrow O}}{\hat{\eta}} \frac{\sum_{r\in R}\left[\hat{\gamma}_2^O(f_u)\hat{k}_O^{f_u}(r)\hat{g}_{\downarrow O}(r) - \hat{\gamma}_2(f_u)(\hat{g}_{\downarrow O}(r)-1) - \hat{\gamma}_2^O(f_u)\right]\left[\widehat{(h_\epsilon * h_\epsilon)}(r)\right]}{\sum_{r\in R}\left[\widehat{(h_\epsilon * h_\epsilon)}(r)\right]^2},$$

for each $u \in T$.

(5) Using the approximate expressions for $\gamma_1(f_u)$ and n_c in Supplement B, solve the weighted least squares problem

$$\min_{\hat{r}_D,\hat{r}_R,\hat{r}_B} \sum_{u\in T}\sum_{r\in R}\left(\frac{\hat{\zeta}_u}{\gamma_2(f_u)}\right)^2 \left(\hat{\zeta}_u - (\gamma_1(f_u) - \hat{\gamma}_2(f_u))n_c\right)^2,$$

to obtain estimators $(\hat{r}_D, \hat{r}_R, \hat{r}_B)$.

(6) Obtain an estimator of r_F by setting

$$\hat{r}_F = \left(\frac{\frac{1}{N}\sum_{k=1}^{N} t_{o_k} - (1-\hat{\eta})\frac{b}{2}}{\hat{\eta}} - \hat{A}_2 - \hat{B}_2\right)^{-1}.$$

where $\hat{A}_2$ and $\hat{B}_2$ are defined in Supplement B.

(7) Obtained a censoring-corrected estimate of r_F by numerically solving

$$\frac{e^{\hat{r}_F^c b} - \hat{r}_F^c b - 1}{\hat{r}_F^c(e^{\hat{r}_F^c b} - 1)} - \frac{1}{\hat{r}_F} = 0,$$

in $\hat{r}_F^c$ over the interval $(0, \hat{r}_F]$.

(8) Return the rate estimates $(\hat{r}_F^c, \hat{r}_D, \hat{r}_R, \hat{r}_B)$.

end

eliminating the influence of r_F entirely. This suggests a two step approach where r_F is treated separately from (r_D, r_R, r_B).

A.4.3 Estimating parameters

The estimation procedures consist roughly of two phases: estimation of η, and estimation of the kinetic rates. The idea is that once $\hat{\eta}$ is known, we can obtain *location invariant* statistics, that allow estimation of the kinetic rates. The second phase is further divided into two steps, as r_F is treated separately from the remaining rates.

Estimating η is easy when E is observed separately, since

$$\eta = 1 - \frac{\lambda_{\downarrow E}}{\lambda_{\downarrow O}}, \tag{A.4.7}$$

so the problem reduces to intensity estimation, which is routinely performed by setting the observed number of points in relation to the area of the observation window. Next, to estimate the kinetic rates, the primary ingredients are the quantities

$$\zeta_u = (\gamma_1(f_u) - \gamma_2(f_u))\, n_c, \quad u \in T, \tag{A.4.8}$$

which can be extracted from the data using the identity in Equation (A.3.17), which states that

$$\zeta_u = \frac{\left(\gamma_2^O(f) k_O^f(r) g_{\downarrow O}(r) - \gamma_2(f)\left[g_{\downarrow O}(r) - 1\right] - \gamma_2^O(f)\right)\lambda_{\downarrow O}}{(h_\epsilon * h_\epsilon)(r)\eta}, \quad u \in T, \tag{A.4.9}$$

which is estimable on the basis of the observed data and $\hat{\eta}$. From the collection $\{\hat{\zeta}_u\}_{u\in T}$ we set up a weighted minimization problem

$$\min_{\hat{r}_D, \hat{r}_R, \hat{r}_B} \sum_{u\in T} \sum_{r\in R} \left(\frac{\hat{\zeta}_u}{\hat{\gamma}_2(f_u)}\right)^2 \left(\hat{\zeta}_u - (\gamma_1(f_u) - \hat{\gamma}_2(f_u))n_c\right)^2, \tag{A.4.10}$$

over the involved rates, where R is a set of spatial distances that must be specified, and the weights $\frac{\hat{\zeta}_u}{\hat{\gamma}_2(f_u)}$ are chosen to put more weight on temporal distances that are most informative. The rates control the values of $\gamma_1(f_u)$ and n_c, and expressions for these are available in Supplement B. As the minimization leads only to 3 of the 4 rates, r_F is obtained separately via

$$\hat{r}_F = \left(\frac{\frac{1}{N}\sum_{i=1}^N t_{o_i} - (1-\hat{\eta})\frac{b}{2}}{\hat{\eta}} - \hat{A}_2 - \hat{B}_2\right)^{-1}, \tag{A.4.11}$$

where $\hat{A}_2$ and $\hat{B}_2$ are statistics computed on the basis of $(\hat{r}_D, \hat{r}_R, \hat{r}_B)$. Since we only observe a finite recording of lenght b, $\hat{r}_F$ will be subject to a censoring bias. A corrected estimate is found by solving

$$\frac{e^{r_F^c b} - r_F^c b - 1}{r_F^c (e^{r_F^c b} - 1)} - \hat{r}_F^{-1} = 0, \tag{A.4.12}$$

in r_F^c.

A.5 Validation of methods on a nuclear pore complex reference cell line

The nuclear pore complex (NPC) is quickly becoming a reference standard for quantitative SMLM imaging. In a recently developed NPC cell line [36], the nucleoporin

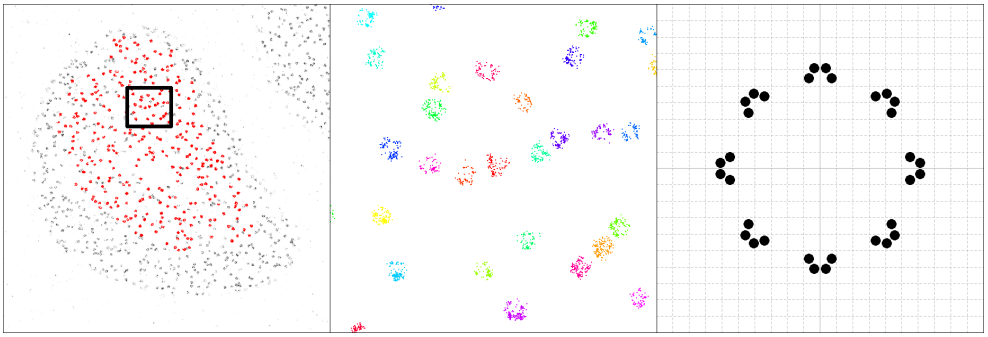

Figure A.3: Nuclear pore complexes in Nup96 cell lines. Left: an example dataset of a cell expressing Nup96-mMaple. The red complexes are those that were confidently segmented by SMAP (see main text), and were used for further analysis. The rectangular region is picked only for visualization purposes, and can be seen magnified in the center plot. Center: magnified region of segmented complexes. The color indicates which points are determined as belonging to the same complex. Right: Top view schematic of an idealized Nup96 complex. A grid of separation 10nm is overlaid for scale.

Nup96 is endogenously tagged with fluorescent labels. Each complex forms a ring of approximately 55nm in radius, comprising 32 Nup96 arranged into 8 equally spaced corners of 4 Nup96 each, see Figure A.3. Due to this well-characterized organization of proteins, these cells offer the rare opportunity of checking results against a known ground truth on a real biological sample.

We analyze the publicly available datasets [35] comprising PALM recordings of Nup96 tagged with mMaple, using a buffer of 50mM Tris in D_2O, recorded with a camera integration length of $\Delta = \frac{1}{10}$. In total, this amounts to localized data from 16 cells, preprocessed according to the procedures in [36]; briefly, using the provided open-source software SMAP [23], localizations were corrected for drift, and emitters with large uncertainty or poor fit likelihood were filtered out. This data presents a challenging setting for the PALM-IBCpp analysis, as the filtering steps are a clear breach of model assumptions, and the low framerate of 10hz challenges the approximations used in fitting, which are only exact in the limit of large framerates.

For each cell, we used SMAP with the established procedures to first segment out high-quality NPCs, and then estimated the effective labeling efficacy (ELE), which describes the fraction of Nup96 that are sufficiently bright to be detected in the SMLM recording. For each cell, we then computed the "target" number of reappearances per Nup96 ($\mathbb{E}_S[G]$, "S" indicating SMAP) according to the formula

$$\mathbb{E}_S[G] = \frac{N_{loc}}{N_{NPC} \cdot ELE \cdot 32}, \tag{A.5.1}$$

where N_{NPC} is the number of segmented NPC, and N_{loc} is the total number of localizations observed across all segmented complexes. In addition, the target number of F state visits ($\mathbb{E}_S[N_b]$) is computed as

$$\mathbb{E}_S[N_b] = \frac{N_{loc,grouped}}{N_{NPC} \cdot ELE \cdot 32}, \tag{A.5.2}$$

where $N_{loc,grouped}$ is the number of localizations from the segmented complexes, after grouping together localizations close in space (35nm) and time (1 frame), again according to the procedures of [36]. As the number of F state visits has a Geometric

distribution (starting at 1), we have $N_b \sim Geom_1(p)$, where $p = \frac{r_B}{r_B+r_D}$ is the bleaching probability. An SMAP estimate of p is thus naturally found via

$$p_S = \frac{1}{\mathbb{E}_S[N_b]}. \tag{A.5.3}$$

Finally, we fit the IBCpp model on the segmented NPCs. To get the most fair comparison with the SMAP targets, we set $\hat{\eta} = 1$ when fitting. This is because SMAP does not account for background localizations, and thus assumes all observations are generated by PA-FP. After fitting, we computed the estimated values of the above targets. We also include the derived statistic

$$N_{copy} = \frac{N_{loc}}{N_{NPC}\mathbb{E}[G]ELE}, \tag{A.5.4}$$

where $\mathbb{E}[G]$ is the estimated mean of G, on the basis of the PALM-IBCpp fit. N_{copy} has a ground truth target value of 32, the copy number of Nup96 per complex.

While the true blinking rates of the data remain unknown, and have no direct SMAP analogue, we can nevertheless compare our model predictions on the derived blinking statistics against the targets, and in this way validate important aspects of our modeling and estimation framework. In Table A.1 the means and standard deviations from fitting to the 16 datasets can be seen. Interestingly, in spite of the model violations incurred by data filtering, we obtained encouraging results. The most intuitive reference quantity, N_{copy}, is estimated at 32.3 ± 1.82, in close correspondence with the ground truth value of 32. The accurate recovery is due to the tight control on $\mathbb{E}[G]$, the total number of appearances per $Nup96$, estimated at 7.40 ± 0.72 by our model, versus 7.46 for the SMAP analysis. One slight deviation from the targets is the number of F state visits, estimated at 2.32 ± 0.08 versus 2.93 for SMAP. A possible explanation for this difference lies in how SMAP estimates it; since the grouping procedure only looks for repeat localizations within a spatial radius of 35nm, it should be expected that some F state visits are broken up into multiple subsegments, potentially biasing results in favor of larger values. This would also explain the slight disagreement for p.

As mentioned, we unfortunately do not have an SMAP reference for the blinking rates. Nevertheless, as both the total number of reapperances and number of blinking cycles are well-estimated, it seems plausible that the estimated blinking dynamics as a whole can be trusted. Looking at the rates, we see that there is surprisingly low variability between datasets, indicating that the replications were performed with careful attention to the experimental conditions. In addition, we notice quite a long-lived dark state, lasting on average 3 seconds. Using the mean rates across all 16 datasets, we find that the Nup96-mMaple had a mean bleaching time of 4.61 seconds, and 99% of Nup96 bleached within 31 seconds.

Results from each individual dataset, including the ELE, number of NPC, and dataset ids, are also available, see Table A.2. Although not used in this analysis, we also included estimates of η for completeness.

A.6 Blinking corrected cluster analysis of LAT-mEos3.2

Cluster analysis is perhaps the most common goal of SMLM experiments, and a great deal of effort has been put towards that end. A shared complication among all such

Table A.1: Estimates and standard deviations of blinking rates and derived statistics on the basis of our model fit to 16 datasets of Nup96 NPC. The target values are based on the SMAP analysis, or are known in the case of N_{copy} (see main text).

	Estimate	*Target*	*Sd*
$r_F \cdot 10^3$	0.73	-	0.29
r_B	2.00	-	0.28
r_D	2.64	-	0.37
r_R	0.32	-	0.06
N_{copy}	32.30	32.00	1.82
$\mathbb{E}[G]$	7.40	7.46	0.72
$\mathbb{E}[N_b]$	2.32	2.93	0.08
p	0.43	0.34	0.01

Table A.2: Results from 16 datasets of Nup96 nuclear pore complexes. The data ids allow identification of the exact dataset analyzed, as stored on the BioImage Archive [35]. The estimated rates can be seen in columns 2 through 5. $\mathbb{E}[G]$ and $\mathbb{E}[N_b]$ are the estimated total number of reappearances per Nup96 and number of F state visits on the basis of the PALM-IBCpp model fit, and $\mathbb{E}_S[G]$ and $\mathbb{E}_S[N_b]$ are the associated targets, on the basis of the SMAP analysis. ELE is the estimated fraction of Nup96 that are detectable in the dataset, as determined by SMAP. N_{copy} is the PALM-IBCpp estimated number of Nup96 per NUP complex, after account for the ELE, which has a target value of 32. N_{NPC} is the number of segmented complexes. Finally, η is the estimated fraction of non-noise points.

Data id	$r_F \cdot 10^3$	r_B	r_D	r_R	$\mathbb{E}[G]$	$\mathbb{E}_S[G]$	$\mathbb{E}[N_b]$	$\mathbb{E}_S[N_b]$	N_{copy}	ELE	N_{NPC}	η
181123_6	0.90	2.28	2.91	0.30	6.64	6.43	2.28	2.64	31.0	0.45	313	0.98
181123_7	0.23	1.91	2.87	0.34	7.72	6.91	2.51	2.85	28.6	0.60	239	1.00
181123_8	0.67	2.00	2.51	0.30	7.25	6.69	2.26	2.75	29.5	0.57	179	0.99
190110_1	0.37	1.71	2.10	0.30	8.07	8.20	2.23	3.06	32.5	0.65	184	0.97
190110_2	0.40	1.81	2.33	0.53	7.76	8.20	2.28	3.05	33.8	0.60	420	0.96
190111_10	0.75	1.81	2.54	0.32	7.89	7.78	2.40	3.06	31.6	0.65	713	0.97
190111_11	0.63	1.69	2.37	0.33	8.30	8.15	2.40	3.16	31.4	0.63	846	0.95
190111_9	0.48	1.71	2.43	0.33	8.25	8.26	2.42	3.22	32.0	0.64	1080	0.97
190118_12	0.59	2.18	3.08	0.32	6.97	6.84	2.41	2.85	31.4	0.60	1040	0.99
190118_13	0.94	2.23	2.81	0.30	6.72	6.66	2.26	2.77	31.7	0.61	567	0.98
190118_14	0.63	2.33	3.03	0.30	6.56	7.21	2.30	2.89	35.1	0.57	648	0.98
190123_3	1.37	2.32	2.96	0.30	6.56	7.09	2.27	2.72	34.6	0.55	207	0.98
190123_4	1.25	2.36	3.03	0.30	6.49	7.02	2.28	2.88	34.6	0.58	303	0.96
190123_5	0.71	2.37	3.17	0.31	6.54	7.14	2.34	2.86	34.9	0.60	578	0.96
190502_15	0.86	1.62	2.02	0.29	8.39	8.55	2.24	3.12	32.6	0.64	396	0.99
190502_16	0.89	1.67	2.10	0.30	8.22	8.21	2.26	3.04	31.9	0.62	440	0.98

analyses is the need to deal with artificial clustering caused by blinking artifacts, and most methods require the data to be first pre-proccessed to correct this [16]. This sort of pre-processing often relies on grouping of localizations on the basis of thresholds determined heuristically or by calibration data [3, 2], and can have quite variable performance [17]. Other methods can deal with blinking by explicitly modeling it alongside the proteins [29], but this limits the analyses that can be done, and requires parametric modeling of the proteins.

To overcome the challenges of quantitative cluster analysis, we suggest estimating first the blinking dynamics directly from the dataset using the PALM-IBCpp model, and subsequently correcting the desired clustering analysis for blinking biases. To exemplify this general methodology, we devise a blinking corrected test for CSR,

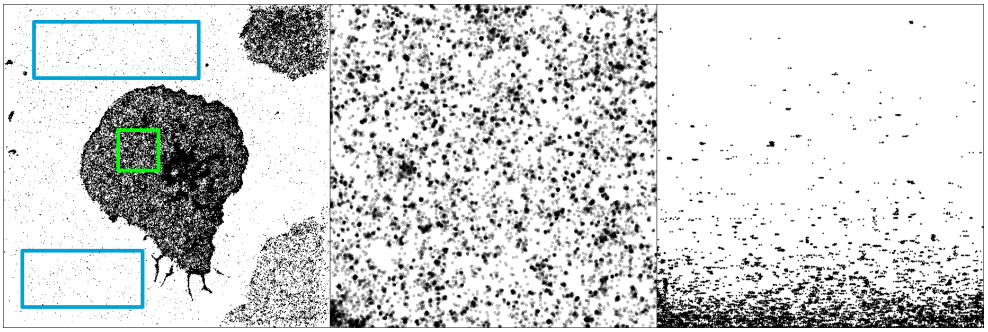

Figure A.4: Left: the full dataset with green region of interest used for fitting the IBCpp model, and blue noise regions used for estimating η. Center: magnified xy scatter plot of the ROI. Right: timepoints are plotted against the x-axis for the region of interest, demonstrating the space-time blinking dynamics.

and demonstrate it on a Jurkat T cell expressing LAT-mEos3.2 PA-FP. The dataset was recorded using PALM at a framerate of $\Delta^{-1} = 25hz$, and was then resolved and corrected for drift using ThunderSTORM [21].

We base our approach on the $L(r) - r$ function, a commonly used transformation of Ripley's K-function [24], which has better variance properties, and is easier to interpret. The function measures spatial clustering, with values of $L(r) - r > 0$ indicating clustering, $L(r) - r = 0$ for CSR-like behavior, and $L(r) - r < 0$ indicates repulsive behavior. To test whether a given dataset follows a prescribed null model, such as CSR, one can compare the observed $L(r) - r$ function to realizations from the null model, as obtained via simulations. This approach can be made rigorous using the class of global envelope tests [19], which produce an envelope that is global in the sense that, if the observed statistic breaches the envelope at any point, it corresponds to a significant test.

At a first glance, we cannot apply this idea directly to our data, as the null model we are testing is not just CSR, but rather CSR observed under blinking and background noise. This means that we do in fact expect to observe large values of $L(r) - r$, even for CSR proteins, and the question is rather how large this function must be to indicate significant protein clustering. Fortunately, as we are able to estimate the blinking rates, we can perform simulations from a model that approximates the null, and get a better handle on the true clustering behavior of the proteins. Of course, as this method is based on parametric bootstrapping, the significance level of the test is only guaranteed to be at the specified level if the rates are estimated perfectly, and some care is advised when interpreting results. To ensure the level of the test is approximately as specified, we suggest using simulation - we demonstrate this below.

For the analysis we first subset out a region of interest (ROI) of manageable size. In addition to the ROI we also subset out 2 large regions from the coverslip outside the cell, which were used for estimation of η, see Figure A.4. The ROI had 21742 points $\{(o_k, t_{o_k})\}_{k=1}^{21742}$ with associated localization uncertainties $\{\hat{\sigma}_k\}_{k=1}^{21742}$. Similarly, the noise regions had 1063 points in total, and the fraction of non-noise points (per area) was estimated at $\hat{\eta} = 0.995$. We fit the PALM-IBCpp model to this ROI, and we are thus in a position to simulate from the CSR (with blinking) null model, using the estimated blinking dynamics. To do this, the number of proteins to simulate was first

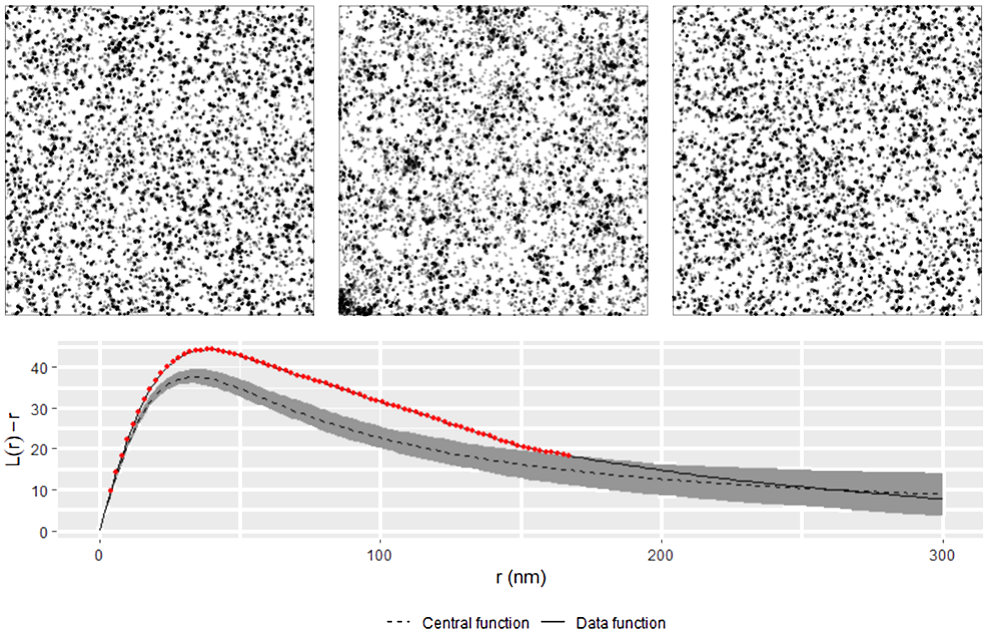

Figure A.5: Blinking corrected CSR test. **Top row**. Center: the observed data. Left and right: representative simulations of blinking CSR proteins with background noise. The blinking rates, number of proteins, and noise parameters used in simulations were obtained from the PALM-IBCpp fit to the observed data (see main text). **Bottom row**. Blinking corrected, 2-sided CSR global envelope test for the observed data, on the basis of the $L(r) - r$ function. The observed $L(r) - r$ function (solid line) was compared to the $L(r) - r$ functions of 500 simulations of blinking CSR proteins with noise, and a global envelope was constructed (shaded gray). The breach of the observed curve above the envelope indicates significant protein clustering in the ROI which cannot be explained by blinking alone ($p = 0.004$).

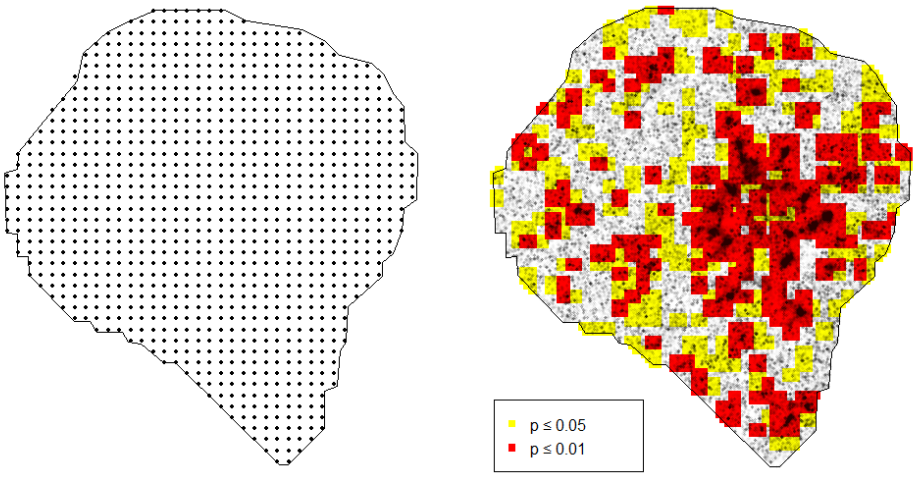

Figure A.6: Blinking corrected CSR testing on the entire cell. Left: the interior of the cell was segmented out, and an evenly spaced grid with separation 500nm was overlaid. Right: around each gridpoint, a centered 1000×1000nm observation window was used to subset out a local portion of the data, and a blinking corrected CSR test was performed for that region (see main text and Figure A.5). For visualization purposes we extrapolated p-values to the entire cell using the p-value associated with the nearest-neighbor point in the grid.

determined on the basis of Equation (A.3.16), which states that

$$\lambda_{\downarrow X} = \frac{\lambda_{\downarrow Z}}{\mathbb{E}[G]} = \frac{\eta \lambda_{\downarrow O}}{\mathbb{E}[G]}, \tag{A.6.1}$$

so that by plugging in our estimates for η, $\lambda_{\downarrow O}$, and $\mathbb{E}[G]$, and multiplying by the window area, we get the number of proteins at

$$N_{protein} \approx \frac{0.995 \cdot 21742}{8.16} \approx 2651. \tag{A.6.2}$$

Each localization in the blinking clusters was then simulated by adding Gaussian noise around the position of a protein, with a standard deviation sampled from $\{\hat{\sigma_k}\}_{k=1}^{21742}$, and the timepoints were simulated according to the discretized 4 state model. Finally we added 109 Poisson background noise points, as indicated by $\hat{\eta}$. Examples of simulations can be seen in the top row of Figure A.5 on the left and right.

Using this simulation scheme, we tested for CSR proteins on the basis of the $L(r)-r$ function. We computed $L(r)-r$ for the observed ROI, and obtained 500 realizations of it from the CSR null model via simulation. We then performed a global envelope test, see Figure A.5. The envelopes indicate the sort of clustering that we would expect to see from blinking clusters. The observed $L(r) - r$ breaches above the envelope, indicating that there is significant clustering of proteins ($p = 0.004$). The observed ROI has spots of clustering that, upon visual inspection and comparison with the null model simulations, are clearly too large to be blinking alone. The results of fitting to the ROI can be seen in Table A.3, where also the results of refitting to 100 simulations of the CSR null model are included. The refits indicate approximate unbiasedness, and low uncertainty of rate estimates. To validate that our test is approximately at the 5% level, we performed the CSR test for each of the 100 simulations, resulting in 3 rejections, in close correspondence with expectations.

To complete this analysis, we next performed the CSR test on the entire cell by means of a rolling window, see Figure A.6. This revealed regions of strongly significant clustering, but also regions indistinguishable from CSR. In fact roughly half the cell presented as clustered, with 47% of the cell clustered at the 5% percent level, and 26% at the 1% level.

A.7 Simulation study

We evaluate the performance of our method under different protein distributions and blinking models. We will also consider what happens when the blinking model is misspecified. We consider 3 different cases of protein distributions: CSR, spherical clustering, and fibrous structures, see Figure A.7. We fix the number of proteins at 500 for all simulations, with localization uncertainties drawn i.i.d. from the Gamma(6.5, 0.375) distribution (shape and rate parameterization), which is the maximum likelihood fit to the observed uncertainties in the LAT data of Section A.6, and we consider $\eta = 1$ known.

For the kinetic rates, we consider short and long lived PA-FPs. Additionally, in a misspecified case, we use a model with 3 distinct dark states, each selected with the same probability, but with very different holding time distributions. For the values of

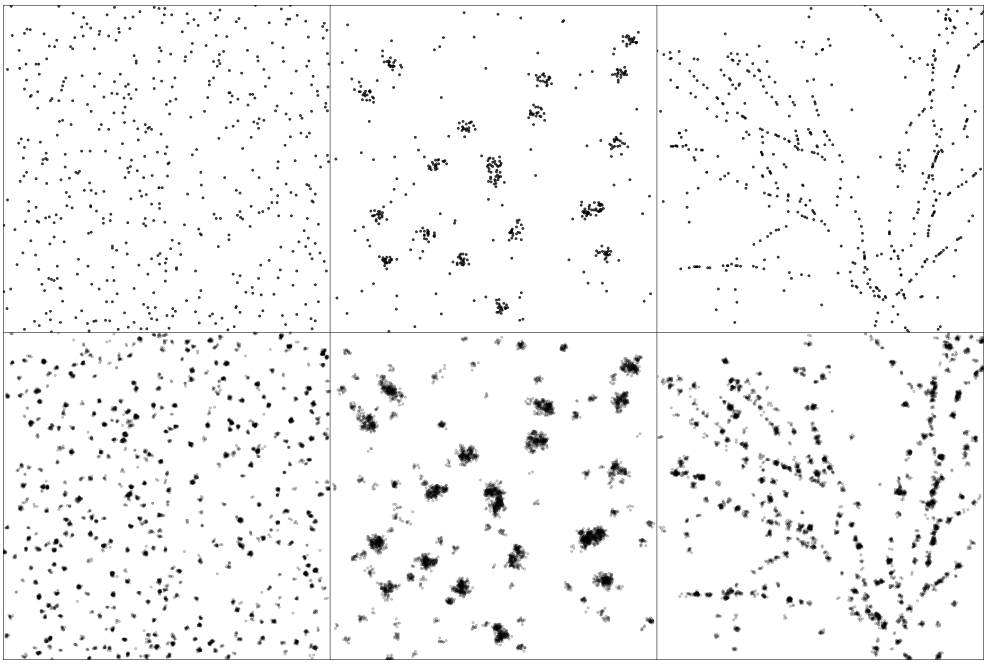

Figure A.7: Typical simulations from each of the 3 protein configurations (CSR, clusters, fibers) in the columns, before and after adding blinking clusters in the top and bottom rows, respectively. The CSR data is simulated as 500 i.i.d. uniform points in the ROI. The clusters data consists of 100 CSR points and further 20 uniformly located Gaussian clusters with standard deviation 50, each having 20 points. Finally, for the fiber data, 450 points are sampled uniformly along the edges of a fixed fiber structure, and 50 CSR points are added to the background.

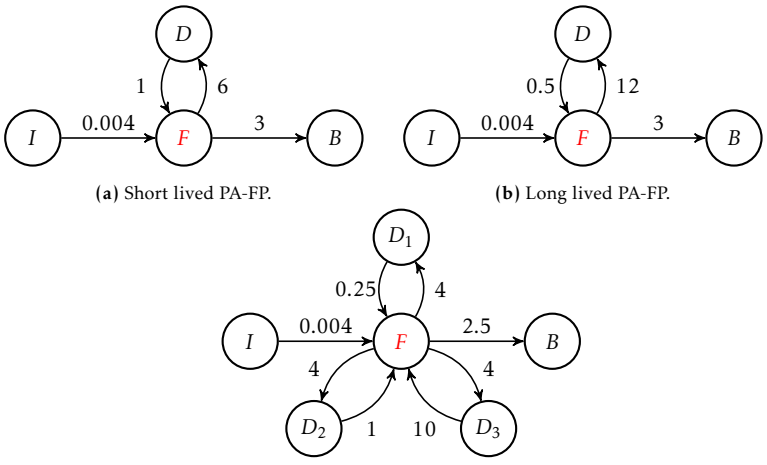

(a) Short lived PA-FP.

(b) Long lived PA-FP.

(c) 3 dark-state PA-FP.

Figure A.8: The three models of PA-FP photophysics considered in simulations.

Table A.3: Estimates (Est) obtained from the fit to the observed data. Included is average (Avg) and standard deviation (Sd) of estimates obtained from fitting to 100 simulations from the CSR null model. Included derived quantities are: the mean number of appearances per protein, $\mathbb{E}[G]$, the bleaching probability, $p = \frac{r_B}{r_B+r_D}$, and the $(0.25, 0.50, 0.75, 0.99)$-quantiles $(q_{0.25}, q_{0.50}, q_{0.75}, q_{0.99})$ of the total PA-FP lifetime distribution (time in seconds from activation to bleaching). For example, 75% of PA-FP bleach within $q_{0.75}$ seconds.

	Est	Avg	Sd
$r_F \cdot 10^3$	5.16	5.17	0.13
r_B	4.92	5.07	0.13
r_D	10.50	11.40	0.55
r_R	1.11	1.15	0.04
$\mathbb{E}[G]$	8.16	8.13	0.17
p	0.32	0.31	0.01
$q_{0.25}$	0.10	0.10	0.00
$q_{0.50}$	1.04	1.08	0.04
$q_{0.75}$	3.10	3.13	0.05
$q_{0.99}$	15.70	12.70	0.15

the kinetic rates in the 3 PA-FP models, see Figure A.8. We simulated 100 realizations from each combination of spatial organization and blinking behavior, and discretized signals according to a framerate of 25hz.

The results of the simulation study can be seen in Table A.4. For the short and long lived PA-FPs, we see that there is close correspondence between the true parameter values and their estimates, especially for the smaller rates and all derived blinking statistics. The mean number of reappearances is well estimated, as is the bleaching probability p, and the total lifetime quantiles. Some bias appears to exist for the dark-state entrance rate, r_D, which also has the highest uncertainty of the rates. This is likely due to bias in the utilized approximations for low framerate to rate ratios. Importantly, for the misspecified 3 dark-states model, the number of reappearances and the lifetime quantiles are again well estimated. Unsurprisingly, both r_B and p are biased in this case, as the model attempts to fit to an average blinking cycle, and cannot exactly capture the nuances of having 3 different dark states. Overall, the effect of the protein distribution is small compared to the effect of different PA-FP models, with a slight increase in variance for more clustered conditions.

To put this analysis into a broader perspective, we compared with results obtained from the PC-PALM (pair correlation PALM) method of [29]. This method is not capable of extracting the kinetic rates, but it can estimate $\mathbb{E}[G]$ for sufficiently simple models on the distribution of G. The PC-PALM method requires modeling of the proteins via an assumed form for the protein pair correlation function $g_{\downarrow X}(r)$. Following the authors, we set

$$g_{\downarrow X}(r) = Ae^{-\frac{r}{B}} + 1, \tag{A.7.1}$$

where A and B are parameters that need to be estimated. The PC-PALM method fits a model to the observed pair correlation function, from which n_c is readily estimated. In order to then estimate $\mathbb{E}[G]$, the authors use the approximation

$$\mathbb{E}[G] \approx n_c, \tag{A.7.2}$$

Table A.4: Results of fitting to 100 simulations from each combination of protein distribution (CSR, cluster, fibers) and PA-FP model (short lived, long lived, 3 dark-states). The average (Avg) and standard deviation (Sd) of estimates is included.

CSR

	Short lived			Long lived			3 dark-states		
	Truth	Avg	Sd	Truth	Avg	Sd	Truth	Avg	Sd
$r_F \cdot 10^3$	4.00	3.98	0.23	4.00	4.04	0.26	4.00	3.98	0.23
r_B	3.00	3.10	0.20	3.00	3.15	0.27	2.50	2.31	0.19
r_D	6.00	6.59	0.67	12.00	13.40	1.22		7.08	0.56
r_R	1.00	1.08	0.09	0.50	0.54	0.05		0.44	0.06
$\mathbb{E}[G]$	11.30	11.20	0.68	13.25	13.20	0.83	15.38	14.97	1.04
p	0.33	0.32	0.02	0.20	0.19	0.01	0.17	0.25	0.01
$q_{0.25}$	0.16	0.16	0.02	0.76	0.89	0.18	0.44	0.39	0.11
$q_{0.50}$	1.12	1.17	0.16	4.92	5.01	0.56	4.16	4.27	0.69
$q_{0.75}$	3.36	3.35	0.33	12.00	12.00	1.26	12.20	11.10	1.68
$q_{0.99}$	13.80	13.50	1.17	45.50	44.70	4.53	50.00	42.82	6.32

Clusters

	Short lived			Long lived			3 dark-states		
	Truth	Avg	Sd	Truth	Avg	Sd	Truth	Avg	Sd
$r_F \cdot 10^3$	4.00	4.00	0.27	4.00	3.98	0.24	4.00	3.99	0.26
r_B	3.00	3.06	0.20	3.00	3.10	0.26	2.50	2.29	0.23
r_D	6.00	6.53	0.62	12.00	13.10	1.39		6.97	0.63
r_R	1.00	1.06	0.09	0.50	0.53	0.06		0.43	0.06
$\mathbb{E}[G]$	11.30	11.30	0.69	13.25	13.30	0.79	15.38	15.03	1.23
p	0.33	0.32	0.02	0.20	0.19	0.01	0.17	0.25	0.02
$q_{0.25}$	0.16	0.16	0.02	0.76	0.90	0.16	0.44	0.38	0.11
$q_{0.50}$	1.12	1.19	0.18	4.92	5.09	0.52	4.16	4.33	0.74
$q_{0.75}$	3.36	3.41	0.39	12.00	12.30	1.23	12.20	11.30	1.80
$q_{0.99}$	13.80	13.70	1.37	45.50	45.50	4.56	50.00	43.68	6.82

Fibers

	Short lived			Long lived			3 dark-states		
	Truth	Avg	Sd	Truth	Avg	Sd	Truth	Avg	Sd
$r_F \cdot 10^3$	4.00	4.01	0.25	4.00	4.03	0.24	4.00	4.02	0.24
r_B	3.00	3.11	0.21	3.00	3.21	0.30	2.50	2.28	0.20
r_D	6.00	6.66	0.64	12.00	13.60	1.29		7.02	0.58
r_R	1.00	1.09	0.12	0.50	0.54	0.05		0.43	0.06
$\mathbb{E}[G]$	11.30	11.20	0.66	13.25	13.10	0.93	15.38	15.13	1.12
p	0.33	0.32	0.02	0.20	0.19	0.01	0.17	0.25	0.01
$q_{0.25}$	0.16	0.16	0.02	0.76	0.89	0.21	0.44	0.40	0.11
$q_{0.50}$	1.12	1.17	0.15	4.92	5.01	0.64	4.16	4.33	0.69
$q_{0.75}$	3.36	3.35	0.32	12.00	12.00	1.41	12.20	11.24	1.68
$q_{0.99}$	13.80	13.50	1.19	45.50	44.70	5.01	50.00	43.34	6.30

which, as noted by [37] and [1], holds exactly if G has a Poisson distribution. Given the 4-state model of PA-FP photophysics, we argue a Geometric distribution is more appropriate, in which case we would have

$$\mathbb{E}[G] = \frac{n_c}{2} + 1. \tag{A.7.3}$$

Using both these estimators, referred to as PC-PALM 1 and PC-PALM 2, respectively, we compared performance with the IBCpp fit on the simulated data, the results of which can be seen in Table A.5. We see that the IBCpp fit has lower bias and variance in every case, and is less sensitive to the blinking and clustering properties of PA-FP. PC-PALM is sensitive to the assumed distribution for G and $g_{\downarrow X}$, which is particularly clear in the 3 dark-state model, which has the most complex blinking behavior, and for the fibers, which has the most heterogeneous spatial distribution.

Table A.5: Comparison with the PC-PALM method for estimating $\mathbb{E}[G]$. Average (Avg), bias (Bias) given as the true value minus Avg, and standard deviation (Sd) of estimates is included. The first PC-PALM method assumes a Poisson distribution for G, whereas the second assumes a Geometric distribution. Best values are in bold.

CSR									
	Short lived			Long lived			3 dark-states		
	Avg	Bias	Sd	Avg	Bias	Sd	Avg	Bias	Sd
PC-PALM 1	21.10	9.80	1.52	25.40	12.15	1.92	41.20	25.82	4.40
PC-PALM 2	11.50	0.20	0.76	13.70	0.45	0.96	21.60	6.22	2.20
IBCpp	11.20	**-0.10**	**0.68**	13.20	**-0.05**	**0.83**	15.00	**-0.38**	**1.04**
Clusters									
	Short lived			Long lived			3 dark-states		
	Avg	Bias	Sd	Avg	Bias	Sd	Avg	Bias	Sd
PC-PALM 1	18.10	6.80	2.70	21.70	8.45	2.76	25.20	9.82	3.40
PC-PALM 2	10.00	-1.30	1.35	11.90	-1.35	1.38	13.60	-1.78	1.70
IBCpp	11.30	**0.00**	**0.69**	13.30	**0.05**	**0.79**	15.00	**-0.38**	**1.23**
Fibers									
	Short lived			Long lived			3 dark-states		
	Avg	Bias	Sd	Avg	Bias	Sd	Avg	Bias	Sd
PC-PALM 1	25.70	14.40	1.95	30.50	17.25	2.49	36.60	21.22	2.92
PC-PALM 2	13.80	2.50	0.98	16.20	2.95	1.25	19.30	3.92	1.46
IBCpp	11.20	**-0.10**	**0.66**	13.10	**-0.15**	**0.93**	15.10	**-0.28**	**1.12**

A.8 Summary and discussion

In the present paper we have established the IBCpp family of spatio-temporal clustered point processes, which is suitable for SMLM data, and we have provided a useful result on the mark correlation function. We constructed the PALM-IBCpp, which is an IBCpp model particularly well-suited for PALM data, and we have presented an algorithm for estimation of the blinking dynamics. The special structure of the mark correlation function in the IBCpp family allows for a semiparametric, moment-based approach to estimation, which can be carried out without having to specify a model for the proteins. The methods were validated on nuclear pore complex reference

data, where we could demonstrate a close correspondence between the model fit and expected blinking targets.

To demonstrate how the PALM-IBCpp can aid cluster analysis in PALM studies, we considered a real dataset expressing the adaptor protein LAT. We devised a blinking corrected global envelope test for CSR, and demonstrated it on the LAT data. In this way we could show that roughly half of the cell was subject to significant protein clustering, while the other half was not significantly different from CSR. We also performed a refitting study, again demonstrating the ability of the PALM-IBCpp model to accurately recover blinking dynamics in a realistic setting.

The ability to obtain blinking dynamics from any given ROI, without a need for calibration data or parametric modeling of protein locations, is perhaps the most important feature of our method, as it ensures that the estimated kinetic rates are relevant to the ROI being analyzed. The well-known sensitivity of PA-FP photodynamics to the experimental conditions [3, 33] means that kinetic rates obtained via a calibration sample may not be entirely applicable in another sample, emphasizing the importance of being able to directly estimate data artifacts from a given ROI. Another key aspect of our method is how quickly it can be carried out, even on large ROIs. Fitting to the LAT ROI in Section A.6, which consisted of 21742 localizations, took 45 seconds to complete, on a laptop with an Intel Core i7 Processor (4x 1.80 GHz). The RAM usage was similarly modest, requiring 1.5GB at the peak.

The drawbacks of our method are as follows. First, although the IBCpp family is generally applicable to SMLM data, the estimation algorithm developed here is specifically for the PALM-IBCpp, and estimation in other SMLM modalities would require additional work. The 4-state photoblinking model will be appropriate for some PA-FP, whereas it will be a surrogate model for other PA-FP with more complex blinking dynamics. As we have seen, the PALM-IBCpp fit is still able to capture important descriptors of blinking dynamics when the model is misspecified, but the parameters of the true blinking model will remain unknown. Finally, as the methods are built on a semiparametric model, and a complex set of estimation choices, theoretical results on the estimators are not forthcoming. The simulation studies suggest that the estimators are well behaved, but we can only guess at this in general.

Acknowledgements

This work was supported by the Centre for Stochastic Geometry and Advanced Bioimaging, funded by grant 8721 from the Villum Foundation. We acknowledge the use of the Nikon Imaging Facility (NIC) at King's College London for data acquisition.

Code availability

Efficient code for estimation, simulation, and more in the PALM-IBCpp model has been developed, and is available at github.com/Louis-Jensen/PALMIBCpp.

A.I Supplementary material

Supplement A: Moment results for IBCpp models

Let O be an IBCpp with motion-invariant protein process $_{\downarrow}X$. Deriving the results of Section 3.2 is perhaps most easily done by taking as starting point the *f-weighted second factorial moment measure*, $\alpha_f^{(2)}$, given as

$$\alpha_f^{(2)}(A) = \mathbb{E}\left[\sum_{(o_1,t_{o_1}),(o_2,t_{o_2})\in O^2}^{\neq} \mathbb{1}_A(o_1,o_2) f(t_{o_1},t_{o_2})\right], \tag{A.I.1}$$

for $A \in \mathbb{R}^d \times \mathbb{R}^d$ a Borel set. By use of a Cambell theorem we obtain

$$\alpha_f^{(2)}(A) = \int_A \left[\int f(t_{o_1},t_{o_2}) dM^{(2)}_{O|(o_1,o_2)}(t_{o_1},t_{o_2})\right] d\alpha_O^{(2)}(o_1,o_2), \tag{A.I.2}$$

so that, comparing the above with the definition of the mark correlation function, we get the alternative characterization

$$k_O^f(o_1,o_2) = \frac{1}{\int\int f(t_{o_1},t_{o_2}) dM^{(1)}_{O|o_1}(t_{o_1}) dM^{(1)}_{O|o_2}(t_{o_2})} \frac{\partial \alpha_f^{(2)}}{\partial \alpha_O^{(2)}}(o_1,o_2), \tag{A.I.3}$$

and we need merely compute the involved factors. We first compute the 1-point mark distributions. Let $A \subset \mathbb{R}^d$ and $B \subset \mathbb{R}_+$ be Borel sets, then we obtain

$$\begin{aligned}
\Lambda_O(A\times B) &= \mathbb{E}\left[\sum_{x\in {}_{\downarrow}X} \sum_{(y,t_y)\in Y_x} \mathbb{1}_A(y)\mathbb{1}_B(t_y)\right] + \mathbb{E}\left[\sum_{(e,t_e)\in E} \mathbb{1}_A(e)\mathbb{1}_B(t_e)\right] && \text{(A.I.4)}\\
&= \mathbb{E}\left[\sum_{x\in {}_{\downarrow}X} \sum_{i=1}^{G} \mathbb{1}_A(x+\epsilon_i)\mathbb{1}_B(t_{y_i})\right] + \mathbb{E}\left[\sum_{(e,t_e)\in E} \mathbb{1}_A(e)\mathbb{1}_B(t_e)\right] && \text{(A.I.5)}\\
&= \frac{\mathbb{E}\left[\sum_{i=1}^G \mathbb{1}_B(t_{y_i})\right]}{\mathbb{E}[G]} \int_A \lambda_{{}_{\downarrow}Z} dz + \int_B \frac{\mathbb{1}(t\in[0,b])}{b} dt \int_A \lambda_{{}_{\downarrow}E} de && \text{(A.I.6)}\\
&= \int_A \left(\eta \frac{\mathbb{E}\left[\sum_{i=1}^G \mathbb{1}_B(t_{y_i})\right]}{\mathbb{E}[G]} + (1-\eta)\int_B \frac{\mathbb{1}(t\in[0,b])}{b} dt\right) d\Lambda_O(o), && \text{(A.I.7)}
\end{aligned}$$

where we exploited that the ϵ_i are independent of $_{\downarrow}X$, G, and $\{t_{y_i}\}_{i=1}^G$, when going from the second to the third line. We also used the assumed form for the intensity function of E in this step. From the above, we see that all involved mark distributions are independent of locations, with

$$M_Z^{(1)}(B) = \frac{\mathbb{E}\left[\sum_{i=1}^G \mathbb{1}_B(t_{y_i})\right]}{\mathbb{E}[G]}, \tag{A.I.8}$$

$$M_E^{(1)}(B) = \int_B \frac{\mathbb{1}(t\in[0,b])}{b} dt, \tag{A.I.9}$$

$$M_O^{(1)}(B) = \eta M_Z^{(1)}(B) + (1-\eta) M_E^{(1)}(B), \tag{A.I.10}$$

based on which the normalization for k_O^f is found

$$\gamma_2^O(f) = \int\int f(t_{o_1}, t_{o_2}) dM_O^{(1)}(t_{o_1}) dM_O^{(1)}(t_{o_2}) \tag{A.I.11}$$

$$= \eta^2 \gamma_2(f) + (1-\eta)^2 \gamma_2^E(f) + 2(1-\eta)\eta \gamma_2^{EZ}(f), \tag{A.I.12}$$

where

$$\gamma_2^E(f) = \int\int f(t_1, t_2) dM_E^{(1)}(t_1) dM_E^{(1)}(t_2), \tag{A.I.13}$$

$$\gamma_2^{EZ}(f) = \int\int f(t_1, t_2) dM_E^{(1)}(t_1) dM_Z^{(1)}(t_2). \tag{A.I.14}$$

Next, we consider the second factorial moment measure of the typical cluster, $\alpha_{Y_x}^{(2)}$, which will be needed below. For arbitrary blinking cluster Y_x and Borel sets $A \subset \mathbb{R}^d \times \mathbb{R}^d$, $B \subset \mathbb{R}_+ \times \mathbb{R}_+$, we have

$$\alpha_{Y_x}^{(2)}(A \times B) = \mathbb{E}\left[\sum_{(i,j)=1}^{G} \mathbb{1}(i \neq j) \mathbb{1}_A(x + \epsilon_i, x + \epsilon_j) \mathbb{1}_B(t_{y_i}, t_{y_j})\right] \tag{A.I.15}$$

$$= \mathbb{E}\left[\sum_{(i,j)=1}^{G} \mathbb{1}(i \neq j) \mathbb{1}_B(t_{y_i}, t_{y_j})\right] \tag{A.I.16}$$

$$\times \int_A h_\epsilon(x_1 - x) h_\epsilon(x_2 - x) d(x_1, x_2),$$

obtained by averaging out the ϵ_i by conditioning on $(G, \{t_{y_i}\}_{i=1}^G)$, from which follows (by observing what happens for $B = \mathbb{R}_+^2$)

$$\alpha_{\downarrow Y_x}^{(2)}(A) = \mathbb{E}[G(G-1)] \int_A h_\epsilon(x_1 - x) h_\epsilon(x_2 - x) d(x_1, x_2), \tag{A.I.17}$$

$$M_{Y_x}^{(2)} = \frac{\mathbb{E}\left[\sum_{(i,j)=1}^{G} \mathbb{1}(i \neq j) \mathbb{1}_B(t_{y_i}, t_{y_j})\right]}{\mathbb{E}[G(G-1)]}, \tag{A.I.18}$$

and we see that $M_{Y_x}^{(2)}$ is independent of x. Finally, for the density of $\alpha_f^{(2)}$, we split the summation according to the process memberships of each pair (respectively, two points from the same cluster, points from different clusters, one cluster and one noise point, two noise points):

$$\alpha_f^{(2)}(A) = \mathbb{E}\left[\sum_{x \in \downarrow X} \sum_{(i,j)=1}^{G} \mathbb{1}(i \neq j) \mathbb{1}_A(x + \epsilon_i, x_2 + \epsilon_j) f(t_{y_i}, t_{y_j})\right] \tag{A.I.19}$$

$$+ \mathbb{E}\left[\sum_{(x_1,x_2) \in \downarrow X^2}^{\neq} \sum_{i=1}^{G} \sum_{j=1}^{G'} \mathbb{1}_A(x_1 + \epsilon_i, x_2 + \epsilon_j') f(t_{y_i}, t_{y_j}')\right]$$

$$+ \mathbb{E}\left[\sum_{(z,t_z) \in Z} \sum_{(e,t_e) \in E} \mathbb{1}_A(z, e) f(t_z, t_e)\right] + \mathbb{E}\left[\sum_{(z,t_z) \in Z} \sum_{(e,t_e) \in E} \mathbb{1}_A(e, z) f(t_e, t_z)\right]$$

$$+ \mathbb{E}\left[\sum_{(e_1,t_{e_1}),(e_2,t_{e_2}) \in E^2}^{\neq} \mathbb{1}_A(e_1, e_2) f(t_{e_1}, t_{e_2})\right].$$

Using Equation (A.I.17) and A.I.18, recalling that E is a Poisson process independent of Z, and using that f is symmetrical, we see that

$$\begin{aligned}\alpha_f^{(2)}(A) &= \gamma_1(f)\int \alpha_{\downarrow Y_0}^{(2)}(A-(x,x))\lambda_{\downarrow X}dx \qquad \text{(A.I.20)}\\ &+ \gamma_2(f)\int (\Lambda_{\downarrow Y_0})^2(A-(x_1,x_2))d\alpha_{\downarrow X}^{(2)}(x_1,x_2)\\ &+ 2\gamma_2^{EZ}(f)\int_A \lambda_{\downarrow Z}\lambda_{\downarrow E}d(o_1,o_2)\\ &+ \gamma_2^{E}(f)\int_A \lambda_{\downarrow E}^2 d(o_1,o_2),\\ &= \gamma_1(f)\mathbb{E}[G(G-1)]\,\lambda_{\downarrow X}\int_A\int h_\epsilon(o_1-x)h_\epsilon(o_2-x)dx\,d(o_1,o_2) \qquad \text{(A.I.21)}\\ &+ \gamma_2(f)\lambda_{\downarrow X}^2\mathbb{E}[G]^2\int_A\int g_{\downarrow X}(\|x_1-x_2\|)h(o_1-x_1)h(o_2-x_2)d(x_1,x_2)d(o_1,o_2)\\ &+ 2\gamma_2^{EZ}(f)\lambda_{\downarrow Z}\lambda_{\downarrow E}\int_A d(o_1,o_2)\\ &+ \gamma_2^{E}(f)\lambda_{\downarrow E}^2\int_A d(o_1,o_2).\end{aligned}$$

Write m for the Lebesgue measure on $\mathbb{R}^d$. Then, using the rotational symmetry of h_ϵ and $g_{\downarrow X}$, it follows that $\frac{\partial\alpha_f^{(2)}}{\partial m^2}(o_1,o_2)$ depends only on $r=\|o_1-o_2\|$, and

$$\frac{\partial\alpha_f^{(2)}}{\partial m^2}(r) = \gamma_1(f)n_c\lambda_{\downarrow Z}(h_\epsilon * h_\epsilon)(r) + \gamma_2(f)\lambda_{\downarrow Z}^2(h_\epsilon * g_{\downarrow X})(r) + 2\gamma_2^{EZ}(f)\lambda_{\downarrow Z}\lambda_{\downarrow E} + \gamma_2^{E}(f)\lambda_{\downarrow E}^2, \qquad \text{(A.I.22)}$$

where

$$(h_\epsilon * g_{\downarrow X})(r) = \int g_{\downarrow X}(\|x_1-x_2\|)h(o_1-x_1)h(o_2-x_2)d(x_1,x_2), \qquad \text{(A.I.23)}$$

for $\|o_1-o_2\|=r$, and in particular

$$\begin{aligned}\gamma_2^O(f)g_{\downarrow O}k_O^f(r) &= \lambda_{\downarrow O}^{-2}\frac{\partial\alpha_f^{(2)}}{\partial m^2}(r) \qquad \text{(A.I.24)}\\ &= \gamma_1(f)\frac{\eta}{\lambda_{\downarrow O}}n_c(h_\epsilon * h_\epsilon)(r) + \gamma_2(f)\eta^2((h_\epsilon * g_{\downarrow X})(r)-1) + \gamma_2^O(f). \qquad \text{(A.I.25)}\end{aligned}$$

By setting $f=1$ we see that

$$g_{\downarrow O} = \frac{\eta}{\lambda_{\downarrow O}}n_c(h_\epsilon * h_\epsilon)(r) + \eta^2((h_\epsilon * g_{\downarrow X})(r)-1) + 1, \qquad \text{(A.I.26)}$$

and using this above we obtain the desired equation

$$\gamma_2^O(f)k_O^f(r)g_{\downarrow O}(r) = (\gamma_1(f)-\gamma_2(f))\left[\frac{\eta}{\lambda_{\downarrow O}}n_c(h_\epsilon * h_\epsilon)(r)\right] + \gamma_2(f)\left[g_{\downarrow O}(r)-1\right] + \gamma_2^O(f). \qquad \text{(A.I.27)}$$

Supplement B: Estimation procedures in the PALM-IBCpp

Extracting spatially invariant statistics from data

In this section we will consider how to extract estimators for the quantities

$$\zeta_u = (\gamma_1(f_u) - \gamma_2(f_u))\, n_c, \quad u \in T.$$

Recall that for an IBCpp, we have

$$\zeta_u = \frac{\left(\gamma_2^O(f_u) k_O^{f_u}(r) g_{\downarrow O}(r) - \gamma_2(f_u)\left[g_{\downarrow O}(r) - 1\right] - \gamma_2^O(f_u)\right)\lambda_{\downarrow O}}{(h_\epsilon * h_\epsilon)(r)\eta}, \quad u \in T, \tag{A.I.28}$$

and estimation of ζ_u is thus naturally done via estimators for each component on the right hand side. Starting with η and $\lambda_{\downarrow O}$, these are both functions of the spatial intensities of O and E. The standard estimator for the spatial intensity of a point process is the relative number of points per area. In particular, if we have access to O and E in separate windows, we set

$$\hat{\lambda}_{\downarrow E} = \frac{N_E}{|W_E|}, \tag{A.I.29}$$

$$\hat{\lambda}_{\downarrow O} = \frac{N}{|W|}, \tag{A.I.30}$$

where e.g. $|W|$ is the area of W, and consequently we get

$$\hat{\eta} = 1 - \frac{\hat{\lambda}_{\downarrow E}}{\hat{\lambda}_{\downarrow O}}. \tag{A.I.31}$$

If we do not have access to E in this way, or if we do not wish to account for background noise, we set instead $\hat{\eta} = 1$.

Moving on to estimators for the pair- and mark correlation functions, $\hat{g}_{\downarrow O}(r)$ and $\hat{k}_O^{f_u}(r)$, these are easily obtained using a number of standard implementations, for instance using the kernel smoothing estimators in the R package Spatstat, or by numerical differentiation of the mark-weighted K function [4, p. 646], which is significantly faster for large datasets, and is the method used in the supplied code. One detail that must be dealt with, however, is which spatial distances, r, we wish to consider. A default choice that emphasizes distances reflecting the spatial scale of blinking clusters is suggested in Algorithm 1 of the main text.

Next, for the cluster autoconvolution $(h_\epsilon * h_\epsilon)$, note first that the density of P_ϵ, h_ϵ, can be obtained as a mean over Gaussian densities where the variance follows P_σ. By changing the order of mean and the integration we thus obtain

$$(h_\epsilon * h_\epsilon)(r) = \int h_\epsilon(y_1 - x) h_\epsilon(y_2 - x) dx = \mathbb{E}\left[\frac{e^{-\frac{r^2}{2(\sigma_1^2+\sigma_2^2)}}}{2\pi(\sigma_1^2+\sigma_2^2)}\right], \tag{A.I.32}$$

where the mean is with respect to σ_1 and σ_2 independently following P_σ. We do not know P_σ, but we do have predictions of σ_k in $\hat{\sigma}_k$ for each $k \in \{1, 2, .., N\}$, and the

natural estimator of $(h_\epsilon * h_\epsilon)$ is then to replace P_σ with the empirical distribution, $P_{\hat{\sigma}}$, of the observed localization uncertainties, that is

$$\widehat{(h_\epsilon * h_\epsilon)}(r) = \mathbb{E}\left[\frac{e^{-\frac{r^2}{2(\hat{\sigma}_1^2+\hat{\sigma}_2^2)}}}{2\pi(\hat{\sigma}_1^2+\hat{\sigma}_2^2)}\right], \quad r \in R. \tag{A.I.33}$$

with $\hat{\sigma}_1$ and $\hat{\sigma}_2$ independently following $P_{\hat{\sigma}}$. This mean can be computed e.g. via sampling $\hat{\sigma}_1$ and $\hat{\sigma}_2$ a larger number of times with replacement from $\{\hat{\sigma}_k\}_{k=1}^N$.

Finally, we need estimators of $\gamma_2(f_u)$ and $\gamma_2^O(f_u)$. Here, γ_2^O is more well-known as the normalization constant in the mark correlation function, and a standard estimator is

$$\hat{\gamma}_2^O(f_u) = \frac{1}{N(N-1)} \sum_{i,j}^{\neq} \mathbb{1}(|t_{o_i} - t_{o_j}| \leq u), \tag{A.I.34}$$

see [10, p. 393]. As the number of pairs in this sum can be quite large, a less computationally expensive estimator first sub-samples a smaller number of pairs to sum over. Next, for $\gamma_2(f_u)$, note first that $\gamma_2^O(f_u)$ has a more formal description as the mean

$$\gamma_2^O(f_u) = \int_0^\infty \int_0^\infty f(t_1,t_2) dM_O^{(1)}(t_1) dM_O^{(1)}(t_2), \tag{A.I.35}$$

where $M_O^{(1)}$ is the 1-point mark distribution of O. This is important in the context of estimating $\gamma_2(f_u)$ since we have similarly

$$\gamma_2(f_u) = \int_0^\infty \int_0^\infty f(t_1,t_2) dM_Z^{(1)}(t_1) dM_Z^{(1)}(t_2), \tag{A.I.36}$$

where $M_Z^{(1)}$ is the 1-point mark distribution of the blinking clusters in Z, which is connected to $M_O^{(1)}$ by the identity

$$M_O^{(1)}(t) = \eta M_Z^{(1)}(t) + (1-\eta)\frac{t}{b}, \tag{A.I.37}$$

c.f. Supplement A. This suggests that we can estimate $\gamma_2(f_u)$ by first estimating the $M_Z^{(1)}$ using the empirical mark distribution $\hat{M}_O^{(1)}$ via

$$\hat{M}_Z^{(1)}(t) = \frac{\hat{M}_O^{(1)}(t) - (1-\hat{\eta})\frac{t}{b}}{\hat{\eta}} \tag{A.I.38}$$

and finally computing

$$\hat{\gamma}_2(f_u) = \mathbb{E}[\mathbb{1}(|t_1 - t_2|)], \tag{A.I.39}$$

where t_1 and t_2 follow $\hat{M}_Z^{(1)}$. This can be done by sampling from $\hat{M}_Z^{(1)}$ a large number of times, which can be accomplished using for instance the method of inverse transform sampling.

We are finally in a position to extract ζ_u. Since Equation (A.I.28) states that the denominator and enumerator on the right hand side are proportional for each r, a least squares fit suggests the estimators

$$\hat{\zeta}_u = \frac{\hat{\lambda}_{\downarrow O}}{\hat{\eta}} \frac{\sum_{r\in R}\left[\hat{\gamma}_2^O(f_u)\hat{k}_O^{f_u}(r)\hat{g}_{\downarrow O}(r) - \hat{\gamma}_2(f_u)(\hat{g}_{\downarrow O}(r)-1) - \hat{\gamma}_2^O(f_u)\right]\left[\widehat{(h_\epsilon * h_\epsilon)}(r)\right]}{\sum_{r\in R}\left[\widehat{(h_\epsilon * h_\epsilon)}(r)\right]^2}, \tag{A.I.40}$$

for each $u \in T$.

Kinetic rate estimation

With the spatially invariant statistics in $\{\hat{\zeta}_u\}_{u\in T}$ at hand, we are able to estimate the kinetic rates. We set up the weighted minimum contrast problem

$$\min_{\hat{r}_D,\hat{r}_R,\hat{r}_B} \sum_{u\in T}\sum_{r\in R}\left(\frac{\hat{\zeta}_u}{\hat{\gamma_2}(f_u)}\right)^2\left(\hat{\zeta}_u - (\gamma_1(f_u)-\hat{\gamma}_2(f_u))n_c\right)^2, \tag{A.I.41}$$

where $\frac{\hat{\zeta}_u}{\hat{\gamma_2}(f_u)}$ are weights chosen to emphasize the ζ_u that are most informative. These weights are motivated by the fact that

$$\frac{\zeta_u}{\gamma_2(f_u)} = \left(\frac{\gamma_1(f_u)}{\gamma_2(f_u)} - 1\right)n_c,$$

puts most weight on $u \in T$ where $\gamma_1(f_u)$ moves between 0 and 1, while down-weighing large u for which $\gamma_1(f_u)$ is constantly 1 and weakly informative. In order to solve the minimization problem in A.I.41, we need to know how $\gamma_1(f_u)$ and n_c depend on (r_D, r_R, r_B), which leads to some rather gritty computations. In fact, we must be satisfied with asymptotically ($\Delta \to 0$) exact approximations, derivations of which can be found in Supplement C. Define the following random variables and associated characteristic functions

$$\begin{aligned}
&N_b \sim Geom_1(p),\\
&W_F \sim Exp(r_D + r_B),\\
&W_D \sim Exp(r_R),\\
&W_I \sim Exp(r_F),\\
&\phi_R(v) = \mathbb{E}\left[e^{ivW_R}\right],\\
&\phi_F(v) = \mathbb{E}\left[e^{ivW_F}\right],\\
&\phi_{(F+R)}(v) = \mathbb{E}\left[e^{ivW_F}\right]\mathbb{E}\left[e^{ivW_R}\right],
\end{aligned}$$

where $p = \frac{r_B}{r_D+r_B}$ is the *bleaching probability*, and $Geom_1$ is a geometric distribution starting from 1. Here, N_b has the interpretation as the number of blinks (F-state visits), and W_F is the holding time in state F, and similarly for W_D and W_I. Next, define the following quantities

$$\begin{aligned}
A(v) &= \frac{2\mathbb{E}[N_b]\left(\phi_F(v)e^{-iv\Delta\frac{1}{2}} + \left(\frac{\mathbb{E}[W_F]}{\Delta} - \frac{1}{2}\right)(e^{-\Delta iv}-1) - 1\right)}{(1-e^{-\Delta iv})^2},\\
B(v) &= \phi_R(v)\left(\mathbb{E}\left[\phi_{(F+R)}(v)^{N_b}\right] - 1 - \mathbb{E}[N_b](\phi_{(F+R)}(v)-1)\right),\\
C(v) &= \frac{2e^{-iv\Delta 2}}{(1-e^{-\Delta iv})^2}\left(\frac{\phi_F(v)e^{iv\Delta\frac{1}{2}}-1}{\phi_{(F+R)}(v)-1}\right)^2,\\
D &= \mathbb{E}\left[N_b^2\right]\left(\frac{\mathbb{E}[W_F]}{\Delta} + \frac{1}{2}\right)^2 + \mathbb{E}[N_b]\left[\frac{\mathbb{E}\left[W_F^2\right] - \mathbb{E}[W_F]^2}{\Delta^2} - \frac{\mathbb{E}[W_F]}{\Delta} - \frac{1}{2}\right],
\end{aligned}$$

and the CDF $u \mapsto \gamma_1(f_u)$ then has characteristic function given as approximately

$$\phi(v) \approx \frac{A(v) + B(v)C(v)}{D}. \tag{A.I.42}$$

All the involved mean values are elementary to compute, and we can thus obtain our approximate $\gamma_1(f_u)$ by numerically inverting $\phi(v)$, which can be done efficiently using the fast Fourier transform, see e.g. [14].

For n_c, we recall that

$$n_c = \frac{\mathbb{E}\left[G^2\right]}{\mathbb{E}[G]} - 1, \tag{A.I.43}$$

and we simply plug in the approximations

$$\begin{aligned}
\mathbb{E}[G] &\approx \mathbb{E}[N_b]\left(\frac{\mathbb{E}[W_F]}{\Delta} + 1\right) - \mathbb{E}[N_b - 1]\,\mu_R^1, \\
\mathbb{E}\left[G^2\right] &\approx \mathbb{E}\left[N_b^2\right]\left(\frac{\mathbb{E}[W_F]}{\Delta} + 1\right)^2 + \mathbb{E}[N_b]\,\frac{\mathbb{E}\left[W_F^2\right] - \mathbb{E}[W_F]^2}{\Delta^2} \\
&\quad + \mathbb{E}\left[(N_b - 1)^2\right](\mu_R^1)^2 + \mathbb{E}[N_b - 1]\left(\mu_R^2 - (\mu_R^1)^2\right) \\
&\quad - 2\mathbb{E}[N_b(N_b - 1)]\left(\frac{\mathbb{E}[W_F]}{\Delta} + 1\right)\mu_R^1,
\end{aligned}$$

with

$$\begin{aligned}
\mu_R^1 &= \frac{r_R\Delta + e^{-r_R\Delta} - 1}{r_R\Delta}, \\
\mu_R^2 &= \frac{2(1 - e^{-r_R\Delta} - r_R\Delta) + (r_R\Delta)^2}{(r_R\Delta)^2}.
\end{aligned}$$

The functions f_u were selected precisely to eliminate the influence of r_F, and r_F consequently plays no role in the minimization problem above. In order to estimate r_F we thus need an additional step. We have the following asymptotically exact relation

$$r_R \approx \left(\frac{1}{2}\gamma_2(f_+) - A_2 - B_2\right)^{-1},$$

where $f_+(t_1, t_2) = t_1 + t_2$, and

$$\begin{aligned}
A_2 &= \frac{\frac{\mathbb{E}\left[W_F^2\right]}{2\Delta} + \mathbb{E}[W_F] + \frac{3\Delta}{8}}{\frac{\mathbb{E}[W_F]}{\Delta} + \frac{1}{2}}, \\
B_2 &= \frac{(\frac{\mathbb{E}[W_F]}{\Delta} + \frac{1}{2})(\frac{1}{2}\mathbb{E}[N_b(N_b - 1)](\mathbb{E}[W_F] + \mathbb{E}[W_R]) + \mathbb{E}[N_b]\Delta\frac{1}{2})}{\mathbb{E}[N_b](\frac{\mathbb{E}[W_F]}{\Delta} + \frac{1}{2})}.
\end{aligned}$$

Write $\hat{A}_2$ and $\hat{B}_2$ for A_2 and B_2 computed with the estimated $(\hat{r}_D, \hat{r}_R, \hat{r}_B)$ in the previous step. We estimate $\gamma_2(f_+)$ directly from the observed timepoints using (A.I.38), and obtain an estimator for r_F as

$$\hat{r}_F = \left(\frac{\frac{1}{N}\sum_{i=1}^N t_{o_i} - (1 - \hat{\eta})\frac{b}{2}}{\hat{\eta}} - \hat{A}_2 - \hat{B}_2\right)^{-1}. \tag{A.I.44}$$

If the dataset recording was stopped too early, $\hat{r}_F$ may be subject to censoring biases, as we then only observed blinking clusters beginning before time b, and $\hat{r}_F^{-1}$ is then rather estimating the mean of the conditional distribution $(W_I | W_I < b)$. A corrected

estimate can be found by equating this mean with its theoretical counterpart, i.e. solving

$$\frac{e^{r_F^c b} - r_F^c b - 1}{r_F^c (e^{r_F^c b} - 1)} - \hat{r}_F^{-1} = 0,$$

in r_F^c.

Supplement C: Approximate discretized statistics

Approximate $\phi(v)$

The mean value to compute is formally

$$\phi(v) := \frac{\mathbb{E}\left[\sum_{j_1, j_2 \in \{1,..,G\}}^{\neq} e^{iv|m_{j_1} - m_{j_2}|}\right]}{\mathbb{E}[G(G-1)]}, \tag{A.I.45}$$

where we have dropped the heavier notation of timepoints in the main text, so that (m_{j_1}, m_{j_2}) are arrival times (marks) j_1 and j_2 in the typical blinking cluster. Denote again by N_b the number of F-state visits (number of blinks), and by F_s the observed timepoints between the entrance to the s'th and $(s+1)$'th F-state visits for $s < N_b$, and F_{N_b} are all observed timepoints after the last entrance to the F-state. Below, we will assume w.l.o.g. that the timepoints are sorted, that is $m_{j_1} < m_{j_2}$ for $(j_2 > j_1)$ when $(m_{j_1}, m_{j_2}) \in F_s$ - this is entirely as a notational convenience. We can split the summation according to whether m_{j_1} and m_{j_2} are from the same F_s, and otherwise how many F-state visits are separating them. Thus

$$\begin{aligned}\phi(v) = &\frac{\mathbb{E}\left[\sum_{s=1}^{N_b} \sum_{(m_{j_1}, m_{j_2}) \in F_s}^{\neq} e^{iv|m_{j_1} - m_{j_2}|}\right]}{\mathbb{E}[G(G-1)]} \\ &+ \frac{\mathbb{E}\left[\sum_{s_1=1}^{N_b} \sum_{s_2=1}^{N_b} \mathbb{1}(s_1 \neq s_2) \sum_{m_{j_1} \in F_{s_1}} \sum_{m_{j_2} \in F_{s_2}} e^{iv|m_{j_1} - m_{j_2}|}\right]}{\mathbb{E}[G(G-1)]}.\end{aligned} \tag{A.I.46}$$

To compute these terms, referred to as the "non-separated" and "separated" terms, respectively, we write the involved quantities in terms of a continuous part, and an error part, and demonstrate that the errors vanish asymptotically, and in particular can be ignored for a given framerate as a valid approximation.

First, we consider the number of timepoints in F_s, $|F_s|$. Since only those frames that do not fully overlap the signal from the s'th F-visit (of which there are at most 2) cause discretization effects, we can write

$$|F_s| = \frac{W_{F_s}}{\Delta} + E_s^F, \tag{A.I.47}$$

where W_{F_s} is the waiting time that was spent on the s'th visit to the F state, and E_s^F is an error term with

$$P(E_s^F \in (-1, 2)) = 1, \tag{A.I.48}$$

and in particular, we obtain for G

$$G = \sum_{s=1}^{N_b} |F_s| = \sum_{s=1}^{N_b} \frac{W_{F_s}}{\Delta} + \sum_{s=1}^{N_b} E_s^F. \tag{A.I.49}$$

Next, consider the inner sum from the non-separated term:

$$\sum_{(m_{j_1},m_{j_2})\in F_s}^{\neq} e^{iv|m_{j_1}-m_{j_2}|}. \tag{A.I.50}$$

Here, note that the first observed timepoint in F_s, m_1^s, can be written as

$$m_1^s = E_s^{m_1} + W_I + \sum_{k=1}^{s-1}(W_{F_k} + W_{R_k}), \tag{A.I.51}$$

since there is always a waiting time of W_I spent in the inactive state, and $(s-1)$ visits in and out of the F state before the s'th visit. $E_s^{m_1}$ is again a discretization error, with magnitude

$$P(E_s^{m_1} \in (0,\Delta)) = 1. \tag{A.I.52}$$

Since each member of F_s is a whole number of Δ-increments away from m_1^s, this in particular means that, for $(m_{j_1}, m_{j_2}) \in F_s$ with $j_2 > j_1$:

$$|m_{j_1} - m_{j_2}| = (j_2 - j_1)\Delta, \tag{A.I.53}$$

and any discretization effects, and the time spent in the I-state, can be seen to disappear here. We can now expand on the non-separate term enumerator:

$$\mathbb{E}\left[\sum_{s=1}^{N_b}\sum_{(m_{j_1},m_{j_2})\in F_s}^{\neq} e^{iv|m_{j_1}-m_{j_2}|}\right] \tag{A.I.54}$$

$$=\mathbb{E}\left[\sum_{s=1}^{N_b}\sum_{(j_1,j_2)\in\{1,2,..,|F_s|\}}^{\neq} e^{iv(j_1\vee j_2 - j_1\wedge j_2)\Delta}\right] \tag{A.I.55}$$

$$=2\mathbb{E}\left[\sum_{s=1}^{N_b}\sum_{j=1}^{|F_s|-1}(|F_s|-j)e^{ivj\Delta}\right] \tag{A.I.56}$$

$$=2\mathbb{E}\left[\sum_{s=1}^{N_b}\frac{e^{iv\Delta(|F_s|-1)} + e^{-iv\Delta}(|F_s|-1) - |F_s|}{(e^{-iv\Delta}-1)^2}\right] \tag{A.I.57}$$

$$=2\mathbb{E}\left[\sum_{s=1}^{N_b}\frac{e^{ivW_{F_s}}e^{iv\Delta(E_s^F-1)} + e^{-iv\Delta}(\frac{W_{F_s}}{\Delta} + E_s^F - 1) - \frac{W_{F_s}}{\Delta} - E_s^F}{(e^{-iv\Delta}-1)^2}\right], \tag{A.I.58}$$

At this point, consider what happens in the limit as $\Delta \to 0$ for the complete non-

separate term:

$$\lim_{\Delta\to 0}\frac{\mathbb{E}\left[\sum_{s=1}^{N_b}\sum_{(m_{j_1},m_{j_2})\in F_s}^{\neq} e^{iv|m_{j_1}-m_{j_2}|}\right]}{\mathbb{E}[G(G-1)]} \tag{A.I.59}$$

$$=\frac{2\mathbb{E}\left[\lim_{\Delta\to 0}\sum_{s=1}^{N_b} e^{ivW_{F_s}}e^{iv\Delta(E_s^F-1)}+\frac{W_{F_s}}{\Delta}(e^{-iv\Delta}-1)+E_s^F(e^{-iv\Delta}-1)-e^{-iv\Delta}\right]}{\lim_{\Delta\to 0}(e^{-iv\Delta}-1)^2\left[\mathbb{E}\left[\left(\sum_{s=1}^{N_b}\frac{W_{F_s}}{\Delta}+\sum_{s=1}^{N_b}E_s^F\right)^2\right]-\mathbb{E}\left[\sum_{s=1}^{N_b}\frac{W_{F_s}}{\Delta}+\sum_{s=1}^{N_b}E_s^F\right]\right]} \tag{A.I.60}$$

$$=\frac{2\mathbb{E}\left[\sum_{s=1}^{N_b}1+ivW_{F_s}-e^{iW_{F_s}}\right]}{v^2\mathbb{E}\left[\left(\sum_{s=1}^{N_b}W_{F_s}\right)^2\right]} \tag{A.I.61}$$

$$=\frac{2\mathbb{E}[N_b](1+iv\mathbb{E}[W_F]-\phi_F(u))}{v^2(\mathbb{E}[N_b]\mathbb{E}\left[W_F^2\right]+\mathbb{E}[N_b(N_b-1)]\mathbb{E}[W_F]^2)}. \tag{A.I.62}$$

Predictably the rounding errors play no role in the limit, and as a simple approximation we therefore set $E_s^F=\frac{1}{2}$ to the midpoint of its domain for all s, to obtain the asymptotically exact approximation:

$$\frac{\mathbb{E}\left[\sum_{s=1}^{N_b}\sum_{(m_{j_1},m_{j_2})\in F_s}^{\neq} e^{iv|m_{j_1}-m_{j_2}|}\right]}{\mathbb{E}[G(G-1)]} \tag{A.I.63}$$

$$\approx\frac{2\mathbb{E}\left[\sum_{s=1}^{N_b} e^{ivW_{F_s}}e^{-iv\Delta\frac{1}{2}}+e^{-iv\Delta}(\frac{W_{F_s}}{\Delta}-\frac{1}{2})-\frac{W_{F_s}}{\Delta}-\frac{1}{2}\right]}{(e^{-iv\Delta}-1)^2\left[\mathbb{E}\left[\left(\sum_{s=1}^{N_b}\frac{W_{F_s}}{\Delta}+\frac{1}{2}\right)^2\right]-\mathbb{E}\left[\sum_{s=1}^{N_b}\frac{W_{F_s}}{\Delta}+\frac{1}{2}\right]\right]} \tag{A.I.64}$$

$$=\frac{2\mathbb{E}[N_b](\phi_F(v)e^{-iv\frac{\Delta}{2}}+e^{-iv\Delta}(\frac{\mathbb{E}[W_F]}{\Delta}-\frac{1}{2})-\frac{\mathbb{E}[W_F]}{\Delta}-\frac{1}{2})}{(e^{-iv\Delta}-1)^2\left(\mathbb{E}\left[N_b^2\right]\left(\frac{\mathbb{E}[W_F]}{\Delta}+\frac{1}{2}\right)^2+\mathbb{E}[N_b]\left[\frac{\mathbb{E}\left[W_F^2\right]-\mathbb{E}[W_F]^2}{\Delta^2}-\frac{\mathbb{E}[W_F]}{\Delta}-\frac{1}{2}\right]\right)}, \tag{A.I.65}$$

which is $\frac{A(v)}{D}$.

Now, consider the separate summation enumerator. We use similar techniques as before. Note that for F_{s_1} and F_{s_2} there are $|s_1-s_2-1|$ W_F waiting times, and $|s_1-s_2|$ W_R waiting times, separating the closest pair in $F_{s_1}\times F_{s_2}$, up to rounding error. Thus, if we enumerate the timepoints in F_{s_1} instead starting from the end (so that $m'_j\in F_{s_1}$ is the j'th largest value in F_s, $j\geq 1$), the differences in timepoints $m'_{j_1}\in F_{s_1}$ and $m_{j_2}\in F_{s_2}$, with $s_2>s_1$, can be written on the form.

$$|m'_{j_1}-m_{j_2}|=W_{s_2}+\sum_{k=1}^{s_2-s_1}(W_{R_{s_1+k}}+W_{F_{s_1+k}})+(j_1+j_2-2)\Delta+E_{(s_1,s_2)}, \tag{A.I.66}$$

where $E_{(s_1,s_2)}$ only depends on (s_1,s_2) and has

$$P(E_{(s_1,s_2)}\in(-\Delta,\Delta))=1. \tag{A.I.67}$$

Therefore:

$$\sum_{s_1=1}^{N_b}\sum_{s_2=1}^{N_b}\mathbb{1}(s_1\neq s_2)\sum_{m_{j_1}\in F_{s_1}}\sum_{m_{j_2}\in F_{s_2}}e^{iv|m_{j_1}-m_{j_2}|} \tag{A.I.68}$$

$$=2\sum_{s_1=1}^{N_b-1}\sum_{s_2=s_1+1}^{N_b}\sum_{m_{j_1}\in F_{s_1}}\sum_{m_{j_2}\in F_{s_2}}e^{iv|m_{j_1}-m_{j_2}|} \tag{A.I.69}$$

$$=2\sum_{s_1=1}^{N_b-1}\sum_{s_2=s_1+1}^{N_b}e^{ivW_{s_2}}e^{iv\sum_{k=1}^{s_2-s_1}(W_{R_{s_1+k}}+W_{F_{s_1+k}})}e^{ivE_{(s_1,s_2)}} \tag{A.I.70}$$

$$\times e^{-iv\Delta 2}\sum_{j_1=1}^{|F_{s_1}|}\sum_{j_2=1}^{|F_{s_2}|}e^{iv(j_1+j_2)\Delta}$$

$$=2\sum_{s_1=1}^{N_b-1}\sum_{s_2=s_1+1}^{N_b}e^{ivW_{s_2}}e^{iv\sum_{k=1}^{s_2-s_1}(W_{R_{s_1+k}}+W_{F_{s_1+k}})}e^{ivE_{(s_1,s_2)}} \tag{A.I.71}$$

$$\times e^{-iv\Delta 2}\frac{(e^{iv\Delta|F_{s_1}|}-1)(e^{iv\Delta|F_{s_2}|}-1)}{(e^{iv\Delta}-1)^2}.$$

At this point, it should be clear that discretization effects again have no impact in the limit. For the sake of completion, we compute also this asymptotic value:

$$\lim_{\Delta\to 0}\frac{\mathbb{E}\left[\sum_{s_1=1}^{N_b}\sum_{s_2=1}^{N_b}\mathbb{1}(s_1\neq s_2)\sum_{m_{j_1}\in F_{s_1}}\sum_{m_{j_2}\in F_{s_2}}e^{iv|m_{j_1}-m_{j_2}|}\right]}{\mathbb{E}[G(G-1)]} \tag{A.I.72}$$

$$=\frac{-\mathbb{E}\left[2\sum_{s_1=1}^{N_b-1}\sum_{s_2=s_1+1}^{N_b}e^{ivW_{s_2}}e^{iv\sum_{k=1}^{s_2-s_1}(W_{R_{s_1+k}}+W_{F_{s_1+k}})}(e^{ivW_{F_{s_1}}}-1)(e^{ivW_{F_{s_2}}}-1)\right]}{v^2(\mathbb{E}[N_b]\mathbb{E}\left[W_F^2\right]+\mathbb{E}[N_b(N_b-1)]\mathbb{E}[W_F]^2)} \tag{A.I.73}$$

$$=\frac{2\left(\frac{\phi_F(v)-1}{\phi_{(F+R)}(v)-1}\right)^2\phi_R(v)\left(1+\mathbb{E}[N_b](\phi_{(F+R)}(v)-1)-\mathbb{E}\left[\phi_{(F+R)}(v)^{N_b}\right]\right)}{v^2(\mathbb{E}[N_b]\mathbb{E}\left[W_F^2\right]+\mathbb{E}[N_b(N_b-1)]\mathbb{E}[W_F]^2)}. \tag{A.I.74}$$

Thus, replacing again all discretization errors with the midpoints of their domains ($E_s^F=\frac{1}{2}, E_{s_1,s_2}=0$), we get an asymptotically exact approximation:

$$\frac{\mathbb{E}\left[\sum_{s_1=1}^{N_b}\sum_{s_2=1}^{N_b}\mathbb{1}(s_1\neq s_2)\sum_{m_{j_1}\in F_{s_1}}\sum_{m_{j_2}\in F_{s_2}}e^{iv|m_{j_1}-m_{j_2}|}\right]}{\mathbb{E}[G(G-1)]} \tag{A.I.75}$$

$$\approx\frac{2e^{-iv\Delta 2}\left(\frac{\phi_F(v)e^{iv\Delta\frac{1}{2}}-1}{\phi_{(F+R)}(v)-1}\right)^2\phi_R(v)\left(\mathbb{E}\left[\phi_{(F+R)}(v)^{N_b}\right]-1-\mathbb{E}[N_b](\phi_{(F+R)}(v)-1)\right)}{(e^{-iv\Delta}-1)^2\left(\mathbb{E}\left[N_b^2\right]\left(\frac{\mathbb{E}[W_F]}{\Delta}+\frac{1}{2}\right)^2+\mathbb{E}[N_b]\left[\frac{\mathbb{E}\left[W_F^2\right]-\mathbb{E}[W_F]^2}{\Delta^2}-\frac{\mathbb{E}[W_F]}{\Delta}-\frac{1}{2}\right]\right)}, \tag{A.I.76}$$

which is $\frac{B(v)C(v)}{D}$.

Approximate n_c

We wish to compute

$$n_c = \frac{\mathbb{E}\left[G^2\right]}{\mathbb{E}[G]} - 1. \tag{A.I.77}$$

Instead of approximating the moments directly, we first approximate the distribution of G, from which the moments can be obtained. We can write somewhat loosely

$$G = \sum_{s=1}^{N_b} \#(\text{frames hit by the s'th F-signal}) - \sum_{s=1}^{N_b-1} \mathbb{1}(\text{F-signals s and s+1 share a frame}), \tag{A.I.78}$$

where by "sharing"we mean that the continuous time signals emitted from the 2 F-state visits hit the same frame. Now, computing the distribution of G from this representation is made intractable due to the dependence and complicated behavior in the summands caused by disretization to the fixed grid $\Delta\mathbb{Z}$. Instead, we replace the summands with their mean under disretization to grids $\Delta\mathbb{Z} + U$, where $U \sim Uni(0, \Delta)$. Write $\mathbb{E}_U[\cdot]$ for this mean, and let $\lfloor a \rfloor$ and $\{a\}$ denote the integer and fractional parts, respectively, of a number a. Write T_s^I and T_s^O for the entrance and exit times, respectively, for the s'th F-state visit, and D_s for the distance from T_s^I to the nearest gridpoint larger than T_s^I. Then, we obtain for any s

$$\begin{aligned}
&\mathbb{E}_U[\#(\text{frames hit by the s'th F-signal})] && \text{(A.I.79)}\\
&= \lfloor W_{F_s}\Delta^{-1} \rfloor + \mathbb{E}_U\left[2\mathbb{1}(D_s < \{W_{F_s}\Delta^{-1}\}) + \mathbb{1}(D_s > \{W_{F_s}\Delta^{-1}\})\right] && \text{(A.I.80)}\\
&= \lfloor W_{F_s}\Delta^{-1} \rfloor + 2\{W_{F_s}\Delta^{-1}\} + (1 - \{W_{F_s}\Delta^{-1}\}) && \text{(A.I.81)}\\
&= W_{F_s}\Delta^{-1} + 1. && \text{(A.I.82)}
\end{aligned}$$

Now, for the second sum, we get

$$\begin{aligned}
&\mathbb{E}_U[\mathbb{1}(\text{F-signals s and s+1 share a frame})] && \text{(A.I.83)}\\
&= 1 - \mathbb{E}_U\left[\mathbb{1}(\text{there is a gridpoint between } T_s^O \text{ and } T_{s+1}^I)\right] && \text{(A.I.84)}\\
&= 1 - (W_{R_s}\Delta^{-1}\mathbb{1}(W_{R_s} \le \Delta) + \mathbb{1}(W_{R_s} > \Delta)) && \text{(A.I.85)}\\
&= \mathbb{1}(W_{R_s}\Delta^{-1} \le 1)(1 - W_{R_s}\Delta^{-1}) && \text{(A.I.86)}
\end{aligned}$$

, and our approximation for G is thus

$$G \approx \sum_{s=1}^{N_b} \frac{W_{F_s}}{\Delta} + 1 - \sum_{s=1}^{N_b-1} \mathbb{1}(\frac{W_{R_s}}{\Delta} \le 1)(1 - \frac{W_{R_s}}{\Delta}), \tag{A.I.87}$$

from which we obtain

$$\mathbb{E}[G] \approx \mathbb{E}[N_b]\left(\frac{\mathbb{E}[W_F]}{\Delta} + 1\right) - \mathbb{E}[N_b - 1]\,\mu_R^1, \tag{A.I.88}$$

where $\mu_R^1 = \int_0^1 (1-x) dP_{\frac{W_R}{\Delta}}(x)$, and

$$\begin{aligned}\mathbb{E}\left[G^2\right] \approx \mathbb{E}\left[N_b^2\right]\left(\frac{\mathbb{E}[W_F]}{\Delta} + 1\right)^2 + \mathbb{E}[N_b]\frac{\mathbb{E}\left[W_F^2\right] - \mathbb{E}[W_F]^2}{\Delta^2} \\ + \mathbb{E}\left[(N_b-1)^2\right](\mu_R^1)^2 + \mathbb{E}[N_b - 1]\left(\mu_R^2 - (\mu_R^1)^2\right) \\ - 2\mathbb{E}[N_b(N_b-1)]\left(\frac{\mathbb{E}[W_F]}{\Delta} + 1\right)\mu_R^1,\end{aligned} \tag{A.I.89}$$

with $\mu_R^2 = \int_0^1 (1-x)^2 dP_{\frac{W_R}{\Delta}}(x)$.

If we write $n_c(\Delta)$ for the approximation of n_c given a framerate of Δ^{-1}, we have that $n_c(\Delta)$ is asymptotically exact in the sense that, after appropriate normalization, we have

$$\lim_{\Delta\to 0} \Delta n_c(\Delta) = \lim_{\Delta \to 0} \Delta n_c, \tag{A.I.90}$$

where this asymptotic value is given as

$$\lim_{\Delta\to 0} \Delta n_c = \frac{\mathbb{E}[N_b]\mathbb{E}\left[W_F^2\right] + \mathbb{E}[N_b(N_b-1)]\mathbb{E}[W_F]^2}{\mathbb{E}[N_b]\mathbb{E}[W_F]}. \tag{A.I.91}$$

Approximate $\gamma_2(f_+)$

By definition, we have

$$\gamma_2(f_+) = \frac{\mathbb{E}\left[\sum_{k=1}^G \sum_{j=1}^{G'} f_+(m_k, m_j')\right]}{\mathbb{E}[G]^2} = \frac{\mathbb{E}\left[\sum_{k=1}^G \sum_{j=1}^{G'} m_k + m_j'\right]}{\mathbb{E}[G]^2}, \tag{A.I.92}$$

where we again drop the drop the heavier time point notation, such that e.g. m_k is arrival time k in a typical cluster, and m_j' is arrival time j in an independent copy of the typical cluster. Clearly, then,

$$\frac{1}{2}\gamma_2(f_+) = \frac{\mathbb{E}\left[\sum_{k=1}^G m_k\right]}{\mathbb{E}[G]}. \tag{A.I.93}$$

Now, write T_s^I for the (continuous) entrance time to the s'th F-state visit. Then the first observed timepoint in F_s can be written as $T_s^I + E_s$, where E_s is a discretization error with $P(0 \leq E_s \leq \Delta) = 1$. Note further, that

$$T_s^I = W_I + \sum_{i=1}^{s-1}(W_{F_i} + W_{R_i}), \tag{A.I.94}$$

and we arrive at the expression

$$\frac{1}{2}\gamma_2(f_+) = \frac{\mathbb{E}\left[\sum_{s=1}^{N_b} |F_s|(T_s^I + E_s) + \sum_{k=1}^{|F_s|} k\Delta\right]}{\mathbb{E}[G]} \tag{A.I.95}$$

$$= \frac{\mathbb{E}\left[\sum_{s=1}^{N_b} |F_s|(T_s^I + E_s)\right]}{\mathbb{E}[G]} + \frac{\Delta\mathbb{E}\left[\sum_{s=1}^{N_b} |F_s|(|F_s|+1)\right]}{2\mathbb{E}[G]}. \tag{A.I.96}$$

Now, setting everywhere $|F_s| = \frac{W_{F_s}}{\Delta} + \frac{1}{2}$ as in Supplement C.1, and similarly setting all $E_s = \Delta\frac{1}{2}$, we get

$$\frac{\mathbb{E}\left[\sum_{s=1}^{N_b}\sum_{k=1}^{|F_s|} k\Delta\right]}{\mathbb{E}[G]} = \frac{\mathbb{E}[N_b](\frac{\mathbb{E}[W_F^2]}{2\Delta} + \mathbb{E}[W_F] + \frac{3\Delta}{8})}{\mathbb{E}[G]}, \tag{A.I.97}$$

and

$$\frac{\mathbb{E}\left[\sum_{s=1}^{N_b}|F_s|(T_s^I + E_s)\right]}{\mathbb{E}[G]} \tag{A.I.98}$$

$$= \mathbb{E}[W_I] + \frac{\mathbb{E}\left[\sum_{s=1}^{N_b}(\frac{W_{F_s}}{\Delta} + \frac{1}{2})(\sum_{i=1}^{s-1}(W_{F_i} + W_{R_i}) + \Delta\frac{1}{2})\right]}{\mathbb{E}[G]} \tag{A.I.99}$$

$$= \mathbb{E}[W_I] + \frac{(\frac{\mathbb{E}[W_F]}{\Delta} + \frac{1}{2})(\frac{1}{2}\mathbb{E}[N_b(N_b-1)](\mathbb{E}[W_F] + \mathbb{E}[W_R]) + \mathbb{E}[N_b]\Delta\frac{1}{2})}{\mathbb{E}[G]}, \tag{A.I.100}$$

so that using $\mathbb{E}[G] \approx \mathbb{E}[N_b]\left(\frac{\mathbb{E}[W_F]}{\Delta} + \frac{1}{2}\right)$ yields the approximation. Again, the approximation is asymptotically exact, with limiting value

$$\lim_{\Delta\to 0}\frac{1}{2}\gamma_2(f_+) = \mathbb{E}[W_I] + \frac{\mathbb{E}[W_F](\frac{1}{2}\mathbb{E}[N_b(N_b-1)](\mathbb{E}[W_F] + \mathbb{E}[W_R])}{\mathbb{E}[N_b]\mathbb{E}[W_F]} + \frac{\mathbb{E}\left[W_F^2\right]}{2\mathbb{E}[W_F]}. \tag{A.I.101}$$

Supplement D: Use on general general protein samples

In this section we show that we can use the same estimation procedures from the main text on samples with general distribution for ${}_{\downarrow}X$, and still expect meaningful estimates. We assume here that the spatial dimension is 2, but the same arguments can be made in arbitrary dimension with minor changes.

Assume that the IBCpp O is observed with N points in $W \times [0,b]$. Standard estimators of $\gamma_2^O(f)k_O^f$ and $g_{{}_{\downarrow}O}$, if O were motion-invariant, are given as

$$\hat{\gamma}_2^O(f)\hat{k}_O^f(r) = \frac{\sum_{i\neq j} f(t_{o_i}, t_{o_j})\kappa(\|o_i - o_j\| - r)w(o_i, o_j)\mathbb{1}_W(o_i, o_j)}{\sum_{i\neq j}\kappa(\|o_i - o_j\| - r)w(o_i, o_j)\mathbb{1}_W(o_i, o_j)}, \tag{A.I.102}$$

$$\hat{g}_{{}_{\downarrow}O}(r) = c(r)\sum_{i\neq j}\kappa(\|o_i - o_j\| - r)w(o_i, o_j)\mathbb{1}_W(o_i, o_j). \tag{A.I.103}$$

Here, $c(r) = (2\pi r)^{-1}N^{-2}|W|$, κ is a smoothing kernel, $w(x,y)$ are edge correction weights, and $\mathbb{1}_W(o_i, o_j)$ is the indicator that both o_i and o_j are in the set W, see e.g. [10, p. 308, 393]. To avoid most complications from edge effects we imagine in the following that ${}_{\downarrow}X$ is finite, and the observation window W is chosen large enough that every point in Z is observed with probability ≈ 1. Further, we set $w = 1$ for all pairs. Although these simplifying assumptions can often be satisfied in practice, as ${}_{\downarrow}X$ is naturally finite and typically entirely observable, smaller ROIs are more convenient to work with, and will then be subject to edge effects. Fortunately, for the size of a typical ROI in SMLM, edge effects should be negligible.

Choosing the same kernel for both estimators above, an estimator of S_O^f is

$$\hat{S}_O^f(r) = \hat{g}_{\downarrow O}(r)\hat{\gamma}_2^O(f)\hat{k}_O^f(r) = c(r)\sum_{i\neq j} f(t_{o_i}, t_{o_j})\kappa(\|o_i - o_j\| - r)\mathbb{1}_W(o_i, o_j). \tag{A.I.104}$$

Rather than computing the mean of $\hat{S}_O^f$ directly, we consider the mean of $N^2\hat{S}_O^f(r)$, which yields slightly more elegant computations. By splitting the summation according to the cluster and process relationships of pairs, using the symmetry of f, and writing $\tilde{c}(r) = N^2 c(r)$, we obtain

$$\begin{aligned}
&\mathbb{E}\left[N^2\hat{S}_O^f(r)\right] \qquad\qquad (\text{A.I.105})\\
&= \mathbb{E}\left[\tilde{c}(r)\sum_{x\in_\downarrow X}\overset{\neq}{\sum_{(y_1,t_{y_1}),(y_2,t_{y_2})\in Y_x^2}} f(t_{y_1}, t_{y_2})\kappa(\|y_1 - y_2\| - r)\mathbb{1}_W(y_1, y_2)\right]\\
&+ \mathbb{E}\left[\tilde{c}(r)\overset{\neq}{\sum_{(x_1,x_2)\in_\downarrow X^2}}\sum_{(y_1,t_{y_1})\in Y_{x_1}}\sum_{(y_2,t_{y_2})\in Y_{x_2}} f(t_{y_1}, t_{y_2})\kappa(\|y_1 - y_2\| - r)\mathbb{1}_W(y_1, y_2)\right]\\
&+ 2\mathbb{E}\left[\tilde{c}(r)\sum_{x\in_\downarrow X}\sum_{(y,t_y)\in Y_x}\sum_{(e,t_e)\in E} f(t_y, t_e)\kappa(\|y - e\| - r)\mathbb{1}_W(e, y)\right]\\
&+ \mathbb{E}\left[\tilde{c}(r)\overset{\neq}{\sum_{(e_1,t_{e_1}),(e_2,t_{e_2})\in E^2}} f(t_{e_1}, t_{e_2})\kappa(\|e_1 - e_2\| - r)\mathbb{1}_W(e_1, e_2)\right],
\end{aligned}$$

Using the spatio-temporal dependence structure of our model, we average out the clusters to arrive at

$$\begin{aligned}
\mathbb{E}\left[N^2\hat{S}_O^f(r)\right] = \gamma_1(f)n_c\mathbb{E}[G]\mathbb{E}\left[\tilde{c}(r)\sum_{x\in_\downarrow X}(h_\epsilon * h_\epsilon)_x^\kappa(r)\right] \qquad (\text{A.I.106})\\
+ \gamma_2(f)\mathbb{E}[G]^2\mathbb{E}\left[\tilde{c}(r)\overset{\neq}{\sum_{(x_1,x_2)\in_\downarrow X^2}}(h_\epsilon * h_\epsilon)_{x_1,x_2}^\kappa(r)\right]\\
+ 2\gamma_2^{EZ}(f)\mathbb{E}[G]\lambda_{\downarrow E}\mathbb{E}\left[\tilde{c}(r)\sum_{x\in_\downarrow X^2}(h_\epsilon * h_e)_x^\kappa(r)\right]\\
+ \gamma_2^E(f)\lambda_{\downarrow E}^2\mathbb{E}[\tilde{c}(r)(h_e * h_e)^\kappa(r)],
\end{aligned}$$

where

$$(h_\epsilon * h_\epsilon)_x^\kappa(r) = \int \kappa(\|t_1 - t_2\| - r)h_\epsilon(t_1)h_\epsilon(t_2)\mathbb{1}_W(x + t_1, x + t_2)dt_1dt_2, \tag{A.I.107}$$

$$(h_\epsilon * h_\epsilon)_{x_1,x_2}^\kappa(r) = \int \kappa(\|t_1 + x_1 - t_2 - x_2\| - r)h_\epsilon(t_1)h_\epsilon(t_2)\mathbb{1}_W(x_1 + t_1, x_2 + t_2)dt_1dt_2, \tag{A.I.108}$$

$$(h_\epsilon * h_e)_x^\kappa(r) = \int \kappa(\|x + t_1 - t_2\| - r)h_\epsilon(t_1)\mathbb{1}_W(x + t_1, t_2)dt_1dt_2, \tag{A.I.109}$$

$$(h_e * h_e)^\kappa(r) = \int \kappa(\|t_1 - t_2\| - r)\mathbb{1}_W(t_1, t_2)dt_1dt_2. \tag{A.I.110}$$

By considering what happens for $f = 1$ (in which case $\gamma_1(f) = \gamma_2(f) = \gamma_2^E(f) = \gamma_2^{EZ}(f) = 1$), we see that we can rewrite the above as

$$\begin{aligned}\mathbb{E}\left[N^2 \hat{S}_O^f(r)\right] &= (\gamma_1(f) - \gamma_2(f)) n_c \mathbb{E}[G] \mathbb{E}\left[\tilde{c}(r) \sum_{x \in_\downarrow X} (h_\epsilon * h_\epsilon)_x^\kappa(r)\right] \\ &+ \gamma_2(f) \mathbb{E}\left[N^2 \hat{g}_{\downarrow O}(r)\right] \\ &+ 2(\gamma_2^{EZ}(f) - \gamma_2(f)) \mathbb{E}[G] \lambda_{\downarrow E} \mathbb{E}\left[\tilde{c}(r) \sum_{x \in_\downarrow X} (h_\epsilon * h_e)_x^\kappa(r)\right] \\ &+ (\gamma_2^E(f) - \gamma_2(f)) \lambda_{\downarrow E}^2 \mathbb{E}[\tilde{c}(r)(h_e * h_e)^\kappa(r)],\end{aligned} \tag{A.I.111}$$

and we already have a very similar expression to the motion-invariant case. The obstacle to further exact computations come from edge and kernel biases. For the pure cluster term, since we assumed that Z is contained in W with large probability, we have

$$\begin{aligned}(h_\epsilon * h_\epsilon)_x^\kappa(r) &\approx \int \kappa(\|t_1 - t_2\| - r) h_\epsilon(t_1) h_\epsilon(t_2) dt_1 dt_2 && \text{(A.I.112)} \\ &= \int \kappa(\|t_1\| - r) h_\epsilon(t_1 + t_2) dt_1 h_\epsilon(t_2) dt_2 && \text{(A.I.113)} \\ &= \int l\kappa(l - r) h_\epsilon(l\,[cos(\theta), sin(\theta)] + t_2) dl d\theta h_\epsilon(t_2) dt_2 && \text{(A.I.114)} \\ &= 2\pi \int l\kappa(l - r)(h_\epsilon * h_\epsilon)(l) dl, && \text{(A.I.115)}\end{aligned}$$

obtained by polar integration, which is a kernel-smoothed version of the cluster autoconvolution. In particular, for small kernel bandwidths, we have

$$\begin{aligned}\mathbb{E}[G] \mathbb{E}\left[\tilde{c}(r) \sum_{x \in_\downarrow X} (h_\epsilon * h_\epsilon)_x^\kappa(r)\right] &= \mathbb{E}[G](2\pi r)^{-1} |W| \Lambda_X(W) (h_\epsilon * h_\epsilon)_x^\kappa(r) && \text{(A.I.116)} \\ &\approx |W| \Lambda_Z(W) (h_\epsilon * h_\epsilon)(r), && \text{(A.I.117)}\end{aligned}$$

since $\Lambda_Z(W) \approx \Lambda_X(W)\mathbb{E}[G]$ as Z is contained in W with large probability. Using the same tricks for the mixed term, we have

$$\begin{aligned}(h_\epsilon * h_e)_x^\kappa(r) &\approx \int \kappa(\|x + t_1 - t_2\| - r) h_\epsilon(t_1) dt_1 dt_2 && \text{(A.I.118)} \\ &= \int \kappa(\|t_2\| - r) dt_2 \int h_\epsilon(t_1) dt_1, && \text{(A.I.119)}\end{aligned}$$

so that, for small kernel bandwidths we have

$$\mathbb{E}[G] \mathbb{E}\left[\tilde{c}(r) \sum_{x \in_\downarrow X} (h_\epsilon * h_e)_x^\kappa(r)\right] \approx |W| \Lambda_Z(W). \tag{A.I.120}$$

Finally, for the pure noise term, note that

$$\lambda_{\downarrow E}^2 \mathbb{E}[\tilde{c}(r)(h_e * h_e)_x^{w,\kappa}(r)] = \mathbb{E}\left[|E \cap W|^2 \hat{g}_{\downarrow E}(r)\right], \tag{A.I.121}$$

where $\hat{g}_{\downarrow E}(r)$ is the estimator of the pair correlation function of a stationary Poisson process, so that we can reasonably expect

$$\lambda_{\downarrow E}^2 \mathbb{E}\left[\tilde{c}(r)(h_e * h_e)_x^{w,\kappa}(r)\right] \approx \mathbb{E}\Big[|E \cap W|^2\Big]. \tag{A.I.122}$$

Thus, assuming the kernel bandwidth is not too large, we obtain

$$\begin{aligned}\mathbb{E}\Big[N^2 \hat{S}_O^f(r)\Big] \approx\ & (\gamma_1(f) - \gamma_2(f)) n_c |W| \Lambda_Z(W)(h_\epsilon * h_\epsilon)(r) \\ & + \gamma_2(f)\mathbb{E}\Big[N^2 \hat{g}_{\downarrow O}(r)\Big] \\ & + 2(\gamma_2^{EZ}(f) - \gamma_2(f))\Lambda_E(W)\Lambda_Z(W) \\ & + (\gamma_2^E(f) - \gamma_2(f))\mathbb{E}\Big[|E \cap W|^2\Big],\end{aligned} \tag{A.I.123}$$

Using simple Taylor expansions for the mean values, we have

$$\begin{aligned}\mathbb{E}\Big[\hat{S}_O^f(r)\Big] \approx\ & (\gamma_1(f) - \gamma_2(f)) n_c \frac{\eta(W)}{\Lambda_O(W)|W|^{-1}}(h_\epsilon * h_\epsilon)(r) \\ & + \gamma_2(f)\mathbb{E}\Big[\hat{g}_{\downarrow O}(r)\Big] \\ & + 2(\gamma_2^{EZ}(f) - \gamma_2(f))\eta(W)(1 - \eta(W)) \\ & + (\gamma_2^E(f) - \gamma_2(f))(1 - \eta(W))^2,\end{aligned} \tag{A.I.124}$$

or

$$\mathbb{E}\Big[\hat{S}_O^f(r)\Big] \approx (\gamma_1(f) - \gamma_2(f)) \frac{n_c \eta(W)}{\Lambda_O(W)|W|^{-1}}(h_\epsilon * h_\epsilon)(r) + \gamma_2(f)(\mathbb{E}\Big[\hat{g}_{\downarrow O}(r)\Big] - 1) + \gamma_2^O(f, W), \tag{A.I.125}$$

where

$$\eta(W) = \frac{\Lambda_Z(W)}{\Lambda_O(W)}, \tag{A.I.126}$$

$$\gamma_2^O(f, W) = \eta(W)^2 \gamma_2(f) + (1 - \eta(W))^2 \gamma_2^E(f) + 2\eta(W)(1 - \eta(W))\gamma_2^{EZ}(f). \tag{A.I.127}$$

Thus, whether X is motion-invariant or not, the mean of the involved summary statistics take approximately the same shape. Note that, since a general distribution for $_\downarrow X$ does not change the spatio-temporal dependence structures, and since all intensity estimation is done for the entire ROI (e.g. the local intensity of O is not needed, only $\Lambda_O(W)$), each term above is naturally estimated by the exact same procedures we developed for the motion-invariant case - the only difference is in interpretation, which must now be conditional on W.

References

[1] Andersen, I.T., U. Hahn, E.C. Arnspang, L.N. Nejsum and E.B.V. Jensen (2018). Double Cox cluster processes — with applications to photoactivated localization microscopy. *Spatial Statistics* 27, 58–73. DOI: 10.1016/j.spasta.2018.04.009.

[2] Annibale, P., S. Vanni, M. Scarselli, U. Rothlisberger and A. Radenovic (2011a). Identification of clustering artifacts in photoactivated localization microscopy. *Nature methods* 8(7), 527.

[3] Annibale, P., S. Vanni, M. Scarselli, U. Rothlisberger and A. Radenovic (2011b). Quantitative photo activated localization microscopy: unraveling the effects of photoblinking. *PloS one* 6(7), e22678.

[4] Baddeley, A., E. Rubak and R. Turner (Nov. 2015). *Spatial Point Patterns*. Apple Academic Press Inc. 810 pp.

[5] Betzig, E., G.H. Patterson, R. Sougrat, O.W. Lindwasser, S. Olenych, J.S. Bonifacino, M.W. Davidson, J. Lippincott-Schwartz and H.F. Hess (2006). Imaging intracellular fluorescent proteins at nanometer resolution. *Science* 313(5793), 1642–1645.

[6] Coltharp, C., R.P Kessler and J. Xiao (2012). Accurate construction of photoactivated localization microscopy (PALM) images for quantitative measurements. *PLoS One* 7(12), e51725.

[7] Daley, D.J. and D. Vere-Jones (2007). *An introduction to the theory of point processes: volume II: general theory and structure*. Springer Science & Business Media.

[8] Deschout, H., F.C. Zanacchi, M. Mlodzianoski, A. Diaspro, J. Bewersdorf, S. T. Hess and K. Braeckmans (2014). Precisely and accurately localizing single emitters in fluorescence microscopy. *Nature methods* 11(3), 253.

[9] Fricke, F., J. Beaudouin, R. Eils and M. Heilemann (2015). One, two or three? Probing the stoichiometry of membrane proteins by single-molecule localization microscopy. *Scientific reports* 5, 14072.

[10] Gelfand, A.E., P. Diggle, P. Guttorp and M. Fuentes (2010). *Handbook of spatial statistics*. CRC press.

[11] Griffié, J., T. Pham, C. Sieben, R. Lang, V. Cevher, S. Holden, M. Unser, S. Manley and D. Sage (Mar. 2020). Virtual-SMLM, a virtual environment for real-time interactive SMLM acquisition. DOI: 10.1101/2020.03.05.967893.

[12] Huang, B., M. Bates and X. Zhuang (June 2009). Super-Resolution Fluorescence Microscopy. *Annual Review of Biochemistry* 78(1), 993–1016. DOI: 10.1146/annurev.biochem.77.061906.092014.

[13] Hummer, G., F. Fricke and M. Heilemann (2016). Model-independent counting of molecules in single-molecule localization microscopy. *Molecular biology of the cell* 27(22), 3637–3644.

[14] Hurlimann, W. (2013). Improved FFT approximations of probability functions based on modified quadrature rules. *International Mathematical Forum* 8, 829–840. DOI: 10.12988/imf.2013.13087.

[15] Karathanasis, C., F. Fricke, G. Hummer and M. Heilemann (2017). Molecule counts in localization microscopy with organic fluorophores. *ChemPhysChem* 18(8), 942–948.

[16] Khater, I.M, I.R. Nabi and G. Hamarneh (June 2020). A Review of Super-Resolution Single-Molecule Localization Microscopy Cluster Analysis and

Quantification Methods. *Patterns* 1(3), 100038. DOI: 10.1016/j.patter.2020.100038.

[17] Lee, S.-H., J.Y. Shin, A. Lee and C. Bustamante (Oct. 2012). Counting single photoactivatable fluorescent molecules by photoactivated localization microscopy (PALM). *Proceedings of the National Academy of Sciences* 109(43), 17436–17441. DOI: 10.1073/pnas.1215175109.

[18] Lin, Y., J.J. Long, F. Huang, W.C. Duim, S. Kirschbaum, Y. Zhang, L.K. Schroeder, A.A. Rebane, M.G.M Velasco, A. Virrueta, et al. (2015). Quantifying and optimizing single-molecule switching nanoscopy at high speeds. *PloS one* 10(5), e0128135.

[19] Myllymäki, M., T. Mrkvička, P. Grabarnik, H. Seijo and U. Hahn (Mar. 2017). Global envelope tests for spatial processes. *Journal of the Royal Statistical Society: Series B (Statistical Methodology)* 79(2), 381–404. DOI: 10.1111/rssb.12172.

[20] Ober, R.J., A. Tahmasbi, S. Ram, Z. Lin and E.S. Ward (Jan. 2015). Quantitative Aspects of Single-Molecule Microscopy: Information-theoretic analysis of single-molecule data. *IEEE Signal Processing Magazine* 32(1), 58–69. DOI: 10.1109/msp.2014.2353664.

[21] Ovesny, M., P. Křižek, J. Borkovec, Z. Švindrych and G.M Hagen (2014). ThunderSTORM: a comprehensive ImageJ plug-in for PALM and STORM data analysis and super-resolution imaging. *Bioinformatics* 30(16), 2389–2390.

[22] Patel, L., N. Gustafsson, Y. Lin, R. Ober, R. Henriques, E. Cohen, et al. (2019). A hidden Markov model approach to characterizing the photo-switching behavior of fluorophores. *The Annals of Applied Statistics* 13(3), 1397–1429.

[23] Ries, J. (Aug. 2020). SMAP: a modular super-resolution microscopy analysis platform for SMLM data. *Nature Methods* 17(9), 870–872. DOI: 10.1038/s41592-020-0938-1.

[24] Ripley, B.D. (June 1976). The second-order analysis of stationary point processes. *Journal of Applied Probability* 13(2), 255–266. DOI: 10.2307/3212829.

[25] Rollins, G.C., J.Y. Shin, C. Bustamante and S. Presse (2015). Stochastic approach to the molecular counting problem in superresolution microscopy. *Proceedings of the National Academy of Sciences* 112(2), E110–E118.

[26] Rossboth, B., A.M Arnold, H. Ta, R. Platzer, F. Kellner, J.B. Huppa, M. Brameshuber, F. Baumgart and G.J. Schütz (July 2018). TCRs are randomly distributed on the plasma membrane of resting antigen-experienced T cells. *Nature Immunology* 19(8), 821–827. DOI: 10.1038/s41590-018-0162-7.

[27] Rust, M.J., M. Bates and X. Zhuang (Aug. 2006). Sub-diffraction-limit imaging by stochastic optical reconstruction microscopy (STORM). *Nature Methods* 3(10), 793–796. DOI: 10.1038/nmeth929.

[28] Schnitzbauer, J., M.T. Strauss, T. Schlichthaerle, F. Schueder and R. Jungmann (May 2017). Super-resolution microscopy with DNA-PAINT. *Nature Protocols* 12(6), 1198–1228. DOI: 10.1038/nprot.2017.024.

[29] Sengupta, P., T. Jovanovic-Talisman, D. Skoko, M. Renz, S.L. Veatch and J. Lippincott-Schwartz (2011). Probing protein heterogeneity in the plasma membrane using PALM and pair correlation analysis. *Nature methods* 8(11), 969.

[30] Shivanandan, A., H. Deschout, M. Scarselli and A. Radenovic (2014). Challenges in quantitative single molecule localization microscopy. *FEBS letters* 588(19), 3595–3602.

[31] Shtengel, G. et al. (Feb. 2009). Interferometric fluorescent super-resolution microscopy resolves 3D cellular ultrastructure. *Proceedings of the National Academy of Sciences* 106(9), 3125–3130. DOI: 10.1073/pnas.0813131106.

[32] Small, A. and S. Stahlheber (2014). Fluorophore localization algorithms for super-resolution microscopy. *Nature methods* 11(3), 267.

[33] Staudt, T., T. Aspelmeier, O. Laitenberger, C. Geisler, A. Egner, A. Munk, et al. (2020). Statistical Molecule Counting in Super-Resolution Fluorescence Microscopy: Towards Quantitative Nanoscopy. *Statistical Science* 35(1), 92–111.

[34] Stoyan, D. (1984). On correlations of marked point processes. *Mathematische Nachrichten* 116(1), 197–207.

[35] Thevathasan, J.V. et al. (2019a). *Nuclear pores as versatile reference standards for quantitative superresolution microscopy*. https://www.ebi.ac.uk/biostudies/BioImages/studies/S-BIAD8.

[36] Thevathasan, J.V. et al. (Sept. 2019b). Nuclear pores as versatile reference standards for quantitative superresolution microscopy. *Nature Methods* 16(10), 1045–1053. DOI: 10.1038/s41592-019-0574-9.

[37] Veatch, S.L., B.B. Machta, S.A. Shelby, E.N. Chiang, D.A. Holowka and B.A. Baird (Feb. 2012). Correlation Functions Quantify Super-Resolution Images and Estimate Apparent Clustering Due to Over-Counting. *PLoS ONE* 7(2). Ed. by J. Rao, e31457. DOI: 10.1371/journal.pone.0031457.

[38] Williamson, D.J., D.M Owen, J. Rossy, A. Magenau, M. Wehrmann, J.J. Gooding and K. Gaus (June 2011). Pre-existing clusters of the adaptor Lat do not participate in early T cell signaling events. *Nature Immunology* 12(7), 655–662. DOI: 10.1038/ni.2049.

[39] Yamanaka, M., N.I. Smith and K. Fujita (2014). Introduction to super-resolution microscopy. *Microscopy* 63(3), 177–192.

[40] Zhang, B., J. Zerubia and J.-C. Olivo-Marin (2007). Gaussian approximations of fluorescence microscope point-spread function models. *Applied optics* 46(10), 1819–1829.

PAPER B

Correction of multiple-blinking artefacts in photoactivated localisation microscopy

Louis G. Jensen, Tjun Yee Hoh, David J. Williamson, Juliette Griffié, Daniel Sage, Patrick Rubin-Delanchy, Dylan M. Owen

Under revision for *Nature Methods*.

Abstract

Photoactivated localisation microscopy (PALM) produces an array of localisation coordinates by means of photoactivatable fluorescent proteins. However, observations are subject to fluorophore multiple-blinking and each protein is included in the dataset an unknown number of times at different positions, due to localisation error. This causes artificial clustering to be observed in the data. We present a workflow using calibration-free estimation of blinking dynamics and model-based clustering, to produce a corrected set of localisation coordinates now representing the true underlying fluorophore locations with enhanced localisation precision. These can be reliably tested for spatial randomness or analysed by other clustering approaches, and previously inestimable descriptors such as the absolute number of fluorophores per cluster are now quantifiable, which we validate with simulated data. Using experimental data, we confirm that the adaptor protein, LAT, is clustered at the T cell immunological synapse, with its nanoscale clustering properties depending on location and intracellular phosphorylatable tyrosine residues.

B.1 Introduction

Single molecule localisation microscopy (SMLM) methods, such as PALM, circumvent the diffraction limit of light by separating fluorophore detections in time through stochastic activation and photobleaching, and then localizing the resulting sparse distribution of point spread functions[7]. The resulting point-pattern is a purported realisation of the underlying ground truth positions of the fluorophores, but is corrupted by a number of artefacts resulting from the photophysical behaviour of the probes as well as the imaging and localisation steps. Most problematic is the multiple appearance (multiple-blinking) problem where fluorophores undergo multiple on-off cycles before permanently bleaching, combined with the discretization effects that result from observing fluorescent signals on discrete camera frames[1]. The multiple-blinking problem results in data sets that are artificially clustered and overly populated (Figure B.1 a). As such, quantitative cluster analysis of SMLM data, in particular testing for spatial randomness of the underlying fluorophores, remains a challenge.

The most commonly employed method for correction of the multiple-blinking problem is to merge events that appear close in space and time[2, 3, 16]. Such methods require a means of determining the best spatial and temporal thresholds for merging. This determination typically relies on heuristic methods, since the blinking behavior of the fluorescent probes is often unknown, and can vary between experiments. Apart from the challenges involved in determining optimal thresholds, these methods have variable performance, depending on the underlying protein organization and blinking characteristics. Instead of attempting to produce a corrected version of the data which can then be used for any subsequent analysis, other approaches have looked to correct specific spatial statistics to account for multiple-blinking. For example, it is possible to estimate a multiple-blink corrected pair correlation curve[28, 26]. However this cannot then be used to find a cluster map.

In this work, we present a new method for correction of multiple-blinking artefacts in PALM data, which estimates, directly from the sample data set, the parameters of a realistic model of fluorescent protein photophysics [15]. Cluster analysis of the spatio-temporal (x, y, t, σ) data set then allows computation of the marginal likelihood of any given blink-merge proposal, under a full generative model for the data. We select the most likely of several proposals generated using a customised hierarchical clustering algorithm. Finally, each blinking cluster is consolidated into a single position, now free from multiple-blinking and with improved localisation precision. The overall effect is to convert the set of raw (x, y, t, σ) localisation data into a new set, (x, y, σ), with enhanced resolution.

We validate the method on simulated PALM data, varying both the ground-truth organization (regular, random, clustered) and photophysical properties of the fluorescent proteins (light and heavy multiple-blinking). In each case, we compare to the state-of-the-art method of dark time thresholding (DTT). Our method allows for testing the completely spatially random (CSR) hypothesis at the correct significance level, whereas the thresholding method fails to do so, and also outperforms the state-of-art in every other metric (including ground truth recovery and extracted cluster properties). PALM is increasingly used in the biological sciences and owing to the properties of commonly used total internal reflection fluorescence (TIRF) illu-

mination, the distributions of membrane proteins have been especially well studied. Despite this, because of artificial clustering resulting from multiple-blinking, the question of whether membrane proteins are randomly distributed or not has become increasingly contentious[23]. Using our validated method combined with subsequent testing of the corrected protein locations, we show that the adaptor protein Linker for Activation of T cells (LAT) is clustered in the plasma membrane of CD4+ Helper T cell lines after the formation of an artificial immunological synapse[29, 17] against an activating, antibody-coated surface. However, subsequent Bayesian cluster analysis[25, 14] shows the clustering properties to be dependent on its macro-scale location within the synapse and on the presence of intracellular phosphorylatable tyrosine residues which mediate protein binding. We now propose that PALM, combined with the method we present here, can be used to test for spatial randomness in other membrane protein species.

B.2 Results

B.2.1 Description of the algorithm

We work with the space-time localisations and uncertainties that result from localisation software (here ThunderSTORM [18]) that is run on the raw microscope data. We apply drift correction, but otherwise no pre-processing is used. The data points are then modeled as a collection of independent and identically distributed fluorophore blinking clusters, with times following a realistic 4-state model[11, 8], discretized by the camera frames. The spatial locations for each cluster are independently drawn from a circular Gaussian distribution of fixed centre (the true molecule position) and variable but known standard deviation (the localisation uncertainty). The centres are given a uniform prior over the region of interest (ROI).

We refer to our algorithm as model-based correction (MBC), and a schematic of its workflow is shown in Figure B.1 b. We first estimate the temporal rates governing the switching behaviour of fluorescent proteins under the 4-state model [15], and the fraction of background noise points. This is done directly using the experimental data, requiring no additional calibration experiments. A recently developed mathematical technique extracts a component from the empirical mark and pair correlation functions which depends only on the spatio-temporal dynamics of the multiple-blinking process, and not the underlying protein distribution. The parameters of the 4-state model drive the theoretical shape of this component, and so they can be optimised to best fit the empirical version [15]. The rate-estimates allow computation of the likelihood of a sequence of timepoints purported to correspond to one multiple-blinking fluorescent protein, and further yields an estimate on the total number, N, of proteins and noise points in the ROI. Using a custom agglomerative hierarchical clustering (HC) algorithm[9], we split the data in the ROI into partitions with N categories. HC takes as input a dissimilarity matrix and a linkage criterion. The dissimilarity matrix determines the distances between pairs of points, and the linkage criterion determines the way to generalise this distance to pairs of clusters. To favour groups likely to correspond to multiple-blinking clusters, we first scale the temporal dimension by a time-dilation hyperparameter, S, and then compute the sum of Euclidean distances in space and in time. For linkage, we choose Ward's Minimum Variance

Method[9], which is well-suited for Gaussian clusters, and consistently resulted in the most likely partitions across all tested linkage criteria. By varying S, we obtain a large sequence of blinking cluster proposals, and evaluate the marginal likelihood of each using a uniform prior on the partitions. Finally, using the best found partition and the localisation uncertainties, we optimally merge the clusters down to their estimated centres, using inverse-variance weighted averages, and update the uncertainty associated with that centre.

B.2.2 PALM data simulation setup

For a given set of protein positions, corresponding PALM data were generated as follows. We simulated fluorescent protein time traces according to the 4-state switching model (see Figure B.1 b), and the continuous signals were discretised to emulate a camera operating at 25 frames per second (40 ms integration time). This was done for 2 different sets of rates (given in Table B.1), with the light blinking resulting in 5.36 appearances per protein on average, and the heavy blinking resulting in 14.94 appearances. For each of these appearances, the observed spatial coordinates were simulated by adding Gaussian localisation noise to the ground-truth position of the associated fluorescent protein, with standard deviation following a Gamma distribution with mean 30 nm and standard deviation 13.4 nm, emulating the localisation uncertainties that can be observed in real PALM data [29]. Each simulated ROI was corrected using MBC and compared to correction using DTT (Figure B.2 a). For DTT, points were considered to have come from the same fluorophore if they were separated by at most 4 times the mean localisation uncertainty in space, and were no further than T apart in time, where the optimal T was determined for each ROI using the method of Annibale et al [3].

B.2.3 Testing for complete spatial randomness

We first evaluate our algorithm for testing for complete spatial randomness of the underlying ground-truth proteins. In each run (n = 30 per condition), 500 proteins were placed at random in a noiseless 3000 nm x 3000 nm ROI. For each ROI, we compute the function L(r)-r (Figure B.2 b), where L is Besag's L function[10], testing its maximum (Figure B.2 c) under a CSR null hypothesis. The standard DTT correction method was unable to recover the ground-truth functions and resulted in rejection of the CSR null hypothesis in 24 and 30 out of the 30 regions, for light and heavy blinking respectively. On the other hand, MBC resulted in the CSR null hypothesis being rejected for 2 and 4 of the regions for light and heavy blinking respectively. These numbers are within the expected range at a 5% confidence level. Thus, we were able to reliably test the CSR hypothesis using MBC, but not using DTT. The estimated total number of fluorescent proteins in each ROI is shown in Figure B.2 d. Under CSR, DTT tends to overestimate the number of proteins in the ROI whereas MBC closely recovers the ground truth.

B.2.4 Cluster analysis

In this experiment, we demonstrate that a clustering algorithm can extract correct cluster descriptions from underlying clustered ground truth protein distributions

when coupled with MBC, and we compare performance with DTT. We simulated data from 2 clustered protein distributions (n = 30 per condition). In each run, 500 ground-truth proteins were placed in a 3000 nm x 3000 nm ROI, with either 10 clusters of 10 molecules each, overlaid with 400 CSR molecules (light clustering) or 10 clusters of 40 molecules each, with 100 overlaid CSR molecules (heavy clustering). Clustered points were simulated as symmetric Gaussian clusters with a standard deviation of 30 nm, and the cluster centres were uniformly distributed over the ROI. Again, both light and heavy blinking was then added to the localisations, resulting in 4 conditions of spatial organisation and blinking characteristics (Figure B.3 a). We used Bayesian cluster analysis [25] for detection of clusters in MBC and DTT corrected data sets. Only MBC could consistently recover the 10 clusters under varying degrees of blinking severity (Figure B.3 b). The failure of DTT to recover the correct number of clusters is even more evident in the case of heavy clustering (Figure B.3 c and d).

B.2.5 Recovery of the ground truth

In addition to simulating realistic data, we also consider a more controlled, synthetic setup wherein ∼500 fluorescent proteins are regularly positioned on a ∼3000 nm × 3000 nm grid. The nature of this dataset allows for easier comparative visualisation of the performance of MBC and DTT (Figure B.4 a), and the improvements offered by our method are visually clear. To validate this, we also compute the 1st Wasserstein distance between the true and corrected grids. This can be thought of as the cost of transporting a standardised mass between two sets of points, and is also known as the earth mover's distance. For a perfectly reconstructed grid, this distance is zero, with any discrepancy increasing the distance. For 50 realisations of both light and heavy blinking on the grid, we see that MBC presents an improvement over DTT, with a lower distance to the true grid, particularly under heavy blinking conditions (Figure B.4 b). Because MBC is robust to heavy blinking, relative to DTT, it is in fact able to use heavy blinking to its advantage, by averaging localisation precisions from large groups of merged observations (Figure B.4 c).

B.2.6 Determining optimal imaging conditions

As a final test using known ground-truth simulated data, we used Virtual-SMLM[13] to simulate raw camera frames. This allowed us to test the effect of varying both the camera frame rate and the intensity of the 405 nm activation laser on the performance of MBC. A ground truth of CSR fluorescent proteins were simulated (Figure B.6 a), imaged using the virtual microscope and output analysed with ThunderSTORM. The camera integration time was set to either 10 ms or 40 ms and the 405 nm laser intensity either kept constant, or ramped to maintain a constant density of point spread functions (PSFs) per frame over the course of the acquisition. Raw localisations (Figure B.6 a) were then corrected using MBC (Figure B.6 b). The Wasserstein distance shows marginally superior performance of the reconstruction when using constant 405 laser power and when using longer, 40 ms frames. We attribute this to the lower density of PSFs per frame in the constant-405 case leading to fewer overlapped PSFs during localisation and to the increased localisation precision offered by the longer frames (Figure B.6 c). The performance of MBC itself is only weakly dependent on the

imaging conditions, and in each condition we were able to recover the ground truth number of molecules to within around 10% error. We conclude therefore that when using MBC, PALM imaging conditions should be chosen to maximise conventional notions of data quality — low density of PSFs and high signal-to-noise ratio. Because of this, we also conclude that MBC is also backwards compatible with all historically acquired PALM data.

B.2.7 Analysis of experimental data

Nanoscale clustering is posited to play a role in regulating protein-protein interactions and therefore the efficiency of signalling propagation along pathways[22]. In the context of an immune response, T cell microclusters of proximal signalling molecules have been widely documented by conventional total internal reflection fluorescence (TIRF) microscopy[12, 20]. Many of these have recently been studied by SMLM and shown to also be clustered on the nanoscale[29, 17, 24, 21]. The claim has proved controversial however, with counter-proposals that, in some circumstances, proteins may in fact be randomly distributed on the cell surface, with observed clustering attributed to multiple-blinking artefacts inherent to SMLM [23]. For PALM data, MBC should enable researchers to navigate this controversy.

To demonstrate the application of MBC to experimental data, we analysed the distribution of the adaptor protein LAT[5] in the plasma membrane of the Jurkat CD4+ Helper T cell line at an artificial immune synapse formed against an activating, antibody coated coverslip (see Supplementary material). To assess the role of intracellular phosphorylation in maintaining this distribution, we also mutated intracellular tyrosine residues to phenylalanine (YF LAT). Both wild-type (WT) LAT and YF LAT were fused to the photoconvertible fluorescent protein mEos3.2 with cells imaged under TIRF illumination. Raw localisations were obtained using ThunderSTORM and then corrected using MBC. The resulting corrected localisations were then tested for spatial randomness using the L-function, and any regions found to be clustered subjected to Bayesian cluster analysis[25].

Figure B.5 shows WT and YF LAT-mEos3.2 from representative regions (from n = 12 - 25 ROIs from 3-6 cells) acquired from the central regions of the cell synapse and from the synapse periphery, both before (Figure B.5 a) and after (Figure B.5 b) correction using MBC. Clearly, the large, dense clusters evident in the uncorrected data in all conditions are reduced in the corrected regions. However, by analysing the L-function curves from the ROIs (Figure B.5 c) and extracting the maximum value of those curves (Figure B.5 d), we were able to perform significance testing on whether the LAT distributions were truly CSR. For the two WT LAT conditions, the null hypothesis that LAT is randomly distributed was rejected in most regions. Therefore, it is likely that WT LAT was clustered in most analysed WT ROIs. This was not true for the YF mutant however, with the null hypothesis of randomly distributed LAT not rejected in the majority of peripheral regions (Figure B.5 d). This therefore may point to a role of intracellular tyrosine phosphorylation in maintaining LAT clustering.

For all regions where the CSR null hypothesis was rejected (treated as clustered regions) we then further interrogated the data using Bayesian cluster analysis. In addition to existing cluster descriptors output by the algorithm, the number of points

per cluster (cluster membership) is now biologically relevant, since this now represents the number of real fluorophores, not detected localisations. For WT LAT the data showed no statistically significant difference in cluster membership between central and peripheral regions. However, the YF mutant showed a significant decrease in the number of molecules per cluster in peripheral regions, both when compared to YF central regions ($p = 0.026$) and compared to WT peripheral regions ($p = 0.001$) (Figure B.5 e). Other outputs from the cluster analysis: number of clusters per ROI, cluster radius, percentage of molecules in clusters, total molecules per ROI and the relative density of molecules inside and outside clusters are shown in Figure B.7, with p-values summarised in Table B.2. The decrease in cluster membership and, in some ROIs, the loss of clustering altogether, in peripheral regions of the T cell synapse resulting from the YF mutation, is a strong indication that intracellular tyrosine phosphorylation is involved in maintaining LAT signalling clusters. Signalling phosphorylation events are known to originate in the synapse periphery and it is therefore consistent that the effect of the mutation is most pronounced there, compared to the central region where signalling is terminated[27].

B.3 Discussion

Super-resolution fluorescence microscopy by SMLM, such as PALM, results in a pointillist data representing an attempted realisation of the underlying ground-truth fluorophore locations1. A common goal in the biological sciences is to test whether such underlying distributions are clustered or randomly distributed and, if clustered, to determine their clustering properties. Achieving this goal has proved difficult however, because the generated localisations are corrupted by artefacts, principally the repeated localisation of the same fluorophore due to multiple-blinking[1]. This has led to controversy about whether proteins are truly clustered in cells, hindering our understanding of the causes and function of nanoscale protein clustering.

Here, we develop an algorithm, MBC, for correcting multiple-blinking that requires no user input, no additional calibration data, and is not limited to a specific analysis goal. We show that it can be used to reliably test for spatial randomness or recover other clustering properties from the ground truth. A number of methods have been put forward to test for spatial randomness in SMLM data. These include, for example, methods based on varying the labelling density and observing the effects on specific cluster analysis outputs[6] or by labelling the same species with two different fluorophores allowing a cross-comparison to be made[4]. These methods, however, require multiple sample preparation rounds and are therefore more complex and time-consuming. Correction can also be made by measuring blinking behaviour in a separate sample of well-isolated fluorophores, but this again adds complexity and experimental effort and requires the assumption that probe photophysics is maintained between the sample and the calibration. It is also possible to measure or simulate multiple-blinking using realistic photophysical models and use these to derive new CSR confidence intervals for the L-function curves[19]. It should be noted however that while all of these competing methods can be used to account for multiple-blinking, none produce a new set of corrected positions and therefore none can be used to extract rich descriptors such as those output by a clustering

algorithm. MBC therefore represents a new capability - of obtaining a set of corrected ground-truth locations of sufficient quality that any subsequent statistical analysis can be conducted with assurance.

The limitations of MBC are as follows. The method is only applicable to the four-state photophysical model typical of PALM acquisitions, and therefore cannot be used to correct dSTORM or other SMLM modalities. Performance of the correction will decrease as the clustering of the ground-truth increases, however, it tested favourably with realistic and heavily clustered scenarios. The method also adds computational time to any analysis pipeline. For a 3000 nm x 3000 nm ROI containing 500 ground-truth proteins, we estimate the MBC step to take 3-5 minutes per ROI on a standard desktop computer. Of course, as it results in fewer points per ROI, subsequent analysis will typically be accelerated. While here the correction is limited to 2D data, it can in principle be adapted to 3D x,y,z coordinates. In conclusion, MBC allows for accurate recovery of ground-truth fluorophore positions, with enhanced precision, from PALM data sets subjected to multiple-blinking artefacts. For the first time, these corrected sets are of sufficient quality to allow accurate cluster analysis and the statistical testing for complete spatial randomness. We therefore believe that PALM combined with MBC will be an invaluable tool for addressing questions on the existence, determinants and functions of protein nanoscale clustering.

Data and code availability

Raw experimental data available upon request. MBC code is available as Supplementary Material together with installation instructions and example simulated data sets.

Acknowledgements

The authors would like to thank Ute Hahn (Aarhus University) for motivating this project in initial discussions. L.G.J was supported by the Centre for Stochastic Geometry and Advanced Bioimaging, funded by grant 8721 from the Villum Foundation. D.O. acknowledges funding from BBSRC grant BB/R007365/1. P.R.D. acknowledges funding from the BBSRC grant BB/R007837/1. We also acknowledge the use of the King's College London Nikon Imaging Centre (NIC).

Author contributions

L.G.J. developed the software. L.G.J., T.Y.H., D.M.O. and P.R-D conceived the experiments. L.G.J. and T.Y.H. ran analysis. L.G.J. and T.Y.H. provided simulated data. D.J.W., J.G. and D.S. provided additional simulated and experimental data. L.G.J., T.Y.H., D.M.O. and P.R-D wrote the manuscript. L.G.J. and P.R-D. conceived the method.

B.I Supplementary material

Blinking simulation parameters

Table B.1: Rate parameters used to simulate multiple-blinking for the light and heavy blinking cases, using the 4-state model shown in Figure B.1 b.

Rate parameter	Light blinking (LB)	Heavy blinking (HB)
r_F	$0.005s^{-1}$	$0.005s^{-1}$
r_B	$8s^{-1}$	$2.5s^{-1}$
r_D	$10s^{-1}$	$10s^{-1}$
r_R	$0.75s^{-1}$	$0.75s^{-1}$

Sample preparation

For LAT images, Jurkat E6.1 cells (ECACC 88042803) expressing LAT-mEos3.2 (wild-type, WT LAT, or signaling deficient mutant, YF LAT) were introduced to anti-CD3 (at 2 μg/ml; eBioscience clone OKT3, 16-0037-81) and anti-CD28 (at 5 μg/ml; RnD Systems, clone CD28.2, 16-0289-85) coated glass-bottomed chamber slides (#1.5 glass, ibidi μSlides) at 50×10^3 cells/cm^2 in warm HBSS and incubated at 37°C for 5 minutes to allow for synapse formation. The chamber wells were gently washed with warm HBSS and then fixed in 3% paraformaldehyde in phosphate-buffered saline (PBS) for 20 minutes at 37°C. Fixed cells were washed five times in PBS and used immediately for PALM imaging.

Imaging

PALM image sequences were acquired on a Nikon N-STORM system in a TIRF configuration using a 100 × 1.49 NA CFI Apochromat TIRF objective for a pixel size of 160 nm. Samples were continuously illuminated with 561 nm laser light at approximately 2 kW/cm^2 and 405 nm laser light (to induce photo-conversion) at approximately 2 W/cm^2. Images were recorded on an Andor IXON Ultra 897 EMCCD with an electron multiplier gain of 200 and pre-amplifier gain profile 3 to a centered 256 × 256 pixel region at 40 ms per frame for 5,000 to 15,000 frames.

Virtual microscope simulations

Raw camera frames were generated using Virtual-SMLM [13] operating in PALM mode (i.e., using a 4 state photophysical model). The frame rate was set to 25 or 100 frames per second. The activation laser (i.e. initial state transition) was either fixed or ramped up over the acquisition. In the first case, the number of fluorophores emitting per frame decreases over time. In the second case, it remains constant over the acquisition. Emission traces were generated independently for each fluorophore and imaging continued until all fluorophores had been imaged and bleached. All other state transition probabilities and photophysics properties were fixed to mimic mEos blinking characteristics. The PSFs were recorded on a virtual EMCCD camera, with an EM gain fixed at 300. Virtual-SMLM took as input ground truth maps of

mEos2 positions. 5556 mEos proteins were placed randomly over a 10000 nm × 10000 nm 2D area. Generated camera frames were then analysed using ThunderSTORM [18] and the data cropped into non-overlapping 3000 × 3000 nm regions.

Localisation

Localisation of fluorophore coordinates were reconstructed using ThunderSTORM and corrected for sample drift using cross-correlation of images from 5 bins at a magnification of 5. No further post-processing was performed.

Mathematical details

Marginal likelihood of clusters

We represent the observed process by a series of localisations $(X_i, Y_i)_{i=1}^n$ with associated 'blink' times $T_1, ..., T_n$, and localisation uncertainties $\sigma_1^2, .., \sigma_n^2$, where $R = [x_0, x_1] \times [y_0, y_1]$ is the region of interest. For a given partition of the localisations into groups, we compute the marginal likelihood of the data as follows. Consider a group comprising the observations $1, ..., m$, with $1 \leq m \leq n$ (without loss of generality), posited to correspond to one, distinct, molecule. In particular, we defer until later the treatment of background noise. The independence assumptions set out in the main article result in the following marginal likelihood factorisation:

$$P((X_i)_{i=1}^n, (Y_i)_{i=1}^n, (T_i)_{i=1}^n) = P((X_i)_{i=1}^n) P((Y_i)_{i=1}^n) P((T_i)_{i=1}^n). \tag{B.I.1}$$

Denoting by $\mu = (\mu_X, \mu_Y)$ the true position of the molecule, the spatial components above have likelihood (given only for $(X_i)_{i=1}^m$)

$$P((X_i)_{i=1}^m \mid \mu_X) = \prod_{i=1}^m (2\pi\sigma_i^2)^{-\frac{1}{2}} exp\left\{-\frac{1}{2}\left(\frac{X_i - \mu_X}{\sigma_i}\right)^2\right\} \tag{B.I.2}$$

$$= (2\pi)^{-\frac{m}{2}} \left(\prod_i \sigma_i\right)^{-1} exp\left\{-\frac{1}{2}\sum_i \eta_i (X_i - \mu_X)^2\right\}, \tag{B.I.3}$$

where $\eta_i = \frac{1}{\sigma_i^2}$. Defining the weighted mean

$$\tilde{X} = \frac{\sum_i \eta_i X_i}{\sum_i \eta_i}, \tag{B.I.4}$$

we find

$$P((X_i)_{i=1}^m \mid \mu_X) = (2\pi)^{-\frac{m}{2}} \left(\prod_i \sigma_i\right)^{-1} exp\left\{-\frac{1}{2}\sum_i \eta_i \left(X_i - \tilde{X}\right)^2\right\} exp\left\{-\frac{\sum_i \eta_i}{2}\left(\mu_X - \tilde{X}\right)^2\right\}. \tag{B.I.5}$$

Placing a uniform prior on μ_X, we find

$$P((X_i)_{i=1}^m \mid \mu_X) = (2\pi)^{-\frac{m}{2}} \left(\prod_i \sigma_i\right)^{-1} exp\left\{-\frac{1}{2}\sum_i \eta_i \left(X_i - \tilde{X}\right)^2\right\} \tag{B.I.6}$$

$$\times (x_1 - x_0)^{-1} \int_{x_0}^{x_1} exp\left\{-\frac{\sum_i \eta_i}{2}\left(\mu_X - \tilde{X}\right)^2\right\} d_{\mu_X} \tag{B.I.7}$$

$$= (2\pi)^{-\frac{m}{2}} \left(\prod_i \sigma_i\right)^{-1} exp\left\{-\frac{1}{2}\sum_i \eta_i \left(X_i - \tilde{X}\right)^2\right\} \tag{B.I.8}$$

$$\times (x_1 - x_0)^{-1} (2\pi)^{\frac{1}{2}} \left(\sum_i \eta_i\right)^{-\frac{1}{2}} \left\{\Phi\left(\frac{x_1 - \tilde{X}}{(\sum_i \eta_i)^{-\frac{1}{2}}}\right) - \Phi\left(\frac{x_0 - \tilde{X}}{(\sum_i \eta_i)^{-\frac{1}{2}}}\right)\right\}. \tag{B.I.9}$$

The temporal component has likelihood

$$P((T_i)_{i=1}^m) = P(u)P(T_{\min})\prod_k P(f_k)\prod_k P(d_k), \tag{B.I.10}$$

each term is computed as follows. The blink times $T_1, ..., T_m$ are not typically observed exactly, and instead one has access only to associated frame numbers $F_1, ..., F_m$, taken to represent (small) windows of time containing them. We therefore consider a visit to the fluorescent state to be a block of $L \geq 1$ contiguous fluorescent frames (or consecutive frame numbers), and impute the length of this visit to be the time elapsed over $L - 1$ frames, to obtain auxiliary quantities

$$f_k : \text{time spent in fluorescent state } (k\text{th visit}). \tag{B.I.11}$$

Up to discrete-approximation error, each f_k represents the minimum of two exponential random variables with respective rates r_D and r_B, with likelihood contribution $P(f_k) = (r_D + r_B)e^{-(r_D+r_B)f_k}$.

Similarly, let d_k denote the time elapsed over the kth interval between noncontiguous frames, taken to represent

$$d_k : \text{time spent in dark state } (k\text{th visit}). \tag{B.I.12}$$

The likelihood contribution is

$$P(d_k) = r_R e^{-r_R d_k} \frac{r_D}{r_D + r_B}. \tag{B.I.13}$$

The initial switch of the fluorophore to the activated state happens at time $T_{\min}$, computed simply as the minimum T_i value, and this contributes

$$P(T_{\min}) = r_F e^{-r_F T_{\min}}, \tag{B.I.14}$$

to the likelihood.

Finally, let u denote the time since the last blink (a period during which it is unknown whether the process has entered a dark or bleached state). The final contribution is

$$P(u) = \frac{r_D}{r_B + r_D} e^{-r_R u} + \frac{r_B}{r_B + r_D} \tag{B.I.15}$$

To finalise calculations, one must account for background noise (in the case m = 1). Such points are assumed to be uniform in spacetime. The complete marginal likelihood is:

$$\pi((X_i)_{i=1}^m,(Y_i)_{i=1}^m,(T_i)_{i=1}^m) = \begin{cases} (1-\alpha)P((X_i)_{i=1}^m,(Y_i)_{i=1}^m,(T_i)_{i=1}^m) & m>1 \\ \alpha V^{-1} + (1-\alpha)P(P((X_i)_{i=1}^m,(Y_i)_{i=1}^m,(T_i)_{i=1}^m)) & m=1, \end{cases} \tag{B.I.16}$$

where $V = T(x_1 - x_0)(y_1 - y_0)$, T is the length of the period of observation, and α is the background probability.

Identifying and summarizing clusters

For both MBC and DTT clustering, an expected number of clusters, N, is first estimated, and a version of agglomerative hierarchical clustering (AHC) is then used to partition the dataset into N clusters. In AHC, each point is initially considered to be a distinct cluster. Using a user-specified metric and a linkage criterion, a stepwise greedy merging of the closest clusters is repeated until a partition with a predetermined number of clusters is obtained, or until no more clusters can be merged with a distance less than some specified number. The metric determines the distances between pairs of points, and the linkage criterion generalises these to a distance between clusters. Once the final partition has been identified, we merge each cluster down to its estimated centre, and the uncertainty of the centre is computed. In the following, we use the notation

$$L = (X, Y) \tag{B.I.17}$$

$$d_l(L_1, L_2) = \sqrt{(X_1 - X_2)^2 + (Y_1 - Y_2)^2} \tag{B.I.18}$$

$$d_t(T_1, T_2) = |T_1 - T_2|. \tag{B.I.19}$$

MBC clustering

For MBC, the number of desired clusters, N, is an output of the rate-estimation step, and is thus decoupled from the clustering problem. For the AHC step, we use the family of metrics

$$d_S((L_1, T_1), (L_2, T_2)) = \frac{d_l(L_1, L_2)}{\sigma_1 + \sigma_2} + S \cdot d_t(T_1, T_2), \tag{B.I.20}$$

for $S \geq 0$, which is simply the sum of the (scaled) Euclidean distance between the locations and times. For the linkage criterion we chose Ward's Minimum Variance Method, as implemented via the Lance-Williams formula [9], as it tends to find homogeneous clusters of spherical shape.

By varying S, we obtain a sequence of partitions, each slightly different but all chosen to have N clusters. The marginal likelihood is computed for each of the resulting partitions, and the most likely partition is selected.

DTT clustering

DTT, or dark time thresholding, is a general idea in SMLM blinking correction literature, but implementation details are rarely discussed. The general principle is

to merge locations that are close in space and time, with hard thresholds on the maximally allowed bridging distances in space and time. As a way to implement this idea in the AHC framework, we define the distance between 2 observations as

$$d_{\tau_S,\tau_t}((L_1,T_1),(L_2,T_2)) = d_l(L_1,L_2) + d_t(T_1,T_2) + \infty \cdot \mathbb{1}(d_l(L_1,L_2) > \tau_S \text{ or } d_t(T_1,T_2) > \tau_t), \tag{B.I.21}$$

where $\infty \cdot 0 = 0$. Although not strictly a metric, this distance measure allows us to implement the dark time thresholding idea. We use the single-linkage criterion for cluster merging, which considers the distance between two clusters to be the smallest pairwise distance between them. Combined with our metric, this means that the clustering algorithm is allowed to merge points and clusters, so long as they can be combined via paths that do not violate the hard thresholds. Finally, a clustering is achieved by continuing to merge clusters until only infinite distances between clusters remain (no more legal merges can be made). For τ_s, we used 4 times the mean localisation uncertainty. The temporal threshold, τ_t, was determined as follows. First, the method of Annibale [3] was used to determine N. Next, τ_t was increased incrementally until the AHC algorithm produced a partition with N clusters, or as close to N as possible.

Cluster centres and uncertainty

Let $(X_i, Y_i)_{i=1}^m$ be the coordinates of an arbitrary cluster with centre μ. Once a particular clustering is given, it makes sense to treat the cluster centres as fixed parameters to be estimated. Thinking therefore of μ as fixed, the maximum likelihood estimator, $\hat{\mu}$, maximizes the likelihood of the cluster coordinates

$$\log\left(P((X_i,Y_i)_{i=1}^m)\right) = -\frac{\sum_i \eta_i}{2}\left((\mu_X - \tilde{X})^2 + (\mu_Y + \tilde{Y})^2\right) + C, \tag{B.I.22}$$

where C does not depend on μ, and it follows immediately that

$$\hat{\mu} = (\tilde{X},\tilde{Y}) = \left(\frac{\sum_i \eta_i X_i}{\sum_i \eta_i}, \frac{\sum_i \eta_i Y_i}{\sum_i \eta_i}\right). \tag{B.I.23}$$

Using $\hat{\mu}$, we can estimate the position of the molecule associated with a given cluster. As the coordinates of $\hat{\mu}$ are independent, the covariance matrix of $\hat{\mu}$ is given as

$$\mathbb{V}[\hat{\mu}] = \tilde{\sigma}^2 I_2, \tag{B.I.24}$$

where I_2 is the 2×2 identity matrix, and

$$\tilde{\sigma}^2 = \mathbb{V}[\tilde{X}] = \frac{\sum_i \eta_i^2 \sigma_i^2}{(\sum_i \eta_i)^2} = \frac{1}{\sum_i \frac{1}{\sigma_i^2}}, \tag{B.I.25}$$

and the updated localisation uncertainty is then simply the associated standard deviation

$$\tilde{\sigma} = \frac{1}{\sqrt{\sum_i \frac{1}{\sigma_i^2}}}. \tag{B.I.26}$$

Significance testing

The p-values reported in Table B.2 are based on a permutation test of the difference of means, using 10,000 simulations.

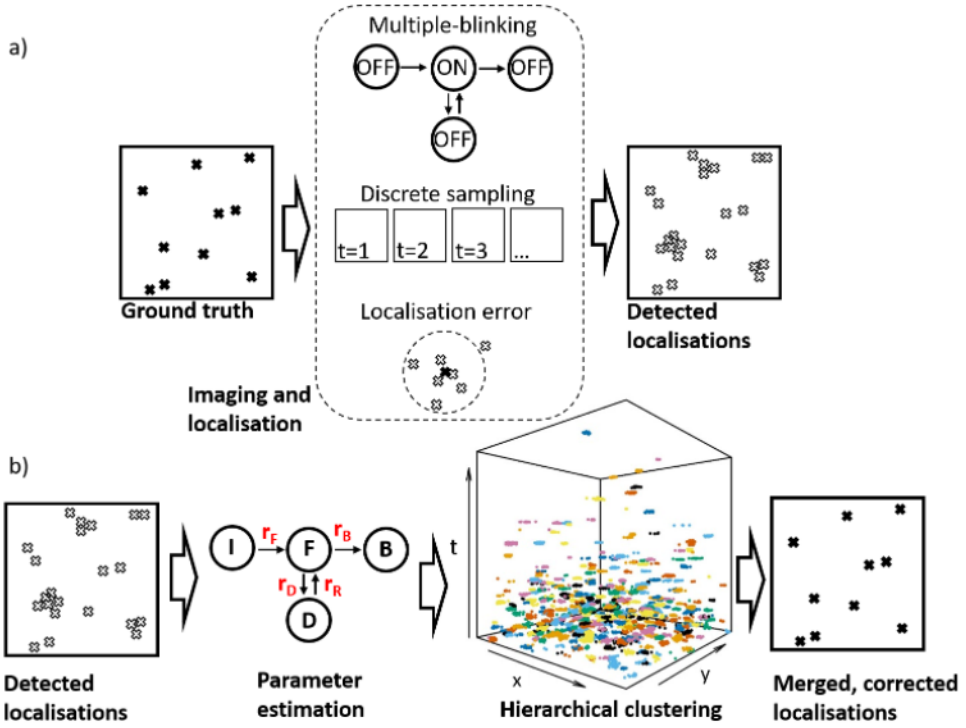

Figure B.1: Illustration of the MBC workflow. a) During PALM image acquisition and subsequent localisation steps, the ground-truth protein positions are corrupted by multiple-blinking in combination with discretisation by the camera frames and scrambling by the localisation uncertainty, resulting in a data set which is over-populated and over-clustered. b) Our algorithm (MBC) takes as input (x, y, t, σ) data and estimates the rate parameters of a 4-state photophysical model, from which it derives the total number of molecules in the ROI. This is then used as input to a hierarchical clustering step (experimental data shown with colours representing the clusters found), after which clusters are merged to their centres, creating a new dataset free from multiple-blinking and with enhanced localisation precision.

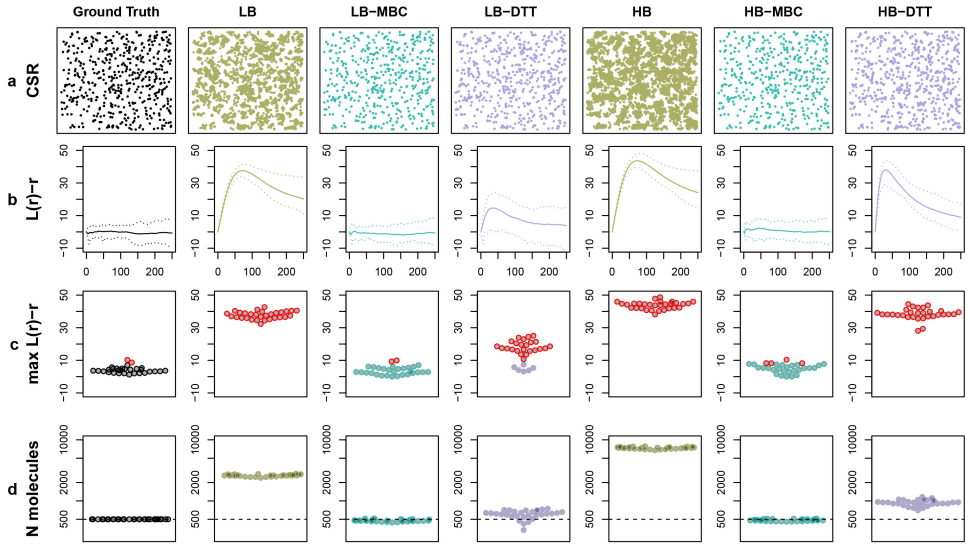

Figure B.2: Testing for spatial randomness. a) Representative simulated data of ground-truth CSR points with light or heavy blinking (LB or HB) either corrected by MBC or DTT as a comparison. b) L(r)-r (mean in solid line) with pointwise 95% quantile bands (dashed line). c) max(L(r)-r) derived from these functions. Points in red correspond to ROIs that were rejected as CSR in a Monte-Carlo test ($p \leq 0.05$). Note that DTT often (and sometimes always) incorrectly rejects the CSR null hypothesis, whereas MBC does not. d) Number of molecules per ROI (log-scaled) showing superior correction of MBC compared to DDT in light and heavy blinking cases.

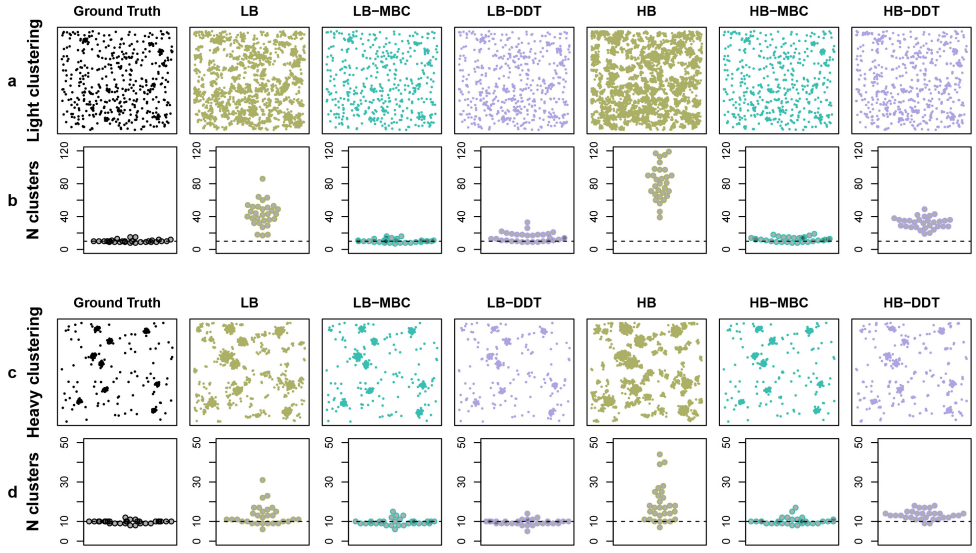

Figure B.3: Testing on clustered ground-truth data sets. a) Low levels of clustering with either light or heavy blinking, corrected by MBC or DDT. b) Number of detected clusters (true number of clusters in dashed line) by Bayesian analysis. c) High levels of clustering with either light or heavy blinking, corrected by MBC or DDT. d) Number of detected clusters (true number of clusters in dashed line) by Bayesian analysis. MBC has superior performance in all cases except heavy clustering/light blinking, where results are comparable.

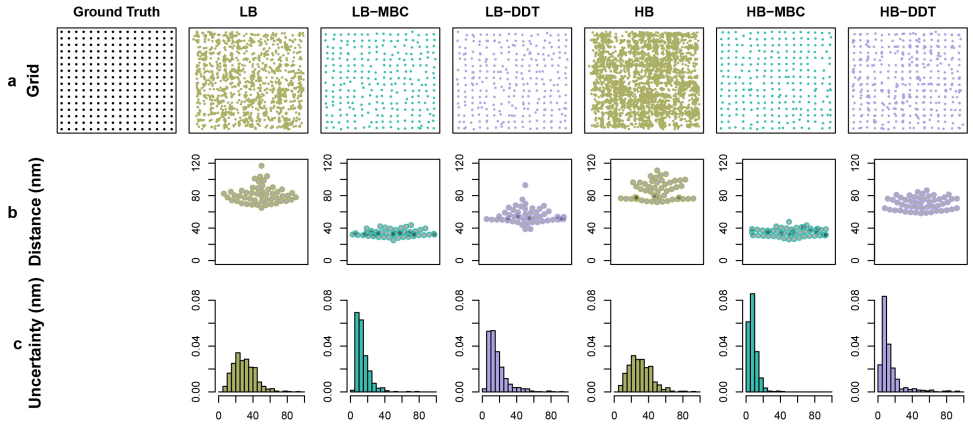

Figure B.4: Testing against molecules on a fixed grid. a) Ground truth and representative simulated data. b) Wasserstein distances between simulated data and ground truth showing that MBC generates output closer to the ground truth. c) Normalised histograms of localisation uncertainties of individual molecules (nm) showing that MBC also generates increased localisation precisions compared to uncorrected data or DDT.

Table B.2: Summary of means and p-values for experimental data analysis of WT LAT and YF LAT at the immunological synapse.

	WT Centre mean	WT Periphery mean	YF Centre mean	YF Periphery mean	WT Centre vs YF Centre p-value	WT Periphery vs YF Periphery p-value	WT Centre vs WT Periphery p-value	YF Centre vs YF Periphery p-value
Number of clusters	10.0	16.5	4.76	4.25	0.006	$< 10^{-5}$	0.043	0.701
Number of molecules per cluster	29.7	18.3	42.1	4.26	0.574	0.001	0.316	0.026
Cluster radius (nm)	73.5	52.5	100	38.6	0.372	0.167	0.075	0.027
Percentage of molecules in clusters	22.6	21.8	35.2	23.4	0.151	0.568	0.761	0.172
Total number of molecules	931	866	226	79.6	$< 10-5$	$< 10-5$	0.794	0.003
Relative density of clustered vs unclustered molecules	15.7	20.8	53.0	217	$< 10-5$	$< 10-5$	0.162	0.006

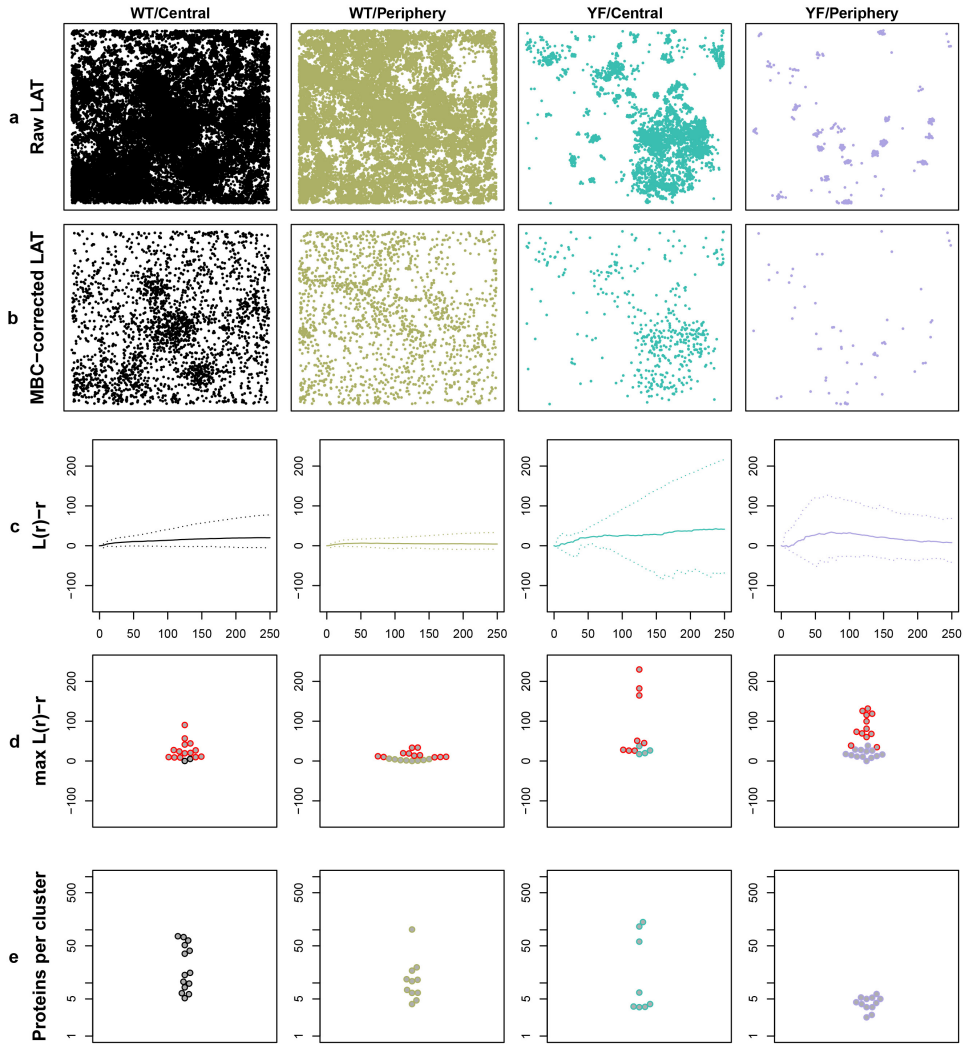

Figure B.5: Cluster analysis of LAT-mEos3.2 at the T cell immunological synapse. a) Representative, raw 3000 nm x 3000 nm ROIs from each of the 4 conditions (WT Centre, WT Periphery, YF Centre and YF Periphery). b) Representative MBC-corrected ROIs, on which analysis was conducted. c) L(r)-r (mean in solid line) with pointwise 95% quantile bands (dashed line). d) max(L(r)-r) derived from these functions. Points coloured in red correspond to ROIs where the CSR null hypothesis was rejected in a Monte Carlo test ($p < 0.05$). These ROI were then retained for subsequent Bayesian cluster analysis. e) Number of proteins per cluster detected by Bayesian analysis.

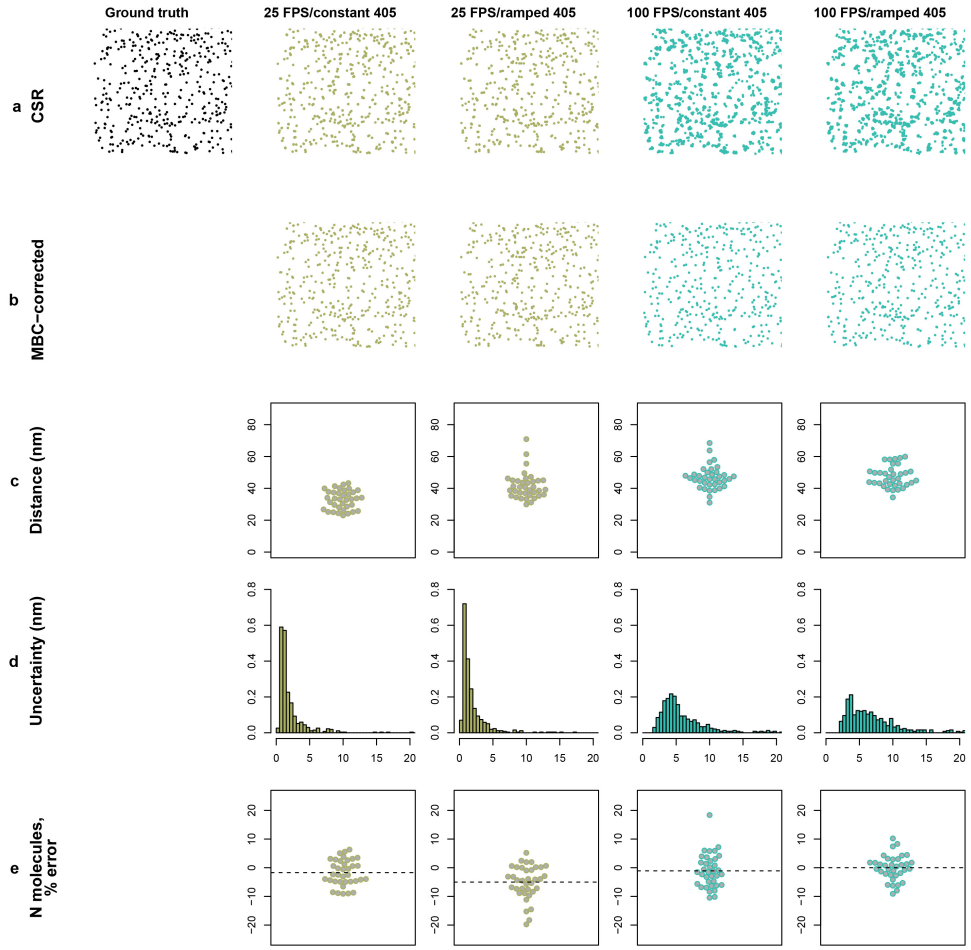

Figure B.6: MBC Performance as a function of camera frame rate and the activating, 405 nm laser power. a) Example ground-truth and raw localisation maps for the different conditions. b) Example MBC-corrected maps. c) Wasserstein distances. d) Normalised histograms of localisation uncertainty. e) Percentage error in estimated number of ground-truth molecules (mean in dashed line).

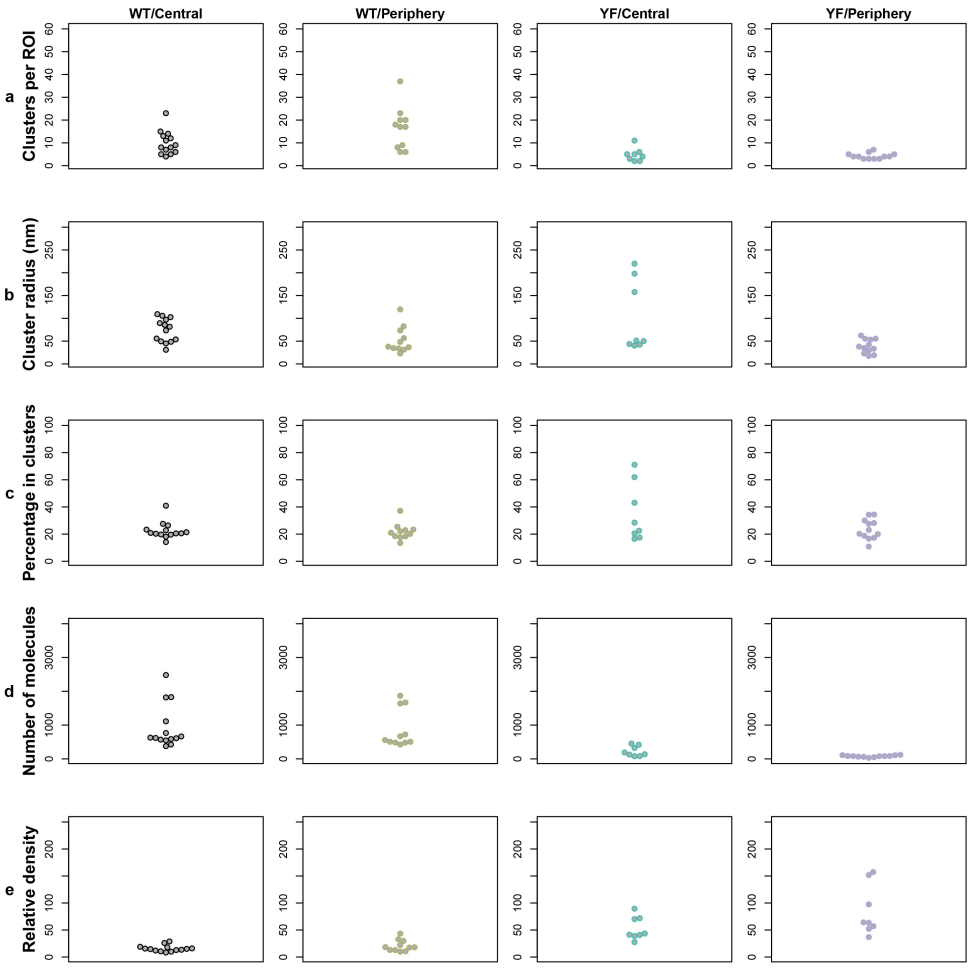

Figure B.7: Additional statistics from the Bayesian cluster analysis of non-CSR LAT-mEos3.2 regions. a) Number of detected clusters, b) cluster radii (nm), c) percentage of molecules in clusters, d) number of molecules per ROI and e) relative density of molecules located in clusters as compared to the surrounding region.

References

[1] Annibale, P., M. Scarselli, A. Kodiyan and A. Radenovic (Apr. 2010). Photoactivatable Fluorescent Protein mEos2 Displays Repeated Photoactivation after a Long-Lived Dark State in the Red Photoconverted Form. *The Journal of Physical Chemistry Letters* 1(9), 1506–1510. DOI: 10.1021/jz1003523.

[2] Annibale, P., S. Vanni, M. Scarselli, U. Rothlisberger and A. Radenovic (2011a). Identification of clustering artifacts in photoactivated localization microscopy. *Nature methods* 8(7), 527.

[3] Annibale, P., S. Vanni, M. Scarselli, U. Rothlisberger and A. Radenovic (2011b). Quantitative photo activated localization microscopy: unraveling the effects of photoblinking. *PloS one* 6(7), e22678.

[4] Arnold, A.M, M.C. Schneider, C. Hüsson, R. Sablatnig, M. Brameshuber, F. Baumgart and G.J. Schütz (Mar. 2020). Verifying molecular clusters by 2-color localization microscopy and significance testing. *Scientific Reports* 10(1). DOI: 10.1038/s41598-020-60976-6.

[5] Balagopalan, L., R.L. Kortum, N.P Coussens, V.A. Barr and L.E. Samelson (Oct. 2015). The Linker for Activation of T Cells (LAT) Signaling Hub: From Signaling Complexes to Microclusters. *Journal of Biological Chemistry* 290(44), 26422–26429. DOI: 10.1074/jbc.r115.665869.

[6] Baumgart, F., A.M Arnold, K. Leskovar, K. Staszek, M. Fölser, J. Weghuber, H. Stockinger and G.J. Schütz (June 2016). Varying label density allows artifact-free analysis of membrane-protein nanoclusters. *Nature Methods* 13(8), 661–664. DOI: 10.1038/nmeth.3897.

[7] Betzig, E., G.H. Patterson, R. Sougrat, O.W. Lindwasser, S. Olenych, J.S. Bonifacino, M.W. Davidson, J. Lippincott-Schwartz and H.F. Hess (2006). Imaging intracellular fluorescent proteins at nanometer resolution. *Science* 313(5793), 1642–1645.

[8] Coltharp, C., R.P Kessler and J. Xiao (2012). Accurate construction of photoactivated localization microscopy (PALM) images for quantitative measurements. *PLoS One* 7(12), e51725.

[9] Cormack, R.M (1971). A Review of Classification. *Journal of the Royal Statistical Society. Series A (General)* 134(3), 321. DOI: 10.2307/2344237.

[10] Diggle, P.J. (Mar. 1979). On Parameter Estimation and Goodness-of-Fit Testing for Spatial Point Patterns. *Biometrics* 35(1), 87. DOI: 10.2307/2529938.

[11] Fricke, F., J. Beaudouin, R. Eils and M. Heilemann (2015). One, two or three? Probing the stoichiometry of membrane proteins by single-molecule localization microscopy. *Scientific reports* 5, 14072.

[12] Grakoui, A. (July 1999). The Immunological Synapse: A Molecular Machine Controlling T Cell Activation. *Science* 285(5425), 221–227. DOI: 10.1126/science.285.5425.221.

[13] Griffié, J., T. Pham, C. Sieben, R. Lang, V. Cevher, S. Holden, M. Unser, S. Manley and D. Sage (Mar. 2020). Virtual-SMLM, a virtual environment for real-time interactive SMLM acquisition. DOI: 10.1101/2020.03.05.967893.

[14] Griffié, J., M. Shannon, C.L. Bromley, L. Boelen, G.L. Burn, D.J. Williamson, N.A. Heard, A.P Cope, D.M Owen and P. Rubin-Delanchy (Nov. 2016). A Bayesian cluster analysis method for single-molecule localization microscopy data. *Nature Protocols* 11(12), 2499–2514. DOI: 10.1038/nprot.2016.149.

[15] Jensen, L.G., D.J. Williamson and U. Hahn (Jan. 2021). Semiparametric point process modelling of blinking artifacts in PALM. arXiv: 2101.12285 [stat.AP].

[16] Lee, S.-H., J.Y. Shin, A. Lee and C. Bustamante (Oct. 2012). Counting single photoactivatable fluorescent molecules by photoactivated localization microscopy (PALM). *Proceedings of the National Academy of Sciences* 109(43), 17436–17441. DOI: 10.1073/pnas.1215175109.

[17] Lillemeier, B.F., M.A. Mörtelmaier, M.B. Forstner, J.B. Huppa, J.T. Groves and M.M Davis (Dec. 2009). TCR and Lat are expressed on separate protein islands on T cell membranes and concatenate during activation. *Nature Immunology* 11(1), 90–96. DOI: 10.1038/ni.1832.

[18] Ovesny, M., P. Křižek, J. Borkovec, Z. Švindrych and G.M Hagen (2014). ThunderSTORM: a comprehensive ImageJ plug-in for PALM and STORM data analysis and super-resolution imaging. *Bioinformatics* 30(16), 2389–2390.

[19] Platzer, R., B.K. Rossboth, M.C. Schneider, E. Sevcsik, F. Baumgart, H. Stockinger, G.J. Schütz, J.B. Huppa and M. Brameshuber (Oct. 2020). Unscrambling fluorophore blinking for comprehensive cluster detection via photoactivated localization microscopy. *Nature Communications* 11(1). DOI: 10.1038/s41467-020-18726-9.

[20] Purbhoo, M.A., H. Liu, S. Oddos, D.M Owen, M.A.A. Neil, S.V. Pageon, P.M.W. French, C.E. Rudd and D.M Davis (May 2010). Dynamics of Subsynaptic Vesicles and Surface Microclusters at the Immunological Synapse. *Science Signaling* 3(121), ra36–ra36. DOI: 10.1126/scisignal.2000645.

[21] Razvag, Y., Y. Neve-Oz, J. Sajman, M. Reches and E. Sherman (Feb. 2018). Nanoscale kinetic segregation of TCR and CD45 in engaged microvilli facilitates early T cell activation. *Nature Communications* 9(1). DOI: 10.1038/s41467-018-03127-w.

[22] Roob, E., N. Trendel, P. Rein ten Wolde and A. Mugler (Apr. 2016). Cooperative Clustering Digitizes Biochemical Signaling and Enhances its Fidelity. *Biophysical Journal* 110(7), 1661–1669. DOI: 10.1016/j.bpj.2016.02.031.

[23] Rossboth, B., A.M Arnold, H. Ta, R. Platzer, F. Kellner, J.B. Huppa, M. Brameshuber, F. Baumgart and G.J. Schütz (July 2018). TCRs are randomly distributed on the plasma membrane of resting antigen-experienced T cells. *Nature Immunology* 19(8), 821–827. DOI: 10.1038/s41590-018-0162-7.

[24] Rossy, J., D.M Owen, D.J. Williamson, Z. Yang and K. Gaus (Dec. 2012). Conformational states of the kinase Lck regulate clustering in early T cell signaling. *Nature Immunology* 14(1), 82–89. DOI: 10.1038/ni.2488.

[25] Rubin-Delanchy, P., G.L. Burn, J. Griffié, D.J. Williamson, N.A. Heard, A.P Cope and D.M Owen (Oct. 2015). Bayesian cluster identification in single-molecule localization microscopy data. *Nature Methods* 12(11), 1072–1076. DOI: 10.1038/nmeth.3612.

[26] Sengupta, P., T. Jovanovic-Talisman, D. Skoko, M. Renz, S.L. Veatch and J. Lippincott-Schwartz (2011). Probing protein heterogeneity in the plasma membrane using PALM and pair correlation analysis. *Nature methods* 8(11), 969.

[27] Varma, R., G. Campi, T. Yokosuka, T. Saito and M.L. Dustin (July 2006). T Cell Receptor-Proximal Signals Are Sustained in Peripheral Microclusters and Terminated in the Central Supramolecular Activation Cluster. *Immunity* 25(1), 117–127. DOI: 10.1016/j.immuni.2006.04.010.

[28] Veatch, S.L., B.B. Machta, S.A. Shelby, E.N. Chiang, D.A. Holowka and B.A. Baird (Feb. 2012). Correlation Functions Quantify Super-Resolution Images and Estimate Apparent Clustering Due to Over-Counting. *PLoS ONE* 7(2). Ed. by J. Rao, e31457. DOI: 10.1371/journal.pone.0031457.

[29] Williamson, D.J., D.M Owen, J. Rossy, A. Magenau, M. Wehrmann, J.J. Gooding and K. Gaus (June 2011). Pre-existing clusters of the adaptor Lat do not participate in early T cell signaling events. *Nature Immunology* 12(7), 655–662. DOI: 10.1038/ni.2049.

PAPER C

Regulated exocytosis: Renal aquaporin-2 3D vesicular network organization and association with F-actin

Mikkel R. Holst, Louis G. Jensen, Jesse Aaron, Frédéric H. Login, Sampavi Rajkumar, Ute Hahn, Lene N. Nejsum

Under revision for *American Journal of Physiology: Cell Physiology*

Abstract

Regulated vesicle exocytosis is a key response to extracellular stimuli in diverse physiological processes, but the nano-scale size of these vesicles has limited analysis of their 3D organization. Using 3D super resolution microscopy, we provide the first direct analysis of the 3D network of exocytic vesicles containing the renal water channel, Aquaporin-2 (AQP2). We show that AQP2 vesicles are 43 ± 3nm in diameter, similar to synaptic vesicles, and that there are two pools of vesicles, one associated with sub-cortical F-actin and the other localized close to the plasma membrane. AQP2 vesicle association with F-actin is enhanced in a serine 256 phospho-mimic of AQP2, whose phosphorylation is a key event in antidiuretic hormone-mediated AQP2 vesicle exocytosis. Our results indicate a conserved structure and organization of regulated exocytic vesicles in neurons and non-neuronal cells.

C.1 Main text

Cellular responses to extracellular stimuli are mediated via different signaling cascades. Nevertheless, a fundamental response is regulated vesicle exocytosis that is conserved in hormone regulated urine concentration, acidification of stomach contents, and neurotransmission. Signal-mediated vesicle exocytosis to the target plasma membrane alters the plasma membrane composition of ion and water channels, and induces the secretion of signaling molecules.

Immuno-electron microscopy and biochemical analysis of vesicles in neuronal synapses revealed that they contain specific proteins, their size is below the diffraction limit of light, and they localize close to the target plasma membrane with actin filaments (F-actin) [22]. In contrast, the 3D organization and physical interactions of regulated exocytic vesicles in other cell types have been generally limited to light microscopy and are poorly understood. Here, we circumvented these indirect and low resolution methods by utilizing recent advances in 3D super resolution microscopy (Interferometric Photoactivated Localization Microscopy (iPALM) [8, 18] that enable imaging of the nano-spatial organization of vesicular populations in cells at a resolution down to 20nm in the xy-axis (lateral) and 10-15nm in the z-axis (vertical).

As a generic example of regulated exocytosis in non-neuronal cells, we analyzed aquaporin-2 (AQP2) vesicular organization in a renal epithelial cell culture model system (MDCK cells). Aquaporins (AQPs) form homo-tetrameric water channels that facilitate passive transport of water across biological membranes. In renal collecting ducts, urine concentration is fine-tuned by regulated exocytosis of a subset of small subapical AQP2 vesicles to the plasma membrane in response to circulating levels of the antidiuretic hormone arginine vasopressin (AVP) [5, 10]. We used our previously described cell system, FRT-AQP2 cells, were AQP2 is expressed in MDCK cells under the control of a doxycycline inducible promoter [6, 21] and where AQP2 has been shown to shuttle to and from the plasma membrane (both apical and basolateral) in subconfluent cells in response to increased levels of cAMP, the signaling downstream of AVP. First, to confirm vesicular localization of AQP2, we employed expansion microscopy (ExM) [2], which increases resolution to approximately 70nm, allowing visualization of both large and smaller endosomal structures. ExM confirmed that AQP2 localized in the membranes of different sized vesicle structures, distributed throughout the cell cytoplasm (Figure C.4). Next, to enable iPALM imaging we used the cell setup in combination with transiently transfected AQP2 tagged with mEos3.2, a photoconvertible green/yellow fluorescent protein. Untagged AQP2 and mEos3.2-AQP2 were co-expressed in a ratio of $\sim$ 3:1 (referred to as AQP2 hereafter), which has been shown to prevent aggregation of the tetramer and enable imaging with fluorescently tagged AQP2 [1, 6]. Furthermore, F-actin has been suggested to form a barrier between AQP2 vesicles and the plasma membrane [9, 12, 20] but it has never been possible to obtain insight in the actual positioning of vesicles in respect to F-actin at this close localization to the plasma membrane. To enable imaging of F-actin in conjunction with AQP2 vesicles we used Alexa647 labeled phalloidin,

iPALM datasets consist of points with (x,y,z) coordinates, and we employed statistical methods for spatial point patterns to analyze the shape, size and spacing of AQP2-containing vesicles. To ensure we were imaging whole transport vesicles,

and not vesicles undergoing scission or fusion with the basal plasma membrane, nor micro domains in the basal plasma membrane, we used the coverslip as a reference zero-point and performed vesicle analysis in the niche 100-400nm above the coverslip (imaging setup in Figure C.5 A). The imaging revealed a network of AQP2 clusters (Figure C.1 A-B and movie 1), which we modeled as proteins lying on the surface of hollow spheres (similar to vesicles) observed with noise (Figure C.1 C). The average AQP2 vesicle diameter was 43 ± 3nm (Figure C.1 D), with 197 ± 60nm spacing (Figure C.1 E). The analysis showed that the z-range with the largest vesicle population was positioned 150-400nm from the coverslip. Our results support that AQP2 vesicles have similar sizes to that of pre-synaptic vesicles [17], but have smaller sizes compared to the larger diameter of transport vesicles in the secretory pathway and endocytic vesicles (reviewed in [13]).

We examined the blinking behavior of mEos3.2 tagged AQ2 in samples imaged with the iPALM system. As expected, we noted areas of high localization density that were consistent with the apparent vesicles seen in the ExM images shown in Figure C.4. Interestingly, we noted that the localizations corresponding to putative vesicles tended to be temporally clustered, rather than appearing randomly throughout the acquisition time, as shown in Figure C.5 B. We speculate that this unexpected behavior may be due to a self-activation mechanism, either due to the high fluorophore density or the fact that AQ2 exists as tetramers or both. However, as shown in the plot in Figure C.5 B, the localization density in these areas cannot be solely attributed to abnormally long on-times of the mEos3.2. Analysis of this plot indicates an average "on-time" of 66ms (or approximately 1.3 frames) within these areas.

Next, we imaged F-actin, which revealed a dense layer of F-actin in the cytoplasm approximately 200nm distal to the plasma membrane (Figure C.2 A-C). The majority (66.91%) of AQP2 vesicles were positioned between the plasma membrane and the dense F-actin layer (Figure C.2 D and movie 2) indicating that the F-actin layer did not compose a barrier towards the plasma membrane for this fraction of AQP2 vesicles. To tests in 3D if AQP2 vesicles associates with F-actin or if the proximity is random, we examined the spatial relationship of AQP2 vesicles with F-actin using a Monte Carlo test for independence of localizations. The distance from each AQP2 vesicle shell to the nearest 1000 neighboring (NN) F-actin localizations in central and peripheral regions of cells was computed, as was a mean-curve for all vesicles. We first assumed distributional invariance of AQP2 vesicle centers under shifts in the XY-plane and then simulated new mean-curves from the null-hypothesis of independence by randomly shifting AQP2 vesicles in XY, while keeping Z-coordinates for AQP2 fixed and XYZ-coordinates for F-actin fixed. Based on the simulated curves we performed a global envelope test based on extreme rank lengths [15]. The observed mean-curves for central and edge regions of the cells were both entirely outside their respective envelopes, indicating AQP2-to-F-actin distances that were shorter than expected if they were independent of each other (Figure C.2 E, pval = 0.002). Thus, the analysis revealed an association between AQP2 vesicles and F-actin (Figure C.2 A-C). Larger vesicles resembling recycling endosomes were also observed (Figure C.6). Our results indicate that there are two pools of small AQP2 transport vesicles, one closely associated with the F-actin layer distal to the plasma membrane, and the other localized between the F-actin layer and proximal to the plasma membrane. AVP binding to the AVP receptor elicits signaling cascades that culminate in phosphorylation

of several residues in the AQP2 COOH-terminal tail, and subsequent fusion of AQP2 vesicles with the PM (recently reviewed in [5]). AQP2 serine 256 (S256) phosphorylation by protein kinase A downstream of AVP is a key event [11], which can be mimicked by the AQP2-S256D mutation, and its nonphospho-mimic AQP2-S256A. The diameter of AQP2-S256A vesicles (41 ± 4nm) was similar to AQP2-wt vesicles (pval = 0.718) (Figure C.3 A-C), whereas AQP2-S256D (31 ± 4nm) vesicles were significantly smaller (pval = 0.022). Spacing between vesicles was not significantly different between AQP2-wt, AQP2-S256D and AQP2-S256A (pval = 0.06096) in the cell center or periphery (pval = 0.60049), when controlling for the number of vesicles per nm3.

Next, we examined the distribution of AQP2-S256D and AQP2-S256A vesicles in relationship to F-actin (Figure C.3 D). In the peripheral cytoplasm, AQP2-S256A vesicles were less associated with F-actin than AQP2-wt with a 58% larger distance between vesicles and the nearest 1000 neighboring F-actins (pval = 0.011). AQP2-S256D vesicles were 11% farther from F-actin than AQP2-wt, but this was not significantly different (pval = 0.531). In the cytoplasm central in the cell, AQP2-S256A vesicles were localized 86% (pval < 0.001) farther from F-actin than AQP2-wt vesicles, whereas AQP2-S256D had a similar distance to F-actin as AQP2-wt (pval = 0.356), indicating that non-phosphorylated AQP2 in S256 is less associated with F-actin than phosphorylated. These results suggest that phosphorylation of S256 AQP2 regulates the size of AQP2 vesicle clusters and their association with F-actin both in the central and peripheral region of the cell.

A key event in AVP mediated AQP2 vesicle exocytosis and urine concentration is AQP2-S256 phosphorylation. Our results indicate that the phospho-mimic S256 AQP2 correlates with increased AQP2 vesicle-F-actin association compared to the non-phospho-mimic AQP2-S256A. Previous studies reported that global F-actin depolymerisation results in AQP2 targeting to the plasma membrane [7, 9, 20], but it was unknown whether the F-actin layer constitutes a physical barrier between AQP2 vesicles and the plasma membrane and/or facilitates AQP2 vesicle delivery to the plasma membrane upon AQP2 S256 phosphorylation [16]. Rather than acting as a barrier to AQP2 vesicle exocytosis, our results support a model that association of AQP2 vesicles with F-actin is enhanced upon AQP2 S256 phosphorylation, and that this increases the propensity for vesicle accumulation with F-actin near the plasma membrane, and thus the likelihood of vesicle fusion with the plasma membrane. AQP2-wt and AQP2-S256D vesicles may have similar transport capacities along F-actin tracks, but differences in their plasma diffusion coefficients [1] and endocytosis rates [14] may result in an increased plasma membrane localization of AQP2-S256D compared to AQP2-wt. Moreover, small increases in circulating AVP may mobilize AQP2 vesicles in the niche between the F-actin layer and the plasma membrane without, or prior to, dissociation from the F-actin layer, thereby ensuring a rapid exocytic response.

Regulated vesicle exocytosis is a conserved response to many extracellular signals that result in the acidification of stomach contents, neurotransmission and hormone regulated urine concentration. Detailed analysis of these vesicles and F-actin has focused on the neuronal synapse, where specialized ∼40nm vesicles associate with F-actin close to the plasma membrane at the synaptic cleft [17, 22]. Our analysis of the spatial organization and physical associations of AQP2 vesicles with F-actin is

the first direct analysis of a 3D network of exocytic vesicles in a non-neuron cell type, and reveals striking similarities with synaptic vesicles in size, localization and clustering. This suggests that different signal-mediated vesicle exocytosis pathways have conserved mechanisms and organizations.

C.2 Materials and Methods

All reagents were purchased from Sigma Aldrich unless otherwise stated.

C.2.1 DNA preparation

The mEOs3.2-AQP2 constructs were generated by swapping the pPAGFP coding sequence of the pPAGFP-AQP2 plasmids (8) with the mEOs3.2 coding sequence. The mEOs3.2 sequence was amplified using the mEOs3.2C1 plasmid as template and the following primers: Forward 5'-CATCAAGTGTATCATATGCCAAG and Reverse 5'-caagacgtcgactccggatcgtctggcattgtc. The PCR product and the different pPAGFP-AQP2 plasmids were digested with NdeI and SalI restriction enzymes (ThermoFisher Scientific). The digested plasmids (lacking the pPAGFP sequence) were ligated with mEOs3.2. All sequences were verified by sequencing (Eurofins GATC, Cologne, Germany). cDNA encoding mEos3.2-C1 was a kind gift from Michael Davidson & Tao Xu (Addgene plasmid # 54550; http://n2t.net/addgene:54550).

C.2.2 Cell culture and setup for microscopy

FTM-AQP2 cells [6, 21] were grown at 5 % CO2 and 37°C in Dulbecco's Modified Eagle Medium with 1 g/L D-glucose (DMEM, Gibco), 10% fetal bovine serum (FBS, Gibco), 5 μg/ml Blasticidin S HCL (Gibco) and 100 μg/ml Hygromycin B (Invitrogen). Cells were induced with 10 ng/ml doxycycline to express AQP2, AQP2-S256A or AQP2-S256D and transiently transfected to express mEos3.2-tagged AQP2 and phosphor-mutants 24 hours prior to fixation. Cells were transiently transfected with a mixture of 0.5 μg cDNA constructs and 10 μg sheared salmon sperm DNA (AM9680, Thermo Fischer Scientific) using a Genepulser Xcell (Biorad) for electroporation according to the manufacturer guidelines. After electroporation cells were seeded out on 25mm diameter #1.5 thickness glass coverslips containing gold nanorod fiducial markers (A12-40-600, Nanopartz, Inc.). Cells were fixed at room temperature with cytoskeleton fixation buffer containing 10 mM MES, 3 mM MgCl2, 138 mM KCl, 2 mM EGTA, 0.32 M sucrose (pH 6.1) and 4 % PFA for 20-25 min. Cells were permeabilized for 10 min with 0.1 % Triton X-100 in blocking buffer containing 3 % BSA in PBS, washed and placed in blocking buffer for 20 min. Cells were then stained with 1:200 Alexa647-Phalloidin for 30 min. After fixation and staining, cells were immersed in dSTORM buffer [3] containing 50 mM Tris (pH 8), 10 mM NaCl, 100 mM mercaptoethanol amine, 0.5 mg/mL glucose oxidase, and 0.03 mg/mL catalase (all from Sigma). An 18 mm diameter, #1.5 thickness coverslip was adhered atop the fiducial-containing coverslip with epoxy and sealed.

C.2.3 Expansion microscopy

ExM was performed as previously described with minor modifications [2, 3]. FTM-AQP2 cells [6, 21] were seeded on 22x22 mm collagen coated coverslips. After 24 h, AQP2 expression was induced with 10 ng/mL doxycycline and cells were also incubated with 50 μM indomethacine for 24 h. Cells were washed 3x in PBS and fixed for 10 min with 4% PFA solution at RT. Next, cells were permeabilized with 0.1% Triton X-100 + 3% BSA in PBS for 10 min. Cells were blocked in 3% BSA in PBS for 30 min and incubated with primary antibody (mouse anti-AQP2 antibody, sc-515770, Santa Cruz Biotechnology, 1:20) in 3% BSA in PBS for 1 h. Cells were washed and incubated with secondary antibody (Dylight-594, donkey-anti-mouse, ImmunoReagents inc., 1:100) in 3% BSA in PBS for 1 h. After wash in PBS, cells were post-fixed with 0.25% glutaraldehyde in PBS for 10 min. After PBS wash, cells were incubated with 100 μL monomer solution 8.1 % Na acrylate (Sigma, cat. No.: 408220), 2.66% w/v Acrylamide (Sigma, cat. No.: A9099), 0.32% w/v N,N'-Methylenebisacrylamide (Sigma, cat. no.: M7279), 11.2% NaCl w/v, in PBS) for 1 h at RT. The coverslip was placed upside down on a drop of 190 μL gelation solution (10 μL of 10% v/v TEMED (Sigma cat. No.: T7024) and 10 μL of 10% w/v APS (Sigma cat. No.: A3678) was added to 480 μL of monomer solution) and incubated for 1 h at RT. Subsequently, digestion was performed for 1 h at 37°C (0.5% Triton X-100, 0.8M guanidine HCL (Sigma cat. No: 50-01-1), 8U/mL Proteinase K in TAE buffer). The gel was cut into a smaller piece and placed into 3 mL of MilliQ water in a 6-well plate and incubate overnight at 4°C. The next day, the water was replaced and the gel incubated for 30 min at RT with gentle shaking. This was repeated and subsequently, the MilliQ water was removed and the gel incubated with fresh MilliQ water containing Hoechst (1:500) for 30 min. The gel was washed in MilliQ water for 30 min, placed in an imaging chamber and imaged on a Nikon Eclipse Ti-E system equipped with a 100x 1.45 NA objective and a Zyla sCMOS camera, controlled by NIS Elements from Nikon. The fluorescence illumination system was CoolLED-pE-300white. Fluorescence filter sets for DAPI and TexasRed were used to detect Hoechst and Dylight-594, respectively. Images were deconvolved with Huygens Software (Scientific Volume Imaging, The Netherlands, http://svi.nl).

C.2.4 Imaging

Samples were imaged using interferometric photoactivation localization microscopy (iPALM), as described previously [18, 19]. Samples were placed in the iPALM and sequentially illuminated in TIRF mode with 640nm and 561nm diode lasers, respectively (Opto Engine) through a 60x APO TIRF, 1.49NA objective (Nikon) at 1-3kW/cm2 irradiance. mEos molecules were photoconverted using ca. 1W/cm2 405nm laser illumination (Coherent).For each cell 50.000-75.000 fluorescence images were captured per channel at 30-50 ms exposure time, through a 647nm long pass filter (Semrock) for Alexa Fluor 647 images, or a 593 +/- 20nm bandpass filter (Semrock) for mEos images, onto 3 EM-CCD detectors (iXon, Andor Technology Ltd.). The different channel data sets were aligned using fiducial markers, consisting of gold nanorods (40nm long axis diameter, 25nm short axis diameter from Nanopartz, Inc.). Typical alignment accuracies are on the order of the localization precision

(∼20nm) [19].

C.2.5 Analysis

Single fluorophores were localized in x,y, and z dimensions, and images rendered using the PeakSelector software (Janelia Research Campus). The analyzed data consists of 76 regions of interest (ROI), coming from a total of 19 unique cells. From each cell, 4 ROIs were cropped out, 2 from a central site in the cell, and 2 from an edge site. The number of cells corresponding to different degrees of phosphorylation (WT, A, D), was (7, 6, 6) spread over three independent experiment days, respectively. Regions coming from the same site type in the same cell were treated as a single region by taking averages of any statistics computed on them. For detection of AQP2 clusters (used interchangeably with "vesicles" below), the DBSCAN algorithm [4] was employed, with parameter choices MinPts = 10 and Eps = 50nm. Eps was chosen relatively large to account for the scale of localization uncertainty. Results were not sensitive to these choices for sensible parameter values, due to the large degree of spatial separation of vesicles, relative to their size. The vesicles thus found were modeled as proteins lying on the surface of a hollow sphere following a von Mises-Fisher distribution, observed with Gaussian noise added to each point. The covariance matrix of the noise added to each point in the vesicle was estimated automatically by PeakSelector as part of the localization routine, and was used in place of the true covariance matrix when estimating vesicle parameters, which was done by maximum likelihood. In this manner, we obtain estimates of the vesicle centers and diameters.

Analysis of AQP2 vesicle characteristics, such as their diameter and association with nearby actin, was carried out by first computing a statistic of interest on each vesicle, and then averaging over the vesicles sharing ROI. Linear mixed effects models were used for summarizing results across different ROIs, and model assumptions were checked by residual tests. All models included a random effect shared for the ROIs coming from the same cell, and fixed effects for the degree of phosphorylation, and the ROI cell site (central/edge).

For investigation of colocalization between AQP2 and actin, we first considered if there was significant statistical association for S256-WT. For each ROI, AQP2 vesicle centers were computed, and overlayed on actin. The centers demonstrated spatial stationarity in the XY-plane, but not in the Z-plane. For this reason, we tested for significant association using shifts in the XY-plane only. This was accomplished by a random superposition hypothesis test, based on distances to the 1000 (NN) actin proteins from vesicle shells. To investigate if the degree of colocalization differs based on phosphorylation status, we similarly computed the distances to the 1000 NNs for the S256-A and S256-D type ROIs. For an overall test of differences between mutant types, we modeled the mean distance of these 1000 NNs. Additional tests at each of the k'th nearest actin proteins was done analogously and summarized graphically. We look at the 1000 NNs, as opposed to the raw number of actin molecules within a set of ranges, because the NNs lend themselves more easily to statistical modeling. In addition, the raw number of molecules is significantly more affected by outlier behavior, and a single actin fiber passing close to a vesicle may exhibit 100 or even 1000-folds of artificially increased association scores when compared to the typical vesicle - this effect is much less pronounced for NN distances. The specific choice

to look at 1000 NNs was made primarily so as to correspond to a relevant range of interactions, which in turn depends on the expected range of interactions, protein expression levels, and some additional range to account for noisy observations. The 1000 NNs here corresponds to looking at interactions with actin structures primarily in the 0-300nm distance range, which allows us to look for both very close interactions, and also any indirect interactions mediated by unseen structures. Additionally, by looking at a large number of NNs we obtain a mean distance that is less influenced by the uncertainty in both protein localizations and vesicle parameters.

Acknowledgments

Acknowledgments: We are grateful to data scientist Eric Wait and to technical coordinator Satya Khuon, Advanced Imaging Center, Janelia Research Campus, USA, for technical suggestions regarding data analysis and technical assistance, respectively. Funding: This project was supported by the Independent Research Fund Denmark grant no.: DFF 4181-00379B, Aarhus University Research Foundation (AUFF): AUFF-E-2015-FLS-8-5 and Fonden til Lægevidenskabens Fremme (19-L-0267) (to L.N.N.), a Lundbeck Foundation travel stipend grant no.: R296-2018-2732 to MRH and grant 8721 from the Villum Foundation to the Centre for Stochastic Geometry and Advanced Bioimaging. iPALM imaging was done in collaboration with the Advanced Imaging Center at Janelia Research Campus, a facility jointly supported by the Gordon and Betty Moore Foundation and Howard Hughes Medical Institute.

Author contributions

Author contributions: MRH: Conceptualization, methodology, validation, investigation, Writing - Original Draft, visualization, funding acquisition; LG: Formal analysis, software, methodology, Data curation, Writing - Original Draft, visualization; JA: methodology, validation, investigation, visualization; FHL: Methodology, investigation, resources; SR: Methodology, investigation, visualization; UH: supervision, funding acquisition; LNN: Conceptualization, methodology, validation, Writing - Original Draft, supervision, project administration, funding acquisition.

Competing interests

Authors declare no competing interests.

Data and materials availability

All data, code, and materials used in the analysis is available in some form upon request to any researcher for purposes of reproducing or extending the analysis.

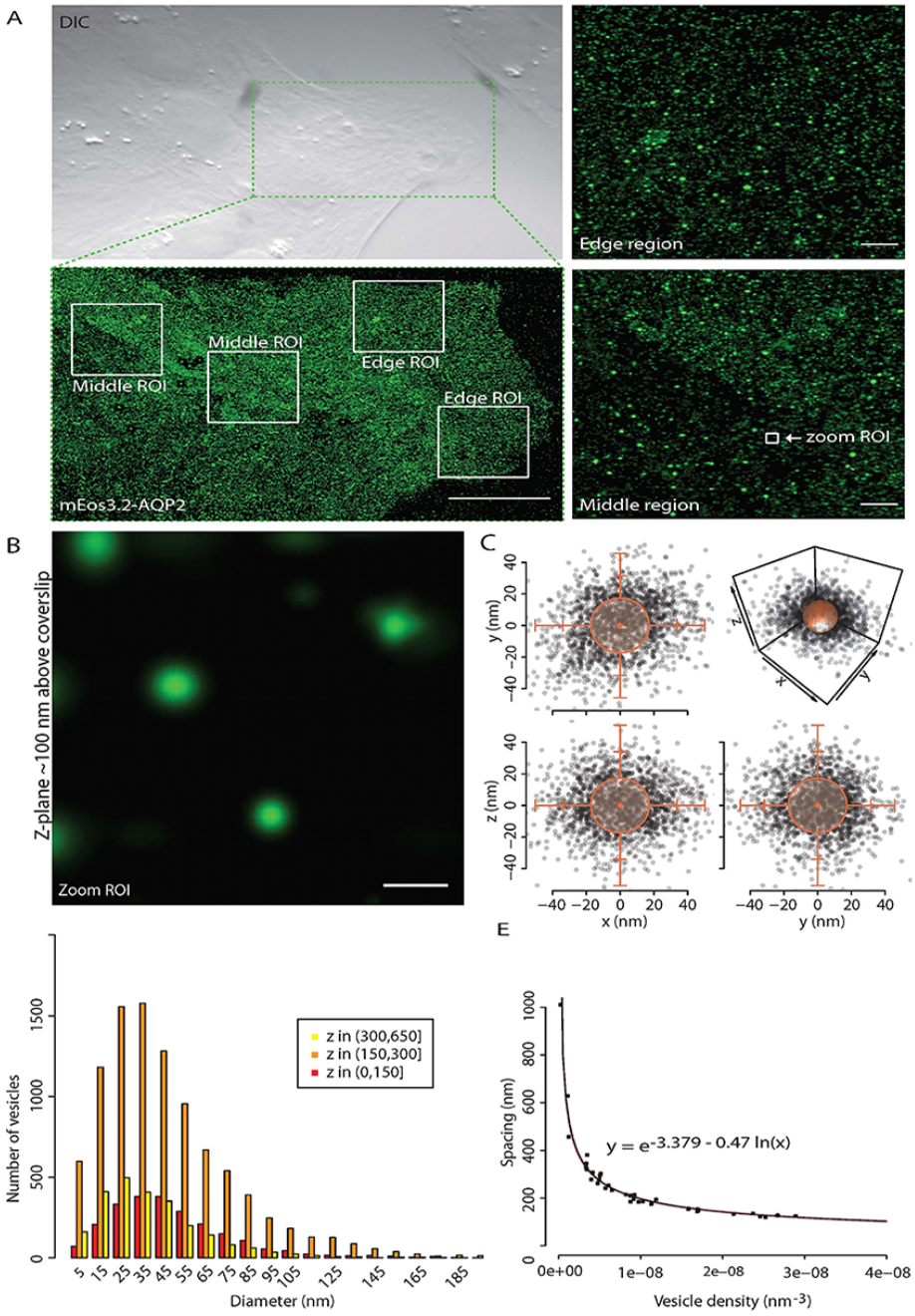

Figure C.1: iPALM localization of AQP2 to small vesicles close to the PM. (A) Upper left, differential interference contrast (DIC) image of cell monolayer and lower left maximum projected micrograph of iPALM renderings of MDCK cells expressing mEos3.2-AQP2 and untagged AQP2, scale bars 10 μm. Upper and lower right maximum projected images show examples of regions of interest chosen for analysis, scale bars 1 μm. (B) Right image shows the zoom ROI from lower right image (A) of a Z-layer with spherical clusters positioned close to the PM, scale bar 100 nm. (C) Clusters found using the DBSCAN algorithm were fitted to a model assuming AQP2 on spherical vesicles observed with noise. The shaded circle/sphere indicate the estimated vesicle. The bars extending from the sphere surface indicate 1 and 2 times the standard deviation of the location uncertainty in the given direction. (D) The distribution of WT vesicle diameters for different sections of depth into the cell. (E) The distance between one vesicle to the nearest other vesicle, as a function of the number of vesicles per nm-3. The shaded area indicates a 95% confidence global envelope.

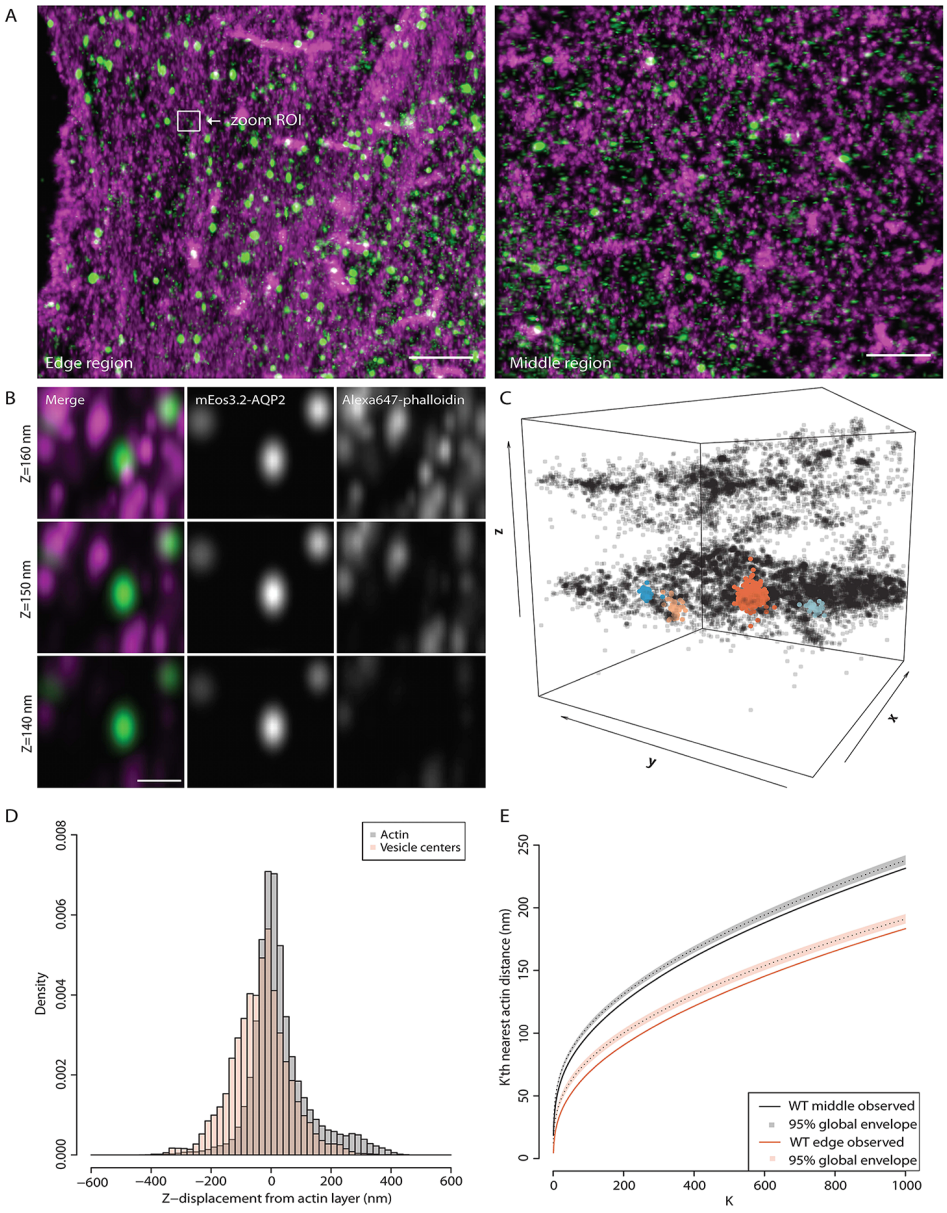

Figure C.2: AQP2 is positioned in vesicles between the PM and the F-actin layer. (A) Representative iPALM renderings of MDCK cells expressing mEos3.2-AQP2 and untagged AQP2 (green), stained with Phalloidin-647 to label F-actin (magenta), scale bars 1 μm. (B) Examples of Z-layers with spherical clusters positioned between the PM and the F-actin layer, scale bar 100 nm. (C) A small, typical cross-section of actin (black points) and the vesicles found using DBSCAN (colored points). F-actin is seen located primarily as a layer structure, and AQP2 localize in close proximity to this layer. AQP2 locations considered as noise by the DBSCAN algorithm are not shown. (D) The z-coordinates of actin and AQP2 vesicle centers, relative to the F-actin layer position. The actin layer position was found as the z coordinate with maximal actin density. (E) The distance from vesicle shells to the K'th nearest F-actin location was computed, and the resulting neighbor-curve was used as a means for quantifying the spatial relations between AQP2 vesicles and actin. This was done both for central (gray) and edge (red) parts of cells. As a test for co-localization, AQP2 vesicles were shifted relative F-actin in the XY-plane, and the neighbor-curves were again computed. Based on 500 shifts, a global envelope test was performed, yielding a region within which the curve would have to lie, assuming independence of AQP2 and actin. The curve lying outside and under the envelope indicates closer AQP2-to-actin distances than would be expected under independence.

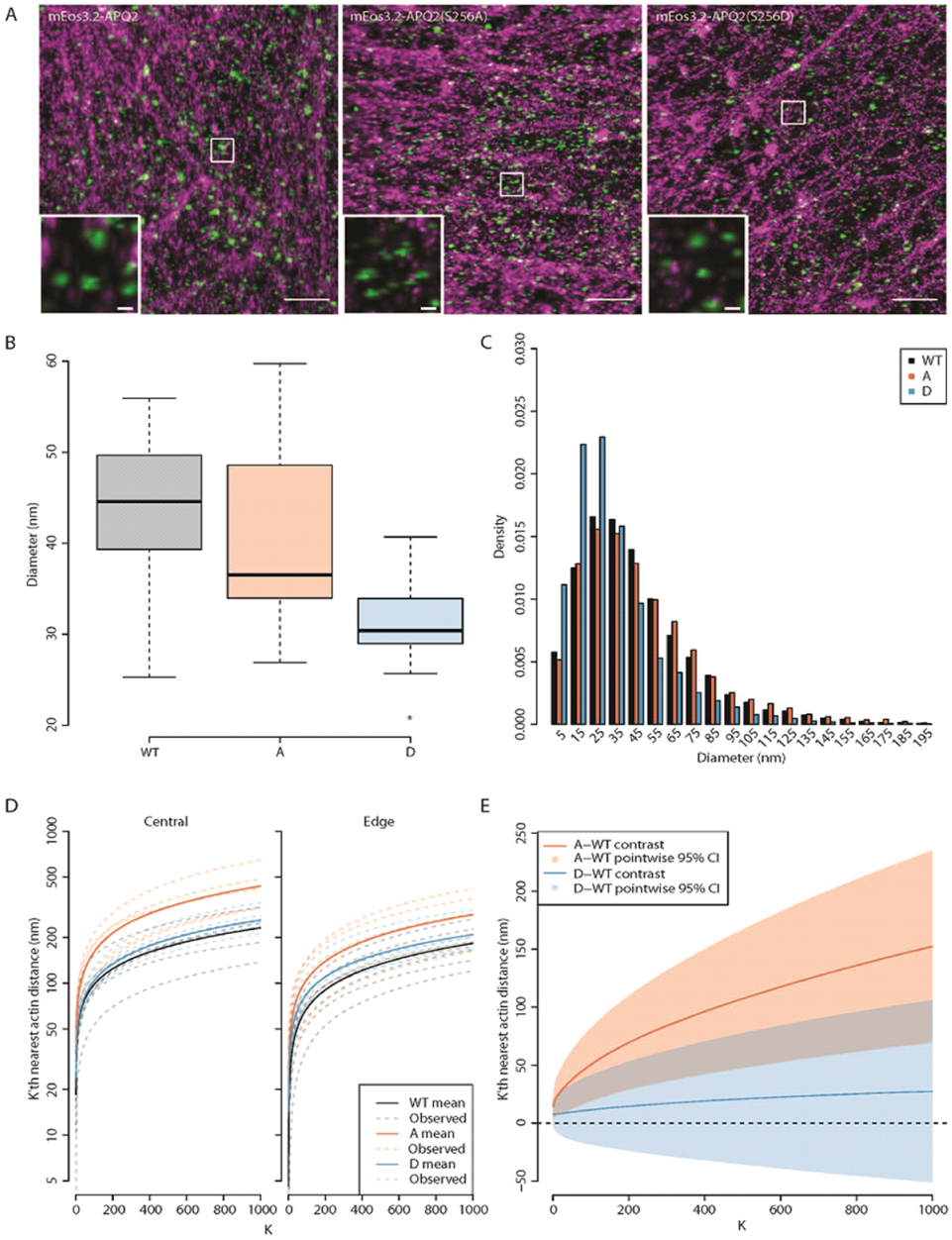

Figure C.3: Phosphorylation of AQP2 at S256 affects vesicle size and F-actin association. (A) Representative iPALM renderings of MDCK cells expressing mEos3.2-AQP2 (left images), mEos3.2-AQP2-S256A and untagged AQP2-S256A (middle images) and mEos3.2-AQP2-S256D and untagged AQP2-S256D (right images). All stained with Alexa647-phalloidin to label F-actin, scale bars 1 μm. The inset zooms show localizations in z-layers under the F-actin layer, scale bars 100 nm. (B) The average vesicle diameter in each data region was used for modeling the mean vesicle diameter size as a function of the cell type. (C) The distribution of observed vesicle diameters across all data regions, for each cell type. (D) Neighbor-graphs computed for each cell and region type, shown on a log-scale. Full lines indicate the mean curves across regions, and dashed lines are curves from individual data regions. The average distance from a vesicle shell to its nearest 1000 actin neighbors was used as a statistic for comparing the degree of association. (E) The distance to the K'th nearest actin location from vesicle surfaces was modelled as a function of cell type, and mean contrasts with WT were estimated. Pointwise confidence intervals were computed for each K between 1 and 1000. These provide a visual description of whether cell mutants are differently, or similarly, associated with actin for varying spatial proximity.

C.I Supplementary materials

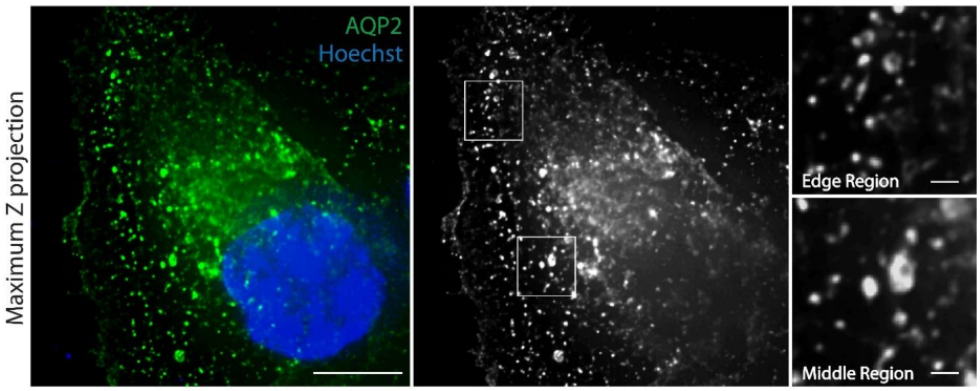

Figure C.4: Localization of endosomal AQP2 by ExM. Cells stably expressing AQP2 were seeded on glass, fixed, stained with ab against AQP2 and Hoechst. Cells were estimated to be expanded 4.5x. This was estimated by measuring nuclei length and comparing expanded with non-expanded cell nuclei. The expansion enabled imaging in x-y with a resolution ~ 45 nm/pixel. Scale bar in left micrograph is 5 μm and 500 nm in right insets.

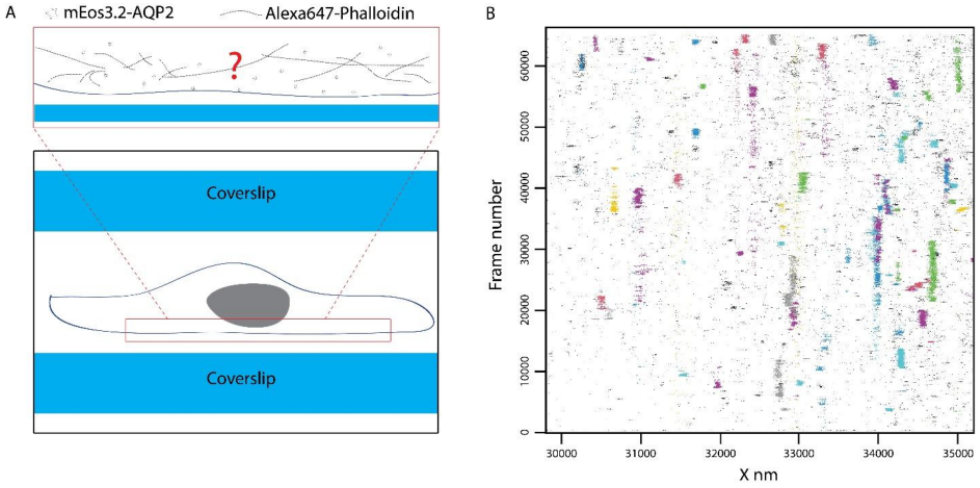

Figure C.5: Setup of iPALM sandwich imaging chamber and Spatio-temporal signal output. (A) Cells were grown on 18-mm coverslips coated with 100-nm gold bead fiducials. After fixation and labelling cells were placed in chambers assembled from the 18-mm cell-containing fiducialed coverglass, 5-min epoxy (ITW Performance Polymers) and vaseline (Unilever), emerged with PHEM buffer and a 25-mm coverglas on top. Imaging chamber was loaded into the microscope and objectives were aligned before iPALM. Corner cells with a medium expression of mEos3.2-AQP2 signal were chosen for imaging. iPALM imaging area is indicated by the red rectangle. (B) Sideview of a region of interest shows the spatio-temporal imaging behavior of detected signal points in a representative ROI. Colored points correspond to the detected groups posited to be vesicles, while black points were considered background and omitted from analysis. The dense clustering structure observed in time indicates an unusually large amount of fluorescent activity in these groups, which may be the result of atypical blinking behavior in tightly packed, fluorescing probes.

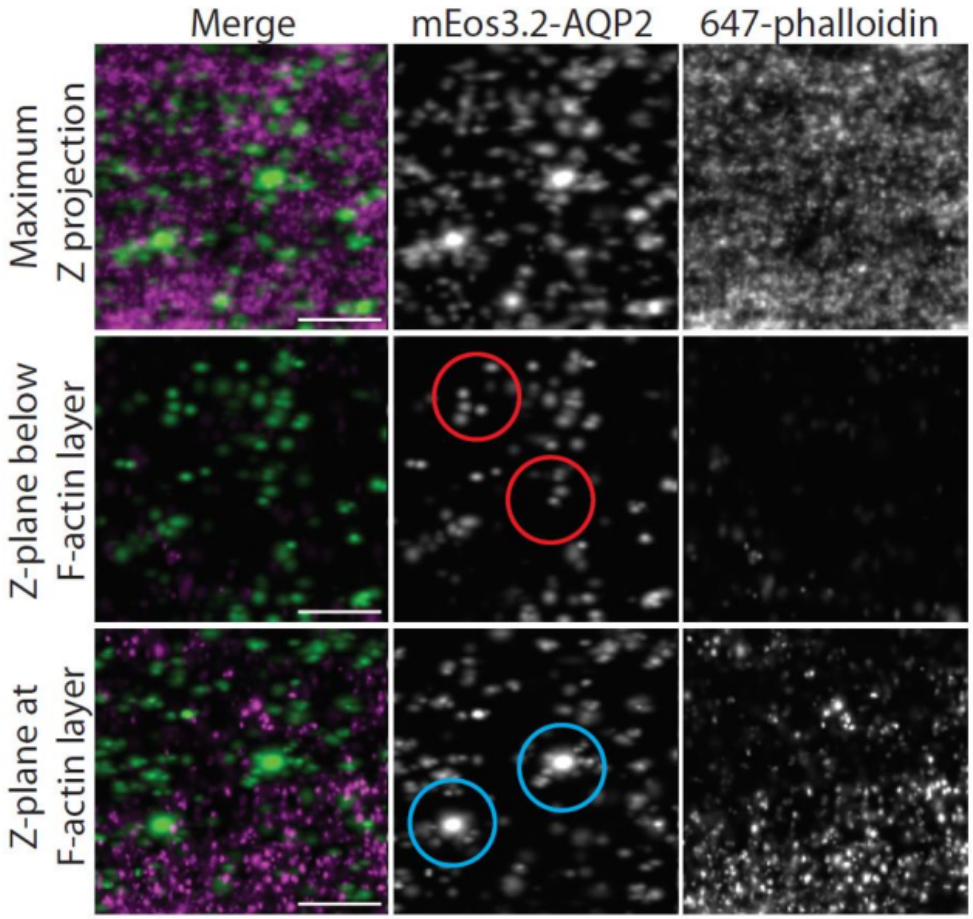

Figure C.6: iPALM positions AQP2 in spherical vesicles and larger endosomes close to the F-actin layer. Representative iPALM renderings of MDCK cells expressing mEOS3.2-AQP2 and untagged AQP2 (green), stained with Phalloidin-647 to label actin (magenta). Small spherical vesicles where localized between the plasma membrane and the F-actin layer (red circles). At the F-actin layer, AQP2 localizations also draw a positioning in endosome-like organelles (blue circles). Scale bars 1 μm.

Movie S1
iPALM localization of AQP2 to small vesicles close to the PM. IMARIS software was used to visualize the vesicular network of rendered 3D micrographs of AQP2 from Figure C.1.

Movie S2
AQP2 is positioned in vesicles between the PM and the F-actin layer. IMARIS software was used to visualize the vesicular network of rendered 3D micrographs of AQP2 in relation to F-actin from bottom located plasma membrane to the F-actin layer positioned ~ 200 nm into the cell.

References

[1] Arnspang, E., F. Login, J. Koffman, P. Sengupta and L. Nejsum (Oct. 2016). AQP2 Plasma Membrane Diffusion Is Altered by the Degree of AQP2-S256 Phosphorylation. *International Journal of Molecular Sciences* 17(11), 1804. DOI: 10.3390/ijms17111804.

[2] Chen, F., P.W. Tillberg and E.S. Boyden (Jan. 2015). Expansion microscopy. *Science* 347(6221), 543–548. DOI: 10.1126/science.1260088.

[3] Chozinski, T.J., A.R. Halpern, H. Okawa, H.-J. Kim, G.J. Tremel, R.O.L. Wong and J.C. Vaughan (Apr. 2016). Expansion microscopy with conventional antibodies and fluorescent proteins. *Nature Methods* 13(6), 485–488. DOI: 10.1038/nmeth.3833.

[4] Ester, M., H.-P. Kriegel, J. Sander and X. Xu (1996). "A Density-Based Algorithm for Discovering Clusters in Large Spatial Databases with Noise". *Proceedings of the Second International Conference on Knowledge Discovery and Data Mining*. KDD'96. Portland, Oregon: AAAI Press, 226–231.

[5] Fenton, R.A., S.K. Murali and H.B. Moeller (July 2020). Advances in aquaporin-2 trafficking mechanisms and their implications for treatment of water balance disorders. *American Journal of Physiology-Cell Physiology* 319(1), C1–C10. DOI: 10.1152/ajpcell.00150.2020.

[6] Holst, M.R. and L.N. Nejsum (July 2019). A versatile aquaporin-2 cell system for quantitative temporal expression and live cell imaging. *American Journal of Physiology-Renal Physiology* 317(1), F124–F132. DOI: 10.1152/ajprenal.00150.2019.

[7] Jang, K.-J., H.S. Cho, D.H. Kang, W.G. Bae, T.-H. Kwon and K.-Y. Suh (2011). Fluid-shear-stress-induced translocation of aquaporin-2 and reorganization of actin cytoskeleton in renal tubular epithelial cells. *Integr. Biol.* 3(2), 134–141. DOI: 10.1039/c0ib00018c.

[8] Kanchanawong, P., G. Shtengel, A.M Pasapera, E.B. Ramko, M.W. Davidson, H.F. Hess and C.M Waterman (Nov. 2010). Nanoscale architecture of integrin-based cell adhesions. *Nature* 468(7323), 580–584. DOI: 10.1038/nature09621.

[9] Klussmann, E., G. Tamma, D. Lorenz, B. Wiesner, K. Maric, F. Hofmann, K. Aktories, G. Valenti and W. Rosenthal (Jan. 2001). An Inhibitory Role of Rho in the Vasopressin-mediated Translocation of Aquaporin-2 into Cell Membranes of Renal Principal Cells. *Journal of Biological Chemistry* 276(23), 20451–20457. DOI: 10.1074/jbc.m010270200.

[10] Knepper, M.A., T.-H. Kwon and S. Nielsen (Apr. 2015). Molecular Physiology of Water Balance. *New England Journal of Medicine* 372(14). Ed. by J.R. Ingelfinger, 1349–1358. DOI: 10.1056/nejmra1404726.

[11] Kuwahara, M., K. Fushimi, Y. Terada, L. Bai, F. Marumo and S. Sasaki (May 1995). cAMP-dependent Phosphorylation Stimulates Water Permeability of Aquaporin-collecting Duct Water Channel Protein Expressed in Xenopus Oocytes.

Journal of Biological Chemistry 270(18), 10384–10387. DOI: 10.1074/jbc.270.18.10384.

[12] Loo, C.-S., C.-W. Chen, P.-J. Wang, P.-Y. Chen, S.-Y. Lin, K.-H. Khoo, R.A. Fenton, M.A. Knepper and M.-J. Yu (Oct. 2013). Quantitative apical membrane proteomics reveals vasopressin-induced actin dynamics in collecting duct cells. *Proceedings of the National Academy of Sciences* 110(42), 17119–17124. DOI: 10.1073/pnas.1309219110.

[13] Mironov, A.A. and G.V. Beznoussenko (Aug. 2019). Models of Intracellular Transport: Pros and Cons. *Frontiers in Cell and Developmental Biology* 7. DOI: 10.3389/fcell.2019.00146.

[14] Moeller, H.B., J. Praetorius, M.R. Rutzler and R.A. Fenton (Dec. 2009). Phosphorylation of aquaporin-2 regulates its endocytosis and protein-protein interactions. *Proceedings of the National Academy of Sciences* 107(1), 424–429. DOI: 10.1073/pnas.0910683107.

[15] Myllymäki, M., T. Mrkvička, P. Grabarnik, H. Seijo and U. Hahn (Mar. 2017). Global envelope tests for spatial processes. *Journal of the Royal Statistical Society: Series B (Statistical Methodology)* 79(2), 381–404. DOI: 10.1111/rssb.12172.

[16] Nedvetsky, P.I. et al. (Oct. 2006). A Role of Myosin Vb and Rab11-FIP2 in the Aquaporin-2 Shuttle. *Traffic* 8(2), 110–123. DOI: 10.1111/j.1600-0854.2006.00508.x.

[17] Qu, L., Y. Akbergenova, Y. Hu and T. Schikorski (June 2009). Synapse-to-synapse variation in mean synaptic vesicle size and its relationship with synaptic morphology and function. *The Journal of Comparative Neurology* 514(4), 343–352. DOI: 10.1002/cne.22007.

[18] Shtengel, G. et al. (Feb. 2009). Interferometric fluorescent super-resolution microscopy resolves 3D cellular ultrastructure. *Proceedings of the National Academy of Sciences* 106(9), 3125–3130. DOI: 10.1073/pnas.0813131106.

[19] Shtengel, G., Y. Wang, Z. Zhang, W.I. Goh, H.F. Hess and P. Kanchanawong (2014). "Imaging cellular ultrastructure by PALM, iPALM, and correlative iPALM-EM". *Methods in Cell Biology*. Elsevier, 273–294. DOI: 10.1016/b978-0-12-420138-5.00015-x.

[20] Tamma, G., E. Klussmann, K. Maric, K. Aktories, M. Svelto, W. Rosenthal and G. Valenti (Dec. 2001). Rho inhibits cAMP-induced translocation of aquaporin-2 into the apical membrane of renal cells. *American Journal of Physiology-Renal Physiology* 281(6), F1092–F1101. DOI: 10.1152/ajprenal.0091.2001.

[21] Tingskov, S.J., H.-J. Choi, M.R. Holst, S. Hu, C. Li, W. Wang, J. Frøkiær, L.N. Nejsum, T.-H. Kwon and R. Nørregaard (Aug. 2019). Vasopressin-Independent Regulation of Aquaporin-2 by Tamoxifen in Kidney Collecting Ducts. *Frontiers in Physiology* 10. DOI: 10.3389/fphys.2019.00948.

[22] Wen, P.J. et al. (Aug. 2016). Actin dynamics provides membrane tension to merge fusing vesicles into the plasma membrane. *Nature Communications* 7(1). DOI: 10.1038/ncomms12604.

Mathematical details for paper C

Given the short-form nature of paper C, the mathematical details had to be considerably compressed. We aim here to provide some additional insight into the more interesting modeling efforts.

CS.1 The data

The data consists of ACT and AQP2 localized in 3D. A total of 19 cells were analyzed, with each cell split into two central and two edge ROIs, see Figure CS.1. Of the 19 cells, 7 expressed wildtype AQP2-WT, 6 the phospho-mimicking AQP2-D mutant, and another 6 the non-phospho-mimicking AQP2-A mutant. In addition to the 3D positions of each protein, we also had access to localization uncertainties in the xy and z planes, and the camera frame numbers associated with each observation. The data shows that ACT is positioned in a layer consisting of dense fibers, whereas AQP2 is more homogeneous and sparse, organizing into small spherical clusters, see Figure CS.2.

CS.1.1 On blinking artifacts in paper C

As noted also in the paper, the data exhibited large spatio-temporal clusters. The question of whether these clusters were the result of individual blinking PA-FP with unusually long lifetimes, or several close-by PA-FP interacting in some unforeseen way, could not be determined on the basis of the data alone, with some authors (myself) believing the clusters to be artifacts that needed correction, while the majority believed the clusters were too large to be blinking alone. As a compromise, we analyzed the data in its raw form, while being open about this shortcoming. In this light, the statistical analysis of vesicles and interactions should be interpreted with some care.

CS.2 Analysis of aquaporin vesicles

Aquaporin localizations demonstrated an organization into well-separated (especially in 3D), compact clusters. These clusters were segmented out automatically using the DBSCAN [2] algorithm, with hyperparameters chosen manually to best align the resulting grouping with the visual impression of clustering. Biologists had an expectation that AQP2 would organize into vesicles, and it was desirable to apply this interpretation to the DBSCAN clusters. To validate this interpretation, we imaged a cell of the same type using expansion microscopy (ExM) [1]. ExM is essentially conventional fluorescence microscopy, but where the sample is first isotropically

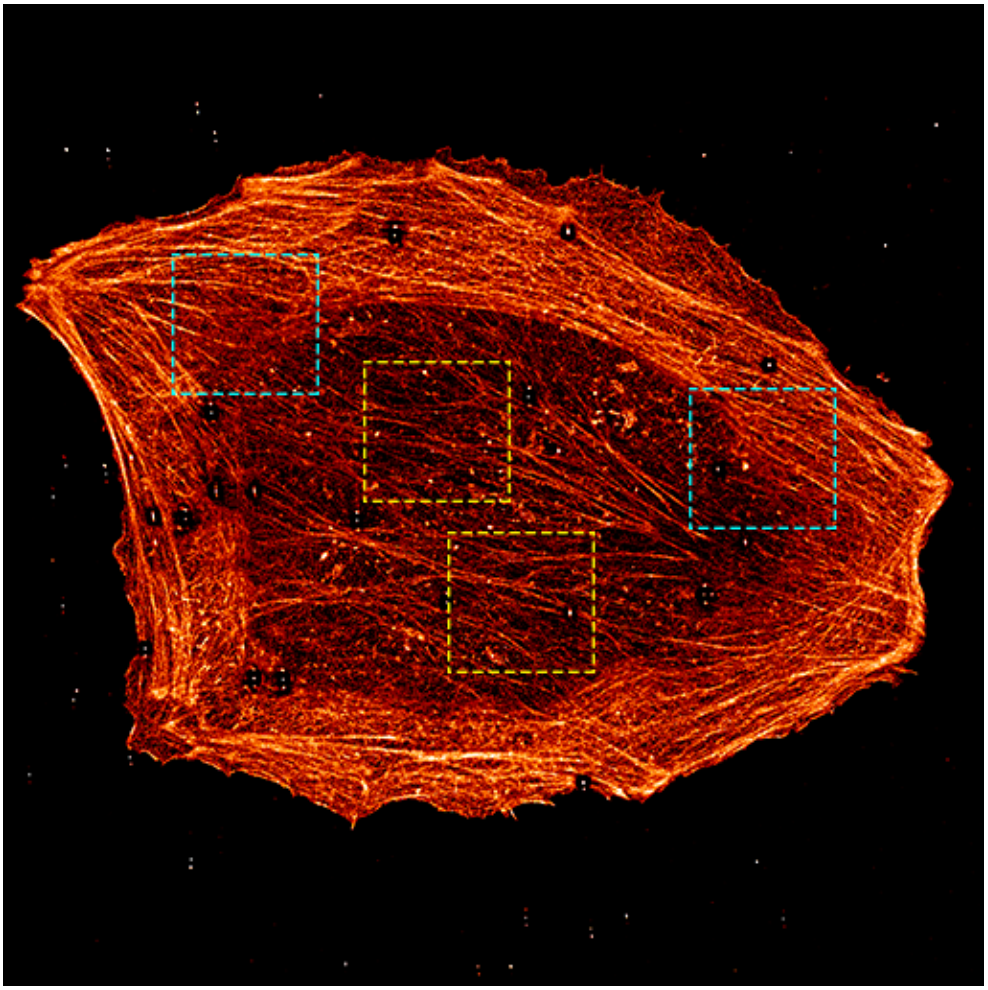

Figure CS.1: A representative cell. Four ROIs are segmented from each cell, with two edge regions (blue) and two central regions (yellow).

enlarged by means of a polymer network, allowing for better effective resolution. ExM showed that AQP2 does indeed organize into vesicular structures of a size consistent with the DBSCAN clusters, allowing us to continue with our interpretation.

CS.2.1 Obtaining vesicle parameters

Vesicles are spherical, hollow objects. For AQP2 trafficking, AQP2 proteins line the surface of the vesicle [5], which serves as a starting point for modeling of the DBSCAN clusters. Let $(u_i)_{i=1}^m = (X_i, Y_i, Z_i)_{i=1}^m$ be the 3D localizations associated with a vesicle, and $(\sigma_{xy,i}, \sigma_{z,i})_{i=1}^m$ be localization uncertainties in the xy and z planes, respectively. For iPALM the uncertainty in the z dimension is typically lower than in the xy plane, and we thus need to treat them separately. We assume each localization is i.i.d., and

take as basis the model

$$u_i = c + rs_i + \epsilon_i, \tag{CS.2.1}$$

$$s_i \sim vMF(\mu, \tau), \tag{CS.2.2}$$

$$\epsilon_i \sim N(0, \Sigma_i) \tag{CS.2.3}$$

where $c \in \mathbb{R}^3$ is the vesicle center, $r \geq 0$ is the vesicle radius, ϵ_i is the localization error, and s_i is the protein location on the unit-sphere, following a von Mises-Fisher distribution with mean direction μ and concentration parameter τ. Specifically, the density of s_i is given as

$$f_s(x) = C(\tau)e^{\tau\mu^T x}, \tag{CS.2.4}$$

where the normalization C is given as

$$C(\tau) = \frac{\tau^{3/2-1}}{(2\pi)^{3/2} I_{3/2-1}(\tau)}, \tag{CS.2.5}$$

where $I_{3/2-1}$ is the modified Bessel function of the first kind of order $3/2 - 1$. In order to estimate parameters via maximum likelihood in a way that is quick enough to be performed on thousands of vesicles, we need a sufficiently simple expression for the density of u_i, which is only forthcoming in the case where $\Sigma_i = \sigma^2 I_3$ is constantly a diagonal matrix. To approximate this situation, let

$$\sigma_{xy}^2 = \frac{1}{m}\sum_{i=1}^{m} \sigma_{xy,i}^2 \tag{CS.2.6}$$

$$\sigma_z^2 = \frac{1}{m}\sum_{i=1}^{m} \sigma_{z,i}^2, \tag{CS.2.7}$$

and assume the uncertainty of each localization in the xy-plane is exactly σ_{xy}, and similarly for σ_z in the z-plane, that is $\Sigma_i = \Sigma$ with

$$\Sigma = \begin{pmatrix} \sigma_{xy}^2 & 0 & 0 \\ 0 & \sigma_{xy}^2 & 0 \\ 0 & 0 & \sigma_z^2 \end{pmatrix} \tag{CS.2.8}$$

Next, define the covariance matrix

$$\Sigma^{aug} = \begin{cases} \begin{pmatrix} 0 & 0 & 0 \\ 0 & 0 & 0 \\ 0 & 0 & \sigma_{xy}^2 - \sigma_z^2 \end{pmatrix} & \text{if } \sigma_{xy} \geq \sigma_z \\ \begin{pmatrix} \sigma_z^2 - \sigma_{xy}^2 & 0 & 0 \\ 0 & \sigma_z^2 - \sigma_{xy}^2 & 0 \\ 0 & 0 & 0 \end{pmatrix} & \text{if } \sigma_{xy} < \sigma_z, \end{cases} \tag{CS.2.9}$$

and define the i.i.d. augmentation variables

$$\epsilon_i^{aug} \sim N(0, \Sigma^{aug}). \tag{CS.2.10}$$

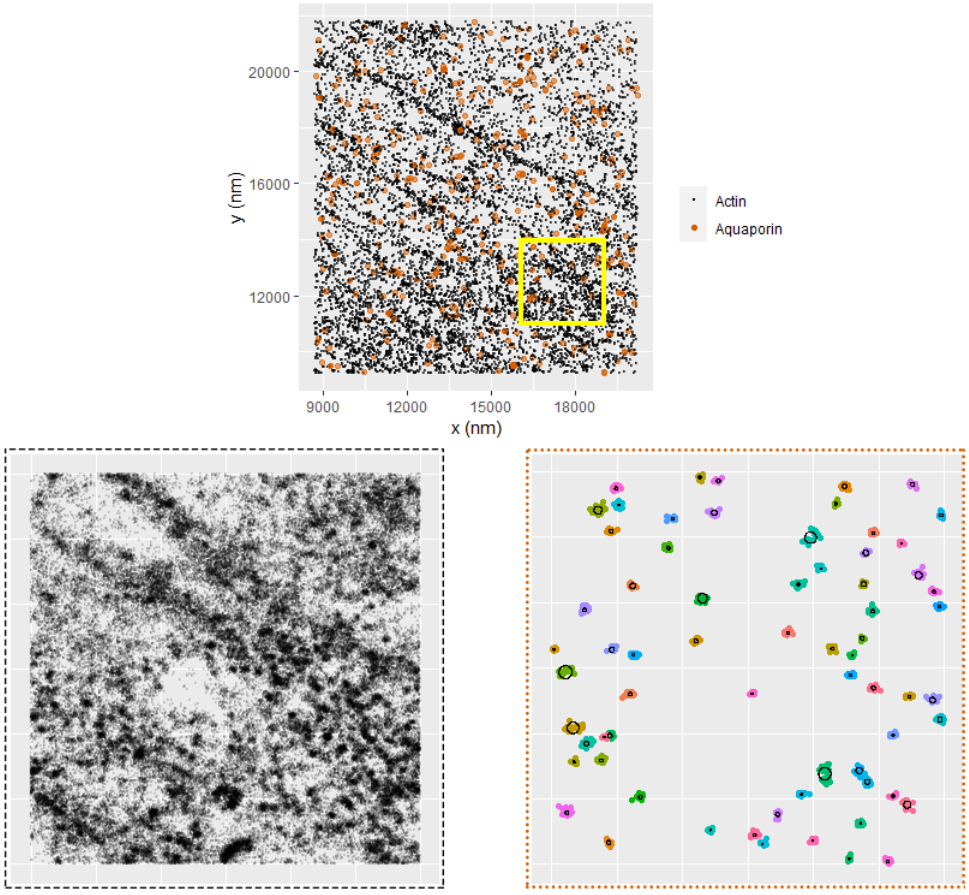

Figure CS.2: A representative ROI of ACT and AQP2 (top). A small subset of the ROI (in yellow) is magnified in the bottom row, showing the complex organization of ACT (left) and the spherical clusters of AQP2 (right). The AQP2 colors indicate the clustering found by the DBSCAN algorithm, and the circles indicate the fitted vesicle parameters. Note that the vesicles were found and parameters estimated on the basis of the 3D data, but we only show the projection unto the xy-plane here for easier visualization.

Finally, we add noise to the observed u_i in order to make the covariance matrix isotropic, so let

$$u_i^{aug} = u_i + \epsilon_i^{aug}, \tag{CS.2.11}$$

and u_i^{aug} then has localization uncertainty with diagonal covariance matrix $\Sigma = \sigma^2 I_3$, with $\sigma^2 = \max\{\sigma_{xy}^2, \sigma_z^2\}$. On the basis of $(u_i^{aug})_{i=1}^m$, the parameters have likelihood [3]

$$L(c, r, \mu, \tau) = \prod_{i=1}^{m} \frac{C(\tau)(2\pi\sigma^2)^{-3/2}}{C(\|\tau\mu + r(u_i^{aug} - c)/\sigma^2\|)} exp\left\{-\frac{1}{2\sigma^2}(\|u_i^{aug} - c\|^2 + r^2)\right\}, \tag{CS.2.12}$$

which is maximized numerically. We optimized over c in the neighborhood of the average cluster position, c_0, which was also the initializing value for c. As an initializing value for r, we can notice that in the case where s_i is uniform on the sphere, it is easy to show that

$$\mathbb{E}\left[\|u_i^{aug}\|^2\right] = r^2 + \|c\|^2 + tr(\Sigma) \tag{CS.2.13}$$

and consequently we initialized r with the value

$$r_0 = \sqrt{\frac{1}{m}\sum_{i=1}^{m} \|u_i^{aug}\|^2 - \|c_0\|^2 - tr(\Sigma)}, \tag{CS.2.14}$$

whenever this value is well-defined, and otherwise we set $r_0 = 0$. Examples of vesicle fits can be seen in the bottom right subplot of Figure CS.2.

CS.3 Association between aquaporin and actin

Association is a term that is used somewhat loosely in the literature on protein colocalization analysis. For the test of significant association between AQP2 and ACT, we treated it as a matter of statistical dependence between point processes. For a given ROI, let X be a point process of the 3D localizations of AQP2, and Y similarly a point process of localizations of ACT. Broadly we are interested in testing the null-hypothesis of independence

$$H_0 : X \perp\!\!\!\perp Y. \tag{CS.3.1}$$

To perform this test in a way that also provides information on the nature of dependence, let S be a function of X and Y, measuring some facet of their simultaneous organization. In the paper, S is a curve of the average distances to the 1000 nearest neighbors in Y from the vesicle shells in X. This choice puts particular focus on spatial proximity between vesicles and ACT, which was of primary interest for this study.

Testing H_0 is done by comparing the observed value of $S(X, Y)$ with the distribution of S when X and Y are drawn from H_0. Rather than specify the marginal distributions in full, it is sufficient to have a degree of stationarity. Given the observed AQP2 organization, we postulate that $X = (x_{1i}, x_{2i}, x_{3i})_{i=1}^N$ is invariant to shifts in the xy-plane, in the sense that

$$X \overset{d}{=} (x_{1i} + s_1, x_{2i} + s_2, x_{3i})_{i=1}^N, \tag{CS.3.2}$$

for any $(s_1, s_2) \in \mathbb{R}^2$. On the basis of several such shift-vectors, a realization of S under the null (strictly speaking, a conditional version of the null) was obtained. Since S is a curve, we performed the test for dependence using a global envelope test [4].

References

[1] Chen, F., P.W. Tillberg and E.S. Boyden (Jan. 2015). Expansion microscopy. *Science* 347(6221), 543–548. DOI: 10.1126/science.1260088.

[2] Ester, M., H.-P. Kriegel, J. Sander and X. Xu (1996). "A Density-Based Algorithm for Discovering Clusters in Large Spatial Databases with Noise". *Proceedings of the Second International Conference on Knowledge Discovery and Data Mining*. KDD'96. Portland, Oregon: AAAI Press, 226–231.

[3] Mukhopadhyay, M., D. Li and D.B. Dunson (Aug. 2020). Estimating densities with non-linear support by using Fisher–Gaussian kernels. *Journal of the Royal Statistical Society: Series B (Statistical Methodology)* 82(5), 1249–1271. DOI: 10.1111/rssb.12390.

[4] Myllymäki, M., T. Mrkvička, P. Grabarnik, H. Seijo and U. Hahn (Mar. 2017). Global envelope tests for spatial processes. *Journal of the Royal Statistical Society: Series B (Statistical Methodology)* 79(2), 381–404. DOI: 10.1111/rssb.12172.

[5] Valenti, G., G. Procino, G. Tamma, M. Carmosino and M. Svelto (Dec. 2005). Minireview: Aquaporin 2 Trafficking. *Endocrinology* 146(12), 5063–5070. DOI: 10.1210/en.2005-0868.